Diffusion Tensor Echo Planar Imaging with High Spatial Resolution and Its Applications

Jiun-Jie Wang

Department of Medical Physics and Bioengineering

University College London

Submitted as a Ph.D. Thesis

20 March 2002

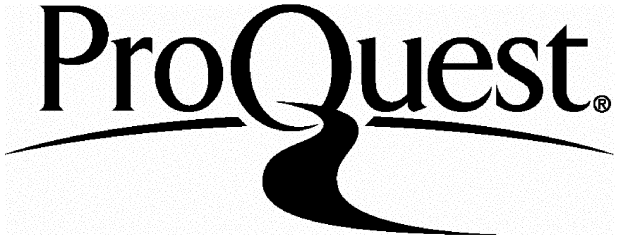

To My Family

Contents

List of Figures

List of Tables

Acknowledgment

First of all, I would like to thank the very inspiring supervision from Professor Roger Ordidge and Professor Robert Turner. This thesis is completed with the help from their great foresight.

I would like to thank for the help and support from the Physics group in the Functional Imaging Laboratory, the NMR group in the Medical Physics and Bioengineering Department, the biophysics unit in the Institute of Child Health and the MRI center in the Great Ormond Street Hospital, especially for the following people who helped me so much in my project: Ralf Deichmann, Oliver Josephs, Chloe Hutton, John Ashburner, David Thomas, John Thornton, Fernando Calamante and many other PhD students and research fellows.

As a foreigner living alone in London, I am also very grateful to those friends I made in Europe, who are very nice and kind to me and who leave a wonderful memory in my life which will never dies away.

I have to thank ChangGung University for the financial support to my PhD study and the offer to a faculty position. I have to especially thank Dr. Wan Yung Liang for helping me with this great chance. I have to acknowledge my other old buddies in Taiwan who stood out whenever I needed help.

I am proud to say that my sweet Chloe, my first daughter, also visited this world at the time when I was close to finishing the writing of this thesis. Finally I have to deeply thank my parents and grandmother, to whom this thesis is dedicated to.

Abstract

Magnetic Resonance Imaging is at present the only imaging technique available to measure diffusion of water and metabolites in humans *in vivo*. It provides vital insights to brain connectivity and has proved to be an important tool in diagnosis and therapy planning in many neurological diseases such as brain tumours, ischaemia and multiple sclerosis. This project focuses on the development of a high resolution diffusion tensor imaging technique. In this thesis, the basic theory of Diffusion Tensor Magnetic Resonance Imaging is presented. The technical challenges encountered during development of these techniques will be discussed, with proposed solutions. New sequences with high spatial resolution have been developed and the results are compared with the standard technique more commonly used. A fiber tracking algorithm based on following the principal eigenvector of the diffusion tensor in each voxel is implemented and tested on the data acquired by the new sequence under various conditions.

Chapter 1

Introduction

1.1 Applications of Diffusion Imaging in Human Brain

Diffusion is the result of the random movements of particles caused by the thermal agitation. The major effect from such motion on the diffusion weighted MR experiment is signal attenuation.

One of the most important features of diffusion imaging (Diffusion Weighted Imaging, DWI, and Diffusion Tensor Imaging, DTI as in Chapter 2) is the ability to identify ischaemic events, such as acute stroke, before any T_2 weighted changes can be seen in conventional imaging (Moseley *et al.*, 1990b). The use of conventional MR images in the early detection of brain ischaemia is limited because the change in T_2 is only apparent after 2 to 5 hours of the event (Buonanno *et al.*, 1982; Moseley *et al.*, 1990b; Knight *et al.*, 1991). However, the initial drop of measured Apparent Diffusion Coefficient (ADC) in the same area can occur within minutes immediately after the event (Mintorovitch *et al.*, 1991; Moseley *et al.*, 1990a; Benveniste & Johnson, 1992). The reason that ischaemia results in a drop of the measured ADC is still an issue of debate. Several causes have been suggested such as the cytoxic cell swelling that occurs at ischaemia, arising from the metabolic failure of the transmembrane pump maintaining osmotic balance (Moseley

et al., 1990b) . Another possible explanation is a simple slowing of intracellular cytosolic streaming of protons and metabolites (Benveniste & Johnson, 1992). Also the decrease of membrane permeability may result in an increased barrier to proton translational processes (Siesjo, 1978).

Because the water diffusion in a fluid filled cyst is less restricted than in solid tissue, diffusion imaging has been used to characterise tumours *in vivo* with different tissue types, which might have similar T_1 and T_2 contrast (LeBihan *et al.*, 1986). Diffusion imaging may help to resolve issues such as tumour staging, separation of edema, cystic lesion, solid tumour, distinguishing between radiation necrosis and tumour recurrence, which cannot be answered by conventional imaging methods (LeBihan *et al.*, 1995).

Diffusion Imaging also has applications to studies of Multiple Sclerosis, because the water diffusion is sensitive to the inflammatory process and loss of neuronal integrity during the progress of the disease (Larsson *et al.*, 1992; Horsfield *et al.*, 1998).

One of the most ambitious applications of diffusion imaging is white matter fiber tracking using the information from the measured diffusion tensor (Conturo *et al.*, 1999; Mori *et al.*, 1999a). The diffusion in the biological environment is restricted and hindered. In white matter in the brain, it mainly follows the directions of the fiber tracts. With the information from the direction of the anisotropic diffusion, it is possible to trace the directions of the axonal fibers which connect various parts of the brain.

The major restriction in the general use of diffusion imaging is the limited spatial resolution. To allow sufficient Signal-to-Noise Ratio, the current spatial resolution used in most of the diffusion measurements corresponds to a voxel size of 3 mm. This can result in significant partial volume artefacts. Further complications arise from motion and eddy current related artefacts. The details will be discussed in the following chapters.

1.2 Overview of the Thesis

The project aims are the development of diffusion tensor imaging techniques with a high spatial resolution .

Chapter 2 will describe the basic physics of MRI, the phenomenon of diffusion and the measurement of diffusion by MRI. The basic parameters used throughout the project will be presented.

In Chapter 3, a reproducibility study on DTI with the single shot EPI sequence will be conducted. The single shot DT-EPI was carried out on a stroke patient.

In Chapter 4, current techniques on high spatial resolution DTI will be explored. Sequences of Interleaved EPI of two segments and EPI with Half Fourier acquisition will be developed. The sources of artefacts which contaminate most DT images will be discussed with solutions proposed.

Chapter 5 proposes a new selective averaging algorithm for the data acquired by the sequences of interleaved EPI. It does not require cardiac gating during data acquisition period and thus increases the speed of data collection.

A new ghost free segmented EPI sequence will be presented in Chapter 6: Half-FOV EPI. The technique will be tested on a phantom *in vitro* as well as in two normal male volunteers *in vivo*.

A comparison study on diffusion tensor imaging was conducted in Chapter 7 relative to the sequence of single shot DT-EPI. The sequences for comparison include the Interleaved EPI of two segments and the new Half-FOV EPI, both with and without cardiac gating.

In Chapter 8, a fiber tracking algorithm based on following the direction of the principal eigenvector was tested on the diffusion tensor data acquired by the Half-FOV EPI sequence. ROIs in the Genu of Corpus Callosum were selected from data acquired in a single session and coregistered from multiple sessions. A study on the potential bias using anisotropic voxels will be presented.

The thesis ends with conclusions in Chapter 9. The future work will be described.

Chapter 2

Diffusion Weighted Echo Planar Imaging

2.1 General Introduction to MRI

The basic physics of Magnetic Resonance Imaging deals the properties of the spins, precession, relaxations and spatial encoding techniques. Those are well documented phenomena. For a proper understanding of the Echo Planar Imaging, the major imaging technique used throughout this project, the introduction begins with the concept of k-space, which is the reciprocal space of the spatial domain. For the fundamental concepts in MRI, it can be referred in books by 'The Basics of MRI' by Professor Joseph P. Hornak (Hornak, 1996) or 'Magnetic Resonance Imaging' by Dr. M.T. Vlaardingerbroek and Dr. J. den Boer (Vlaardingerbroek & den Boer, 1996) .

2.2 k-space

A vector in k-space represents the integral of the gradient activity history at time, t, and can be defined in Equation 2.1.

$$\vec{\kappa}(t) = \gamma \cdot \int_0^t \vec{G}(t')dt' \tag{2.1}$$

The MR signal in k-space represents the spatial frequencies present in the object being imaged. The gradient activity makes signal evolve from one part of k-space to ancther. To reconstruct one slice of an image, the raw data needs to be sampled from k-space properly before any data processing. The central part of k-space, which contains information of low spatial frequency, and hence of low spatial resolution, determines the largest signal component of the image. The peripheral part of k-space, which contains high frequency information determines the edges, fine details and subtle contrast in the reconstructed image. If Δt_x and Δt_y are the effective time increments between sampled data points in the x (readout) and y (phase encode) directions, the minimum sampling distance in k-space depends on the Field of View of the image, as described in the following Equations 2.2 (readout direction) and 2.3 (phase encoding direction) :

$$\Delta\kappa_x = \gamma \cdot G_x \cdot \Delta t_x = \frac{2\pi}{FOV_x} \tag{2.2}$$

$$\Delta\kappa_y = \gamma \cdot G_y \cdot \Delta t_y = \frac{2\pi}{FOV_y} \tag{2.3}$$

where FOV_x and FOV_y are the Field Of View in x and y directions respectively.

2.2.1 Image Resolution

When two features in an image are distinguishable, they are said to be resolved. The ability to resolve two features in an image is a function of many variables such as T_2, Signal-to-Noise Ratio, sampling rate, slice thickness, and image matrix size, to name

a few. Resolution is a measure of image quality. When two features 1 mm apart are resolvable in an image, the image is said to be a higher resolution image than one where two features are not resolvable. Resolution is inversely proportional to the separation of two resolvable features.
In this work, the spatial resolution is defined as FOV/N where FOV = Field Of View, and N = number of data points across an image. We will never resolve two features located less than FOV/N, or one pixel, apart.

2.3 Echo Planar Imaging

Conventional Magnetic Resonance Imaging techniques entail a long acquisition time. To reduce the scanning time, fast imaging techniques were introduced. In spite of the hardware demand, Echo Planar Imaging (EPI) is now available in most clinical scanners in the world as the fastest imaging technique. It provides the best SNR per unit time. The EPI sequence is the main technique developed and used in this project and will be described in the following section.

2.3.1 Historical Background

The historical development of Echo Planar Imaging (EPI) began with the realization that the Nuclear Magnetic Resonance (NMR) technique can be used to provide images of nuclear spin density. However, because of the technical difficulties, it was not until 1977 (Mansfield, 1977) that Sir Peter Mansfield conceived that the complete k-space data could be acquired on the order of msec with only one single excitation RF pulse using this technique. Early development was focused on low field scanners of 0.1 or 0.5 Tesla because of the hardware demands (Mansfield & Pykett, 1978; Edelstein *et al.*, 1980).

In 1985 in the University of Aberdeen, Johnson et al (Johnson & Hutchinson, 1985) developed the Blipped Echo planar Single pulse Technique (BEST), which uses blips instead of a constant gradient in the phase encoding direction. This provides great advantages in image reconstruction because no re-gridding in k-space is required.
The image quality in EPI sequences was compromised by slow switching and complicated eddy current behaviour in the early scanners. The development of an actively shielded gradient coil allowed cleaner gradient switching and better eddy current performance (Mansfield & Chapman, 1986; Turner & Bowley, 1986; Römer *et al.*, 1986).
Because of the fast acquisition and motion free image quality, early EPI development was focused on moving organs such as the heart (Ordidge *et al.*, 1981). Its potential for brain imaging was soon discovered. By late 1980s, Turner and LeBihan developed the first diffusion weighted EPI sequence (Turner, 1988; Turner *et al.*, 1990). Other applications of EPI such as perfusion weighted MRI (Rosen *et al.*, 1989), or the study of brain function with the Blood Oxygenation Level Dependence (BOLD) effect (Kwong *et al.*, 1992; Belliveau *et al.*, 1991) were evolving at the same time.

2.3.2 Image Acquisition and Reconstruction in EPI

Echo Planar Imaging is an ultra fast imaging sequence. With EPI, after the slice of interest is selectively excited, the whole k-space data are acquired with a fast switching gradient before the signal decays away through spin-spin relaxation as shown in Figure 2.1. The total acquisition time for one slice of image is, thus, usually less than 100 msec. This makes it possible to cover the whole brain in a very short time .

EPI images are mainly T_2 or T_2^* weighted. A typical sequence consists of two modules. The first part is a preparation module and the second part is a data acquisition module. In the preparation module, the slice of interest is excited by a 90 degree RF pulse applied

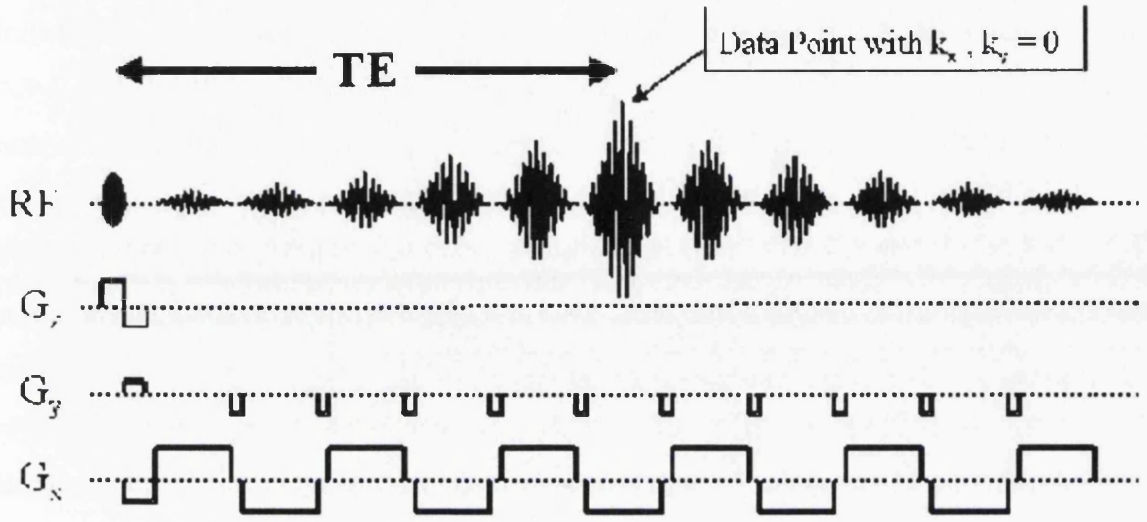

Figure 2.1: The diagram shows the structure of a typical Echo Planar Imaging sequence

with a slice selective gradient. The sequence can be made T_2 weighted by adding in a refocusing 180 degree RF pulse. Various desirable contrasts can be implemented during the preparation stage of EPI sequence. Diffusion weighting can be added by introducing diffusion weighting gradients.

During the data acquisition module, raw data in the k-space are acquired by a fast switching readout gradient. There are many designs of different k-space trajectory schemes. Most commonly used is the rectangular trajectory. The raw data in k-space can be acquired in a spiral manner as well.

To acquire the raw data in a rectangular k-space trajectory scheme, a short blip gradient in the phase encoding direction is applied after each echo is acquired (Johnson & Hutchinson, 1985). The blip in the phase encoding direction brings the k-space trajectory to the next phase encoding step. The reconstruction of the final image is straightforward with 2D Fourier Transformation after the temporal reversal of alternate k-space lines. Usually one-dimensional Fourier Transformation is performed in the x- (readout/

frequency encoding) direction. The data needs to be phase corrected before the second Fourier Transformation. This can be done by using the phase information extracted from the navigator echoes, a separate set of echoes acquired without phase encoding (Ordidge *et al.*, 1994; Kelley & Ordidge, 1993; Bruder *et al.*, 1992). In the project, all the EPI data was phase corrected using a MATLAB program developed by the author.

Any hardware imperfection and magnetic field inhomogeneity introduce additional time shift and phase evolution in the raw data. Because in EPI, alternate k-space lines are acquired with gradients of opposite polarities, the raw data need to be temporally reversed, which shifts this additional evolution in time and phase towards opposite directions between two neighbouring k-space lines. Without correction, this shift will lead to formation of a ghost at a position shifted by half of the FOV, after image reconstruction. The correction is usually done by using the phase information extracted from a set of navigator echoes. Each navigator echo is a representation of the projection of all the spins contained in a plane perpendicular to the direction of frequency encoding. Either the same number of navigator echoes as the number of lines in the image is acquired, or only a few navigator echoes are used. It has been shown that using two navigator echoes to perform the phase correction is more effective in reducing the N/2 ghost than using the same number of echoes as the number of lines in the image (Wong, 1992). In the work described in Chapter 4, three navigator echoes were acquired instead of two, to compensate for the fact that the echoes were acquired at different echo times with different off-resonance effect (Heid, 2000).

Throughout the project, the navigator echoes were acquired immediately before the EPI readout began along the frequency encoding direction, with the phase encoding gradient switched off. After the acquisition of the navigator echoes, the phase difference between the alternate lines was extracted at each point, and was subsequently applied to phase correct the original data. The final image is produced after a second Fourier Transformation performed in the y- (phase encoding) direction.

The data can also be acquired with a constant gradient in the phase encoding direction.

The k-space trajectory will be in a zigzag format. The k-space trajectory may be re-gridded to a rectangular format before the image reconstruction.
The EPI sequence is demanding because the system needs to be able to provide stable switching gradients of opposite polarities within a very short time. The advantage of EPI is that it provides an ultra-short acquisition time. The SNR per unit time is relatively high compared with conventional imaging technique. Yet, the image quality tends to be inferior due to the relatively long signal acquisition time.
In addition to the single shot technique, the raw data in EPI sequences can be acquired within several excitations (Chapman *et al.*, 1987; Rzedzian, 1987). Each excitation only acquires part of the data in k-space. The raw data are spliced together later prior to image reconstruction. The details of the multiple shots techniques will be discussed in Section 4.1.

2.3.3 Hardware Demand

A major hardware design consideration in EPI is the requirement of regularly producing large, stable and fast switching gradients. Most modern clinical scanners can provide reasonably reliable and stable systems for EPI acquisition. Thus, in this section we are only discussing the requirements instead of presenting a practical solution. An understanding of the requirement may help the EPI sequence developer to identify the source of ghosts and artefacts.
The rigorous demand on the system hardware arises from the fact that the data are acquired from a train of echoes by one single RF excitation before the signal is destroyed by the T_2/T_2^* relaxation. The whole acquisition time for one slice of image in the human brain is normally limited to the T_2^* constant in the brain of approximately 70 msec. For an image of matrix size of N by N, the acquisition time for one echo τ is restricted to $\tau = \frac{T_2^*}{N}$. For example, an image of 64 by 64 pixels, it is around 1 msec, which is compa-

rably shorter than in any other conventional MR imaging sequences (Bowtell & Schmitt, 1998).

The spatial resolution of the image, FOV/N , is inversely proportional to the gradient strength G and the acquisition time for one echo τ as in Equation 2.4.

$$\frac{FOV}{N} = \frac{2 \cdot \pi}{\gamma \cdot G \cdot \tau} \tag{2.4}$$

As the acquisition time τ decreases, to maintain the same spatial resolution, the gradient strength G has to increase. However, in EPI the echoes are acquired by a fast switching gradient. If the spatial resolution is not to be compromised, it is necessary to reverse a large gradient very quickly. The large fast switching gradient system requires a highly efficient gradient coil of low inductance, and a powerful amplifier. This normally requires specially designed switching circuitry such as an EPI booster circuit. The design of an EPI booster circuit is crucial to the performance of EPI sequences in the scanner.

The time between each sampling point in the readout direction is $\frac{\tau}{N}$, which is less than 15 μsec in the above example. The analogue-to-digital converter needs to be very efficient. Current performance in most state of the art scanners is about 16 bit complex data sampling at a rate of 1 MHz.

The RF coil design needs to be optimized to give good SNR, a requirement which is not much different from the conventional MR imaging techniques. However, it needs to be ensured that any shielding screen used in RF coil does not produce eddy currents during the fast switching period of EPI readout. Otherwise this will lead to complicating ghosts in the image which are difficult to correct.

2.4 Diffusion Weighted MRI

Diffusion is the result of Brownian motion, which arises from the random thermal agitation for all particles at above absolute zero temperature. It has been of growing interest in the measurement of diffusion *in vivo* since the late 1980s. Diffusion weighted MR images provide important information in the early diagnosis of acute stroke and other neurological disorders. The availability of Echo Planar Imaging sequences to clinical MR scanners makes diffusion weighting imaging possible with satisfactory diffusion contrast and whole brain coverage within a few tens of seconds.
In the following section, the history and theory of DWI will be presented.

2.4.1 History of Diffusion Weighted MRI

Although early studies in the effect of diffusion on NMR by Hahn (Hahn, 1950) and Carr-Purcell (Carr & Purcell, 1954) etc suggest that NMR can be used to measure the value of self diffusion, it is the work of Stejskal and Tanner in 1965 (Stejskal & Tanner, 1965) that forms the foundation of most of the diffusion studies in MRI at this time. The experiment consists of a Spin Echo sequence with a pair of long duration gradients on both sides of the 180-degree RF pulse. The gradient amplitudes and durations are carefully calculated so that the dephasing from one gradient is completely rephased by the other after the 180 degree RF pulse for the static spins. Diffusion causes incomplete rephasing and a reduction in the net signal. The diffusion coefficient is then derived with Equation 2.12, which will be described in detail later.
Diffusion weighted MRI was successfully implemented using various fast MR imaging techniques (Taylor & Bushell, 1985; LeBihan *et al.*, 1986; LeBihan & Breton, 1985). Experiments using diffusion weighted EPI on human brain were first demonstrated by Turner et al (Turner *et al.*, 1990).

The applications of diffusion weighted MRI are mainly focused on two fields: stroke and fiber tracking, as described in Chapter 1. In 1990 Moseley et al demonstrated that a reduction of apparent diffusion coefficient can occur within 5 minutes of the onset of acute stroke, which is much earlier than changes in conventional T_1 or T_2 weighted images (Moseley *et al.*, 1990b). Combined with perfusion weighted MRI, the diffusion weighted image provides important information about diagnosis and therapy planning of stroke patients (Sorensen & Buonanno, 1996).

Further applications of diffusion weighted MRI result from the observation that the diffusion in human brain is mainly anisotropic in certain tissues (Pierpaoli & Basser, 1996). New techniques such as Diffusion Tensor Imaging (DTI) evolved from isotropic Diffusion Weighted MRI, which provides full characterisation of diffusion in all directions in biological environments (Basser *et al.*, 1994a). Because the diffusion in white matter in the brain mainly follows the direction of fiber tracts, it is potentially possible to map the direction of neuronal fibers with the information contained in the eigenmatrix of the measured diffusion tensor. The result from neuron fiber tracking offers important insight into the understanding of brain connectivity.

2.4.2 Fick's Laws of Diffusion

Fick's first law of diffusion states that the flux J of diffusing particles at position r in time t is proportional to the concentration gradient of the particles, ∇C. The proportionality constant D is the diffusion coefficient or diffusivity.

$$J(r,t) = -D \cdot \nabla C(r,t) \tag{2.5}$$

According to the law of conservation of mass, the rate of change of the concentration of the particles within a volume ΔV bounded by a surface dS can be expressed in Equation

2.6:

$$\frac{\partial C(r,t)}{\partial t} = -\frac{1}{\Delta V} \cdot \oint_s J(r,t) dS = -\nabla J(r,t) \tag{2.6}$$

This leads to Fick's second law of diffusion as in Equation 2.7:

$$\frac{\partial C(r,t)}{\partial t} = -\nabla J(r,t) = \nabla(D \cdot \nabla C(r,t)) = D \cdot \nabla^2 C(r,t) \tag{2.7}$$

To measure the diffusion coefficient, conventionally the concentration profile is monitored over a period of time using radioactive or fluorescent-labeled tracers. Such techniques have been applied successfully in biological tissues but because of their intrinsic invasiveness, they cannot be used in humans *in vivo*.

2.4.3 Einstein Equation

If the density of the particles at position r_0 is $\rho(r_0)$, the probability of finding the particle at position r moving from the original position r_0 after an observation time t is $P(r, r_0, t)$. The probability density can be expressed in Equation 2.8

$$P(r,t) = \int \rho(r_0) \cdot P(r_0, r, t) dr_0 \tag{2.8}$$

Fick's second law of Diffusion can be deduced for the probability density, as in Equation 2.9

$$\frac{\partial P(r_0, r, t)}{\partial t} = D \cdot \nabla^2 P(r_0, r, t) \tag{2.9}$$

In an isotropic medium, the self-diffusion can be expressed as in Equation 2.10

$$P(r_0, r, t) = \left(\frac{1}{\sqrt{(4\pi \cdot D \cdot t)}}\right)^3 \cdot e^{-\frac{(r-r_0)^2}{4Dt}} \tag{2.10}$$

The solution to Equation 2.10 leads to the Einstein Equation of Diffusion (Einstein, 1926) as in Equation 2.11

$$< (r - r_0)^2 >= 6 \cdot D \cdot t \tag{2.11}$$

The Einstein Equation of diffusion states that the mean square distance of movement of a particle from position r_0 to position r depends on the time of observation t. The diffusivity can be directly inferred from Einstein Equation by measuring the second moment of the conditional probability distribution of the diffusing particles. This approach is amenable to measurements using NMR and MRI.

2.4.4 Measuring Diffusion with MRI

The effect of water diffusion on the MR signal is mainly signal attenuation from spin dephasing. The signal attenuation is the result of gradient activity and diffusion.
The conventional way of measuring diffusion coefficient with MRI is using a simple pair of bipolar gradients in a Gradient Recalled Echo sequence or a pair of unipolar gradients on both sides of the refocusing 180-degree RF pulse in a typical Spin Echo type sequence. Figure 2.2 shows the structure of such a Spin Echo type diffusion weighted EPI sequence. The applied gradient will lead to additional spin dephasing and thus signal decay. If there is no diffusion in the medium, this additional signal dephasing will be refocused by the second gradient. The signal acquired during the readout period will only experience the spin-spin relaxation.
However, because the spins are diffusing, after the prolonged observation period of diffusion, the spins will have moved to a different position and be subjected to a different

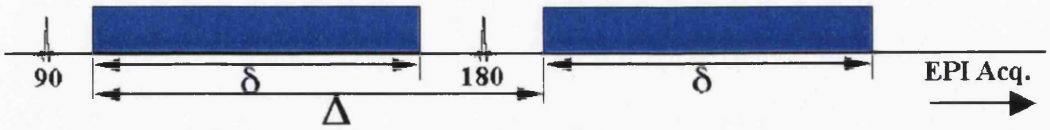

Figure 2.2: The figure shows the gradient activity and timing diagram of a typical diffusion weighted Spin Echo EPI sequence. The blue shaded area shows the activity of the diffusion weighting gradients.

magnetic field. Therefore the signal cannot be completely refocused. This leads to a signal attenuation due to the diffusion activity of spins.

Diffusion weighting can be added in both Gradient Recalled EPI and Spin Echo EPI sequences. The Gradient Recalled Echo type sequence, although it provides faster acquisition, tends to suffer from ghosts due to field inhomogeneity, especially after adding in the diffusion period. The shorter T_2^* relaxation and prolonged echo time lead to higher sensitivity to off-resonance artefacts. In a Spin Echo type acquisition, the refocusing 180 degree RF pulse reduces the sensitivity to field inhomogeneity. The slower intrinsic T_2 decay in the Spin Echo sequence can also improve the signal compared with the much faster T_2^* decay in the Gradient Recalled Echo sequence. To apply to diffusion measurements, all the sequences are implemented as Spin Echo type acquisition throughout this project.

The measured signal decay is a combination of both the intrinsic spin-spin relaxation and the diffusion attenuation. The logarithm of signal attenuation is proportional to the measured diffusion coefficient multiplied by a b-factor as in Equation 2.12, where $S(TE, b_1)$ and $S(TE, b_2)$ are the diffusion weighted signal measured at a certain Echo Time (TE) with different b-factors b_1 and b_2.

$$S(TE, b_1) = S(TE, b_2) \cdot e^{-(b_1 - b_2) \cdot D} \tag{2.12}$$

The b-factor is a constant which describes the sensitivity of the MR sequence to diffusion effects, including the strength, duration and the time separation of the diffusion weighting gradients. It is defined in the Equations 2.13 and 2.14

$$b = \int_0^{TE} \kappa(t') \cdot \kappa(t') dt' \tag{2.13}$$

$$\kappa(t) = \gamma \cdot \int_0^t G(t') dt' \tag{2.14}$$

where $G(t')$ is the effective gradient. In a Gradient Recalled Echo type experiment, the effective gradient in this equation has the same sign as the real gradient. In a Spin Echo type experiment, the sign of the effective gradient should be reversed after each 180 degree RF pulse.

If the ramp of the gradient can be ignored, the b-factor in a typical Spin Echo sequence, such as in Figure 2.2, can be calculated by a simple formula as in Equation 2.15

$$b = \gamma^2 \cdot G^2 \cdot \delta^2 \cdot (\Delta - \frac{\delta}{3}) \tag{2.15}$$

where G is the gradient strength and γ is the gyromagnetic ratio.

To measure the diffusion coefficient as in Equation 2.12, normally two images are acquired during the experiment. One is an image with strong diffusion weighting, while the other is a non- or low-diffusion weighted image acquired at the same echo time TE. Therefore the signal attenuation from the intrinsic spin-spin relaxation can be excluded in the calculation.

2.4.5 Choosing the b-factor

The choice of b-factor depends on several factors. During DTI sequence development, usually an optimised or desired b-factor is chosen. Because the b-factor of the sequence depends on the gradient strength and diffusion mixing time, the sequence is normally designed using the shortest echo time according to the maximum gradient that is available.

To increase the diffusion weighting, a larger b-factor is required. With the same gradient system available, the diffusion time has to increase, as was given in Equation 2.15. The final image will suffer longer T_2 relaxation and stronger diffusion attenuation and thus, be of much smaller SNR. The accuracy of diffusion measurement will be affected. It is thus essential to choose an optimised b-factor which provides appropriate diffusion weighting and maintains the best SNR in the images. Xing et al calculated the optimised b-factor according to the SNR in the diffusion weighted images (Xing *et al.*, 1997). Other optimal data collection schemes have been devised for isotropic media, or for the estimation of the ADC along one direction (Ahn *et al.*, 1986; Prasad & Nalcioglu, 1991). Armitage et al designed an optimised scheme based on the SNR in the calculated diffusion tensor trace map (Armitage & Bastin, 2001). All these works assumed a particular b-factor can be achieved within a short echo time. In the following section the relationship between the echo time and the b-factor will be taken into consideration in the optimization of the b-factor.

In MRI, the signal in the image depends on the T_2 relaxation and diffusion attenuation. It is difficult to estimate the original signal S_0, and the T_2 in the brain can vary over a range of 40 to 100 msec. The diffusion coefficient is obtained from the exponential signal decay curve between two measurements as in Equation 2.12. Here we rewrite as Equation 2.16.

$$D = \frac{1}{(b_1 - b_2)} \cdot \ln \frac{S(TE, b_2)}{S(TE, b_1)} \tag{2.16}$$

The error in the estimation of ADC, δD, is from the error in the measurements of $S(TE, b_1)$ and $S(TE, b_2)$ as in Equation 2.17.

$$\delta D = \sqrt{\left(\frac{\partial D}{\partial S(TE, b_1)}\right)^2 + \left(\frac{\partial D}{\partial S(TE, b_2)}\right)^2} \cdot \delta S(TE) \tag{2.17}$$

This leads to

$$\frac{\delta D}{\delta S(TE)} = \frac{1}{(b_1 - b_2)} \cdot \sqrt{\left(\frac{1}{S(TE, b_1)}\right)^2 + \left(\frac{1}{S(TE, b_2)}\right)^2} = \frac{e^{\frac{TE}{T_2}} \cdot e^{b_2 \cdot D}}{(b_1 - b_2) \cdot S_0} \cdot \sqrt{1 + e^{2 \cdot (b_1 - b_2) \cdot D}} \tag{2.18}$$

If we assumed that $b_2 \approx 0$ and $b = b_1$, we have to minimise the following expression:

$$N = \frac{e^{\frac{TE(b)}{T_2}}}{b} \cdot \sqrt{1 + e^{2 \cdot b \cdot D}} \tag{2.19}$$

The echo time TE depends on the b-factor chosen. In a Spin Echo experiment as in Figure 2.2, it is reasonable to assume that both Δ and δ are approximately equal to TE/2. The b-factor can thus be expressed as a function of echo time TE as

$$b = k \cdot TE^3 \tag{2.20}$$

$$\text{where } k = \tfrac{1}{12} \cdot \gamma^2 \cdot G^2$$

Thus, we have

$$TE(b) = \left(\frac{b}{k}\right)^{\frac{1}{3}} \tag{2.21}$$

and

$$b \cdot \frac{\partial TE(b)}{\partial b} = \frac{1}{3} \cdot \left(\frac{b}{k}\right)^{\frac{1}{3}} \tag{2.22}$$

The optimised b-factor occurs at

$$\frac{\partial N}{\partial b} \equiv 0 \tag{2.23}$$

$$\frac{b}{T_2} \cdot \frac{\partial TE(b)}{\partial b} + \frac{b \cdot D \cdot e^{2 \cdot b \cdot D}}{1 + e^{2 \cdot b \cdot D}} \equiv 1 \tag{2.24}$$

Figure 2.3 plots the value of N against b-factor for 10 different diffusion coefficients over a range of T_2 in the brain.

In our experiment, the maximum effective gradient used in the tetrahedral diffusion encoding scheme (Papadakis *et al.*, 1999) is $G_{max} = 16 \cdot \sqrt{2}mT/m$. If we assumed that the ADC is approximately $0.9 \cdot 10^{-9} m^2/sec$ and T_2 is about 100 msec in human brain, the optimised b-factor is approximately $998 \cdot 10^6 sec/m^2$ calculated from the figure.
In the following experiments, two sets of b-factors were used. The b-factors chosen were $992.88 \cdot 10^6 sec/m^2$ in the high diffusion weighted sequences and $96.96 \cdot 10^6 sec/m^2$ in the low diffusion weighted sequence. This will lead to a difference of the b-factors of $895.92 \cdot 10^6 sec/m^2$, which is quite close to the optimised value. The b-factor used in the selective averaging experiment is slightly lower at $868 \cdot 10^6 sec/m^2$ which will be described in more details in Chapter 4.

2.5 Diffusion Tensor Imaging

Diffusion tensor imaging is a further development of isotropic diffusion weighted imaging. It was noticed since the early development of DWI that diffusion in the biological environment is not isotropic, therefore the measured diffusion coefficients vary with the direction of the diffusion weighting gradients. To fully characterise the diffusion in the tissues, diffusion tensor imaging was developed, which has been successfully carried out in human brain showing diffusion anisotropy in biological tissues (Basser *et al.*, 1994a).

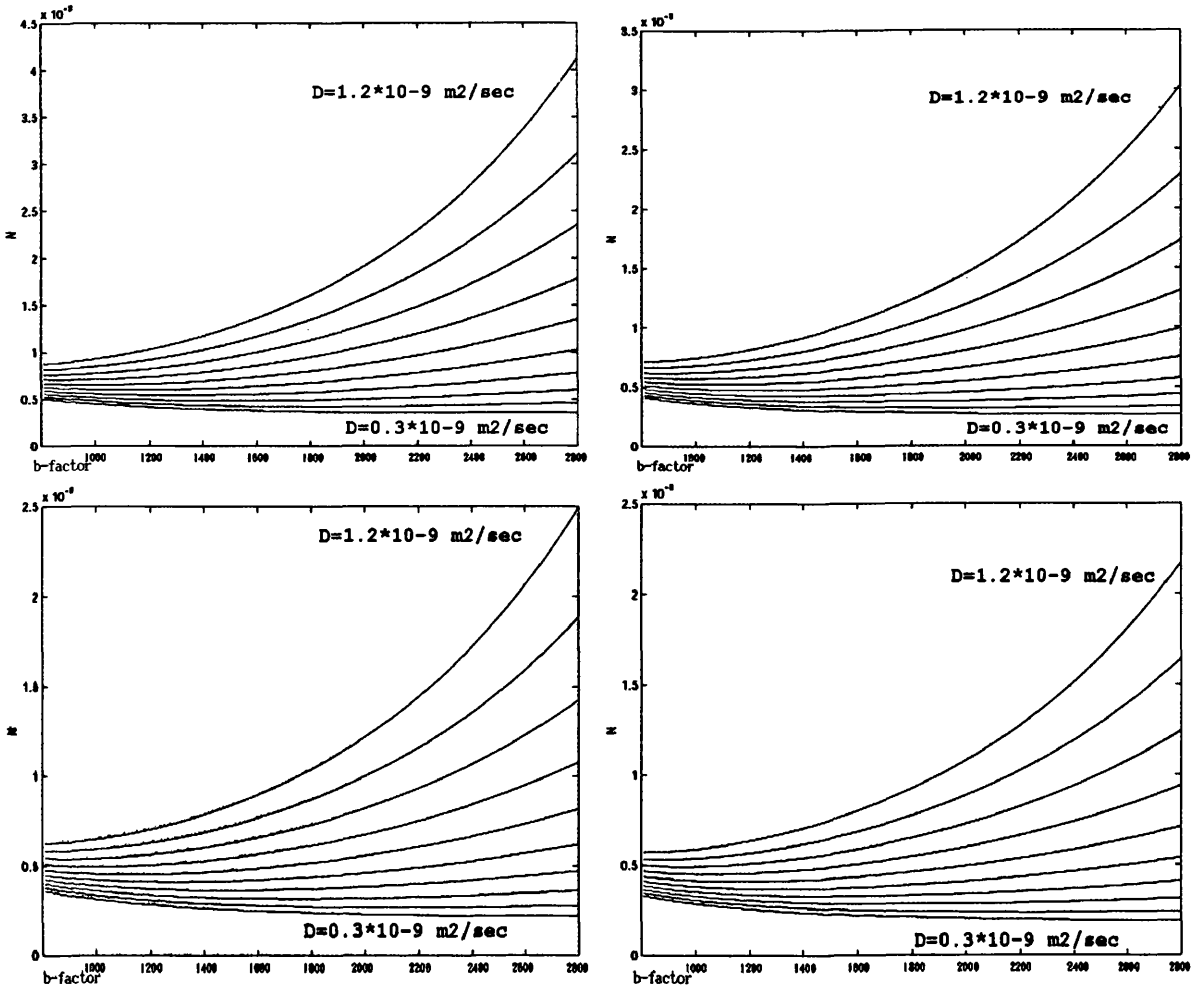

Figure 2.3: The figure plots the value of N against b-factor for 10 different diffusion coefficients ranging from $0.3 \cdot 10^{-9} m^2/sec$ to $1.2 \cdot 10^{-9} m^2/sec$ with increment of $0.1 \cdot 10^{-9} m^2/sec$ for a range of T_2. The b-factor is given in unit of $10^6 sec/m^2$.

Top Left: $T_2 = 70$ msec

Top Right: $T_2 = 90$ msec

Bottom Left: $T_2 = 110$ msec

Bottom Right: $T_2 = 130$ msec

2.5.1 Diffusion Anisotropy in Human Environment

The measurement of the diffusion coefficient from the Einstein Equation 2.11 assumes that the diffusing particles are in free motion. However, in biological tissues one cannot assume a homogeneously free environment. The diffusing particles within and between the cells are bound to hit obstacles, organelles and cell membranes etc. Considering a typical cell of size 10 μm in diameter, it takes less than 4 msec for the water molecule to reach the boundary from the centre of the cell, according to predictions from the Einstein Equation. However, the measured diffusion coefficient in the human brain is approximately $10^{-9} \cdot m^2/sec$, while the value measured in free water is considerably larger at approximately $3.5 \cdot 10^{-9} m^2/sec$. This suggests that hindrance to the mobility of molecules occurs within and between the cells. Thus the diffusion is no longer free and isotropic in the biological environment (Turner, 1998).

It is proposed that the semi permeable cell membrane acts as a major barrier to the diffusion within the tissue. Other structures such as organelles and protein molecules can obstruct the diffusing pathway as well. The measured diffusion coefficient is, thus, no longer dependent on the observation time described by the Einstein Equation. Instead, it depends on the geometry of the pathway or the homogeneity of the biological environment. Because generally no such *a priori* knowledge is available, the measured diffusion coefficient is described as 'Apparent' Diffusion Coefficient (ADC) (Tanner, 1978). The measurement of apparent diffusion coefficient will change with the direction of the diffusion weighting gradients.

2.5.2 Introduction to the Diffusion Tensor

The diffusion tensor consists of a 3 by 3 matrix which characterises the diffusion in all the directions as in Equation 2.25 (Basser *et al.*, 1994a; Basser *et al.*, 1994b; Basser & Pierpaoli, 1996).

$$D = \begin{pmatrix} D_{xx} & D_{xy} & D_{xz} \\ D_{yx} & D_{yy} & D_{yz} \\ D_{zx} & D_{zy} & D_{zz} \end{pmatrix} \tag{2.25}$$

The diffusion coefficient is positive definite. The measured diffusion coefficient in the xy direction is the same as the one in the yx direction and likewise for the diffusion coefficients measured in all the other off-diagonal directions. The components of the diffusion tensor in the diagonal directions define the diffusion in the three principal directions while the off-diagonal components describe the effect of correlation among the perpendicular diffusion weighting directions.

Fick's law of diffusion can be extended to the diffusion tensor form as in the following Equations 2.26 and 2.27:

$$\begin{pmatrix} J_x(x,y,z,t) \\ J_y(x,y,z,t) \\ J_z(x,y,z,t) \end{pmatrix} = \begin{pmatrix} D_{xx} & D_{xy} & D_{xz} \\ D_{yx} & D_{yy} & D_{yz} \\ D_{zx} & D_{zy} & D_{zz} \end{pmatrix} \times \begin{pmatrix} \frac{\partial c(x,y,z,t)}{\partial x} \\ \frac{\partial c(x,y,z,t)}{\partial y} \\ \frac{\partial c(x,y,z,t)}{\partial z} \end{pmatrix} \tag{2.26}$$

And

$$\begin{pmatrix} \frac{\partial c(x,y,z,t)}{\partial t} \\ \frac{\partial c(x,y,z,t)}{\partial t} \\ \frac{\partial c(x,y,z,t)}{\partial t} \end{pmatrix} = \begin{pmatrix} D_{xx} & D_{xy} & D_{xz} \\ D_{yx} & D_{yy} & D_{yz} \\ D_{zx} & D_{zy} & D_{zz} \end{pmatrix} \times \nabla^2 \begin{pmatrix} c(x,y,z,t) \\ c(x,y,z,t) \\ c(x,y,z,t) \end{pmatrix} \tag{2.27}$$

2.5.3 Definition of b-matrix

The diffusion process can be described by 6 independent parameters: the 3 eigenvalues of the diffusion tensor D and 3 additional parameters defining the transformation between

the coordinate systems of the eigenmatrix of the tensor and the scanner. This requires at least six measurements with various non-linear diffusion encoding directions and one additional measurement without diffusion weighting to obtain the value $S(TE, b_{low})$ (Basser & Pierpaoli, 1998). With Equation 2.12, diffusion in the biological environment can be expressed as in Equation 2.28

$$\ln(\frac{S(TE,b_m)}{S(TE,b_{low})}) = \begin{pmatrix} b_{xx} & b_{xy} & b_{xz} \\ b_{yx} & b_{yy} & b_{yz} \\ b_{zx} & b_{zy} & b_{zz} \end{pmatrix} \times \begin{pmatrix} D_{xx} & D_{xy} & D_{xz} \\ D_{yx} & D_{yy} & D_{yz} \\ D_{zx} & D_{zy} & D_{zz} \end{pmatrix} \tag{2.28}$$

where $S(TE, b_m)$ is the signal acquired from the mth measurement and the $S(TE, b_{low})$ is the signal with low or non diffusion weighting acquired at the same echo time TE.
In the Spin Echo experiment as described in the previous example in Figure 2.2, the elements $b_{ij,for i,j=x,y,z}$ in the b-matrix of Equation 2.28 can be calculated from Equation 2.29

$$b_{ij} = \gamma^2 \cdot \mid \vec{G_i} \mid \cdot \mid \vec{G_j} \mid \cdot \delta^2 \cdot (\Delta - \frac{\delta}{3}) \tag{2.29}$$

Where $\vec{G_i}$ and $\vec{G_j}$ are the diffusion weighting gradients applied in the i and j directions respectively.

2.5.4 Display of the Diffusion Tensor

As a 3 by 3 matrix, it is generally difficult to visualise the diffusion tensor in a grayscale image. Several approaches have been developed to display the tensor as colour-encoded (Douek *et al.*, 1991; Jones *et al.*, 1997; Pajevic & Pierpaoli, 1999) or as elongated ellipsoids (Basser *et al.*, 1994b). It is also helpful to extract some intrinsic information from the diffusion tensor matrix and display this as individual grayscale images.

Eigenmatrix of the Diffusion Tensor

The orientation of the intrinsic diffusion in the human environment is generally different from the directions used in the diffusion encoding scheme during the measurements. The diffusion tensor is diagonal in a coordinate system the axes of which are given by the eigenvectors of the tensor matrix D. After acquiring the full diffusion tensor, it is necessary to rotate the tensor matrix to its eigenmatrix. The directions of the three eigenvectors $\lambda_1, \lambda_2, \lambda_3$ point to the real directions of the principal diffusions and the corresponding eigenvalues $\epsilon_1, \epsilon_2, \epsilon_3$ show the diffusion in the respective direction. The eigenvalues thus can reflect the true diffusion in different directions within the voxel of interest.

The eigenvalues are often sorted according to the absolute values. In an ideally isotropic environment such as free water, the three eigenvalues should be the same. Yet, in biological tissues, the absolute values of the sorted eigenvalues can vary within a wide range and the largest eigenvalues can be up to ten times the smallest eigenvalues. Thus eigenvalues of the diffusion tensor matrix provide a good way to measure the diffusion anisotropy in the biological environment.

The Diffusion Tensor as Ellipsoids

One of the most straightforward ways of displaying the diffusion tensor is to depict it as an ellipsoid on a voxel by voxel basis as shown in Figure 2.4 (Basser *et al.*, 1994b; Basser *et al.*, 1995).

The three principal axes of the diffusion ellipsoid are aligned with the directions of the three eigenvectors of the diffusion tensor. The lengths of the principal axes are the corresponding eigenvalues. The surface of the ellipsoids describes the probability distribution of the particles observed after a unit time when placed in the centre of the voxel.

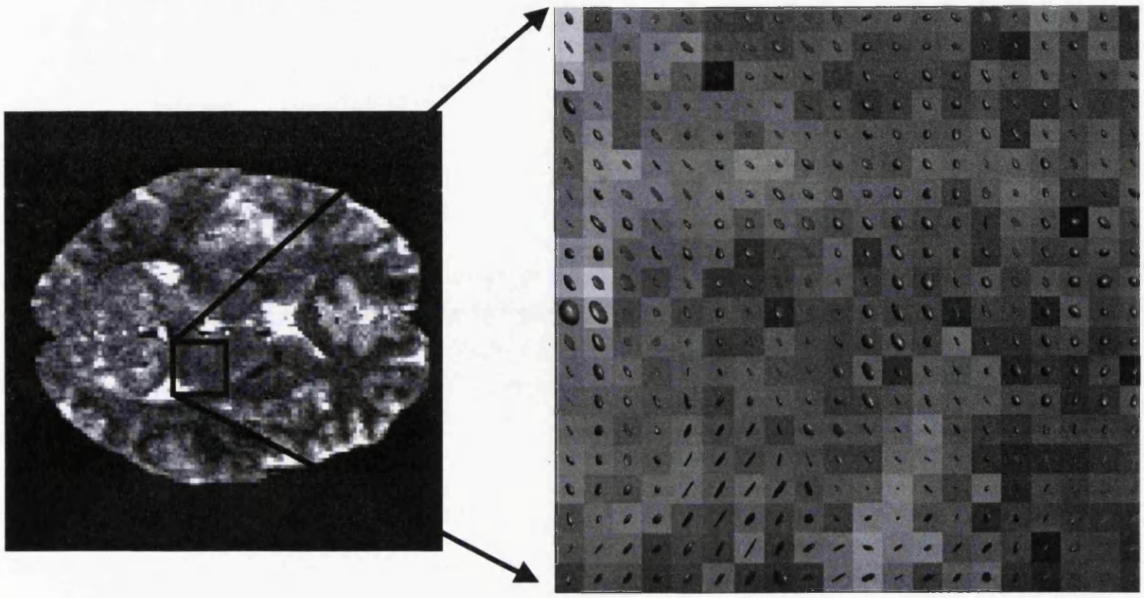

Figure 2.4: Diffusion tensor shown as ellipsoids in an enlarged area.
Left: One slice of the trace image.
Right: Diffusion tensor displayed an ellipsoids in an enlarged ROI.

Although the ellipsoid is effective at showing the size and orientation of the diffusion tensor qualitatively, it is not straightforward to perceive as an grayscale image.

2.5.5 Trace of the Diffusion Tensor

The trace of the diffusion tensor is defined as the sum of the three principal components of the diffusion tensor as in Equation 2.30 (Kärger *et al.*, 1988):

$$Trace(D) = \epsilon_1 + \epsilon_2 + \epsilon_3 \tag{2.30}$$

The trace of the diffusion tensor reflects the part of diffusion that is isotropic and thus does not change with the coordinate system of reference. The trace is rotationally

invariant and provides an estimation of the bulk diffusion.

Interestingly, though the ADCs measured in white matter, gray matter and CSF in human brain are different, the image of trace looks relatively uniform. Typical trace values measured in the brain (Shimony *et al.*, 1999) are around $2.17{\cdot}10^{-9}m^2/sec$ in ROIs in Splenium of Corpus Callosum and $2.16{\cdot}10^{-9}m^2/sec$ in Genu of Internal Capsule in white matter. In gray matter it is around $2.39{\cdot}10^{-9}m^2/sec$ in ROIs in the head of Caudate Nucleus and $2.65{\cdot}10^{-9}m^2/sec$ in Frontal GM.

Throughout the project, the trace is presented as the mean value of the bulk diffusion, trace/3, which reflects the isotropic component of the diffusion.

Figure 2.5 shows the trace and three sorted eigen images from the same slice in the human brain displayed on the same windowed scale.

2.5.6 Characterising Diffusion Anisotropy

There have been several different ways to characterise diffusion anisotropy in the human brain. Some definitions of diffusion anisotropy are rotationally variant, and are thus susceptible to the changes in the diffusion encoding scheme. Others are rotationally invariant, and remains constant regardless of the orientation of the coordinate system of reference used for diffusion weighting gradients.

The ratios of the eigenvalues reflect the extent of diffusion anisotropy. They are the most intuitive and simplest way to characterise the diffusion anisotropy as defined in Equation 2.31(Douek *et al.*, 1991) and 2.32 (Pierpaoli & Basser, 1996).

$$volume\ ratio_1 = \frac{\epsilon_1}{\epsilon_3} \tag{2.31}$$

$$volume\ ratio_2 = \frac{2 \cdot \epsilon_1}{\epsilon_2 + \epsilon_3} \tag{2.32}$$

However, such ratios tend to suffer from accumulated errors in the sorting of the eigen-

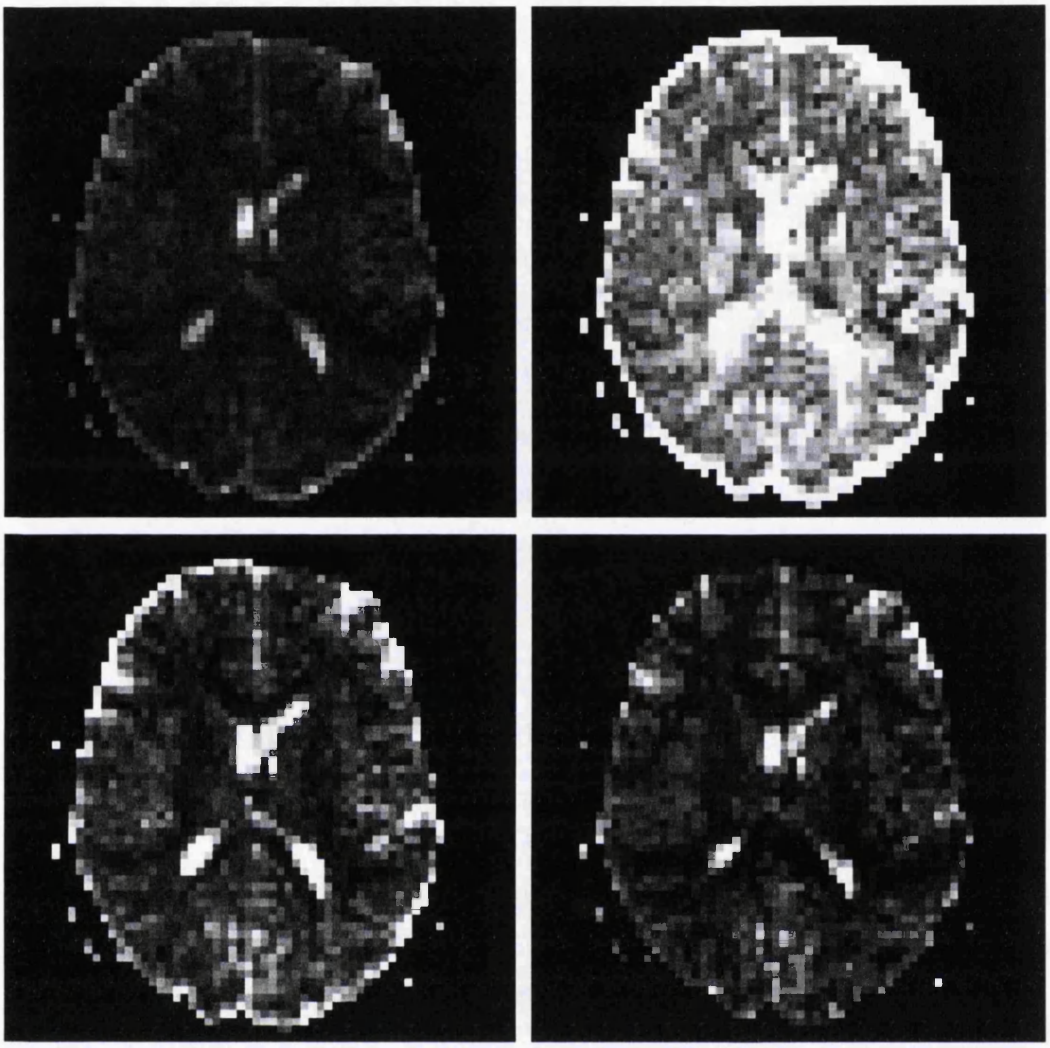

Figure 2.5: The figure shows the trace image and three sorted eigenimages of the same slice. Images are acquired with the same parameters used in the *in vivo* experiment in Chapter 3: using a single shot EPI sequence, matrix size of 64 by 64, isotropic voxel size of 3 mm, standard diffusion encoding as described in Section 2.4. Images are displayed at the same windowing scale.

Top Left: Image of the trace/3 from one slice of the brain.

Top Right: Image of the largest eigenvalue from the same slice.

Bottom Left: Image of the second largest eigenvalue from the same slice.

Bottom Right: Image of the smallest eigenvalue from the same slice.

values, and are thus particularly susceptible to the low SNR of the diffusion weighted images (Mehta, 1991; Ahrens *et al.*, 1998).

Relative Anisotropy (RA) and Fractional Anisotropy (FA) are both rotationally invariant and independent of the order of the eigenvalues, which avoids the sorting errors as encountered in Equation 2.31 and 2.32 (Basser & Pierpaoli, 1996).

Relative Anisotropy is the ratio of the anisotropic component divided by the isotropic component of the diffusion tensor as in Equation 2.33. Similarly, Fractional Anisotropy is defined in Equation 2.34.

$$RA = \frac{\sqrt{(\epsilon_1 - \epsilon_2)^2 + (\epsilon_2 - \epsilon_3)^2 + (\epsilon_3 - \epsilon_1)^2}}{(\epsilon_1 + \epsilon_2 + \epsilon_3)} \tag{2.33}$$

$$FA = \frac{\sqrt{(\epsilon_1 - \epsilon_2)^2 + (\epsilon_2 - \epsilon_3)^2 + (\epsilon_3 - \epsilon_1)^2}}{\sqrt{2 \cdot (\epsilon_1{}^2 + \epsilon_2{}^2 + \epsilon_3{}^2)}} \tag{2.34}$$

Both RA and FA are quantitative and dimensionless. They are physically meaningful and rotationally invariant. For isotropic medium, both RA and FA are 0. For cylindrically symmetric anisotropic medium, FA is 1. Figure 2.6 shows images of Fractional Anisotropy and Relative Anisotropy from the human brain. We can see clearly that it is dark in the more isotropic regions such as CSF in the ventricle, which is mainly water, and bright in the anisotropic regions such as in Corpus Callosum where diffusion mainly follows the direction of the neuron fibers. In this project, Fractional Anisotropy is used as an index to characterise the extent of diffusion anisotropy.

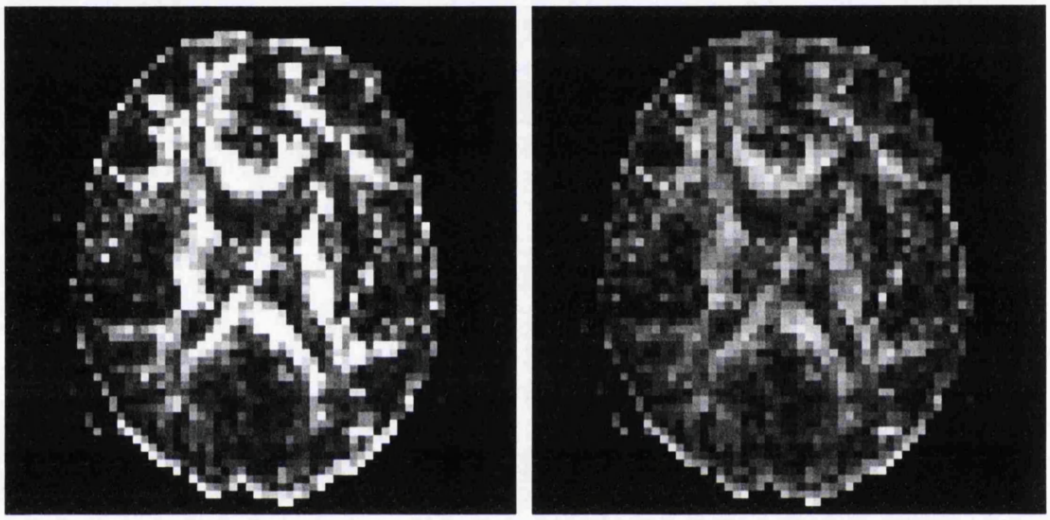

Figure 2.6: The figure shows one slice of brain images of the Relative Anisotropy map and Fractional Anisotropy map. Parameters used are the same as in Figure 2.5.
Left: Relative Anisotropy map
Right: Fractional Anisotropy map

2.6 Protocols in Measuring the Diffusion Tensor

In this project, all the experiments were carried out in a 2 Tesla MRI whole body scanner (Siemens Magnetom Vision, Erlangen Germany) in a passively shielded magnet. The maximum gradient strength available is 25 mT/m.

The water phantom used in the experiments is a standard phantom made by Siemens Erlangen. It is made of 2.571 liter of water in a spherical container doped with 1.25 g $NiSO_4 \cdot 6H_2O$.

A gel phantom was made and used in the experiments as well. It was stored in a spherical container and doped with 6.65 % Acrylamide, 0.35 % Bisacrylamide, 0.1 % Ammonium Persulphate and 0.076 % TEMED. The recipe was proposed by Dr. Denis LeBihan from Commissariat a l'Energie Atomique, Orsay, France, through private communication.

The processing of the raw data, including the extraction of phase information from the navigator echoes, correction of the phase evolution in the raw data, the image reconstruction and the calculation of the diffusion tensor images and the Fractional Anisotropy maps was all implemented by the author and performed with MATLAB (The Mathworks, Natick, Mass., USA).

When it is necessary to select a Region Of Interest (ROI), it was drawn by hand along the boundary of the structure of interest or in a region as large as possible yet without inclusion of overlapping ghosts. The size of the ROI thus varied. In a multiple measurement, the first measurement was used if not specified in the text.

None of the data from separate scans were co-registered except those particularly specified. This is to avoid rotation of the diffusion tensor.

Two diffusion encoding schemes are used in the project. The first scheme is called the standard diffusion encoding scheme as shown in Table 2.1 (Basser & Pierpaoli, 1998). Six high diffusion weighted measurements with different directions of the diffusion weighting gradients were performed for each image section providing significant diffusion attenuation along the three orthogonal axes in phase encoding, slice selection and read out

Order of measurements	Read Out	Phase Encoding	Slice Selection
1	G	0	0
2	0	G	0
3	0	0	G
4	$\frac{G}{\sqrt{2}}$	$\frac{G}{\sqrt{2}}$	0
5	$\frac{G}{\sqrt{2}}$	0	$\frac{G}{\sqrt{2}}$
6	0	$\frac{G}{\sqrt{2}}$	$\frac{G}{\sqrt{2}}$

Table 2.1: The table shows the strength and directions of the diffusion weighting gradients in the standard diffusion encoding scheme from six high diffusion weighted measurements. G is the strength of the diffusion weighting gradient.

directions and three off-orthogonal axes along the combined direction of the phase encoding/ slice selection, phase encoding/ read out and slice selection/ read out directions.

In the second scheme, the diffusion weighting gradients are applied to the tetrahedral directions as in Table 2.2 and was referred to as the tetrahedral diffusion encoding scheme throughout the project (Papadakis *et al.*, 1999).

One low diffusion-weighted measurement was conducted with diffusion weighting along the three orthogonal directions.

Order of measurements	Read Out	Phase Encoding	Slice Selection
1	-G	G	0
2	-G	0	G
3	G	G	0
4	G	0	G
5	0	-G	G
6	0	G	G

Table 2.2: The table shows the strength and directions of the diffusion weighting gradients in the tetrahedral diffusion encoding scheme from six high diffusion weighted measurements. G is the strength of the diffusion weighting gradient.

Chapter 3

Single Shot Diffusion Tensor EPI

To demonstrate the stability and reproducibility of the diffusion tensor imaging, standard single shot EPI was used as the template. Diffusion weighting gradients were added in 6 directions using the standard diffusion encoding scheme as described in Section 2.6 in Chapter 2. The acquisition time per echo was 1024 μs, and the matrix size was 64 by 64. The field of view was 192 mm by 192 mm and the slice thickness was 3 mm, resulting in an isotropic voxel size of 3 mm. The sequence was tested *in vitro* on a water phantom and *in vivo* on six healthy volunteers which was repeated twice.

For high diffusion weighted measurements, 15 averages of each measurement were obtained. For low diffusion weighted measurements, 12 averages were measured. The effective echo time was 102 msec and the k-space was sampled asymmetrically by acquiring the central k-space line after 25 % of the EPI echo train acquisition, thus reducing the echo time (Hennel & Nedelec, 1995).

The b factors chosen were 923 $\cdot 10^6 sec/m^2$ for measurements in the 3 principal directions, and 461 $\cdot 10^6 sec/m^2$ for measurements along the off-diagonal directions. The b-factor for the low diffusion weighting measurement was 117 $\cdot 10^6 sec/m^2$.

3.1 Phantom Study

In the phantom study, a Siemens phantom made from doped water was used in all the experiments. The values of the trace/3, eigenvalues, Fractional Anisotropy of the tensor from a region of interest are shown in Table 3.1. The diffusion coefficient measured at 1 ATM and 20 Celsius degree was $1.95{\cdot}10^{-9}m^2/sec$, which is close to the value of $2.05 \cdot 10^{-9}m^2/sec$ for pure water reported by Harris et al (Harris & Woolf, 1980) under similar conditions. The measured Fractional Anisotropy of 0.12 shows reasonable low directionality in free water, which is comparable to the simulated data from Pierpaoli et al for isotropic material (Pierpaoli & Basser, 1996).

Figure 3.1 and Figure 3.2 show the calculated tensor images of the phantom. Both the trace image and the images of eigenvalues are relatively ghost free. All the images of the eigenvalues are quite similar, which suggests low anisotropy, as expected. Fractional Anisotropy maps show that the phantom has low diffusion anisotropy inside the phantom with a bright ring at the edge, which could be due to vibration of the scanner bed during the data acquisition, residual eddy current or a susceptibility artefact.

3.2 Study on Healthy Volunteers

To study the reproducibility of the sequences on humans, 6 healthy volunteers, including four male and two female (aged 33.5 $\pm$ 5.54 years old, between 26 to 40) were scanned twice with the same protocol. After data processing, 8 parameters are presented here for comparisons: Fractional Anisotropy, trace/3, three sorted eigenvalues and three apparent diffusion coefficients along the main axes.

ROIs in white matter (Posterior Corpus Callosum), gray matter (Pericalcarine) and CSF in the ventricles were drawn by hand for six subjects. The mean values and standard deviation from both sessions are presented in Table 3.2. Figure 3.3 and Figure 3.4 plot the mean and standard deviation of the calculated trace/3 and Fractional Anisotropy in

Parameter of Interest	Mean ± Standard Deviation
Trace/3	1.95 ± 0.08
1st EigenValue	2.15 ± 0.08
2nd EigenValue	1.89 ± 0.06
3rd EigenValue	1.80 ± 0.07
Tensor in xx direction	1.89 ± 0.07
Tensor in yy direction	1.87 ± 0.06
Tensor in zz direction	2.08 ± 0.06
Tensor in xy direction	-0.03 ± 0.05
Tensor in xz direction	0.06 ± 0.06
Tensor in yz direction	-0.11 ± 0.03
Fractional Anisotropy	0.12 ± 0.03

Table 3.1: The table shows the measured diffusion tensor, trace/3, Fractional Anisotropy and the eigenvalues from a doped water phantom. Diffusion coefficients are in units of $10^{-9}m^2/sec$. Fractional Anisotropy is dimensionless.

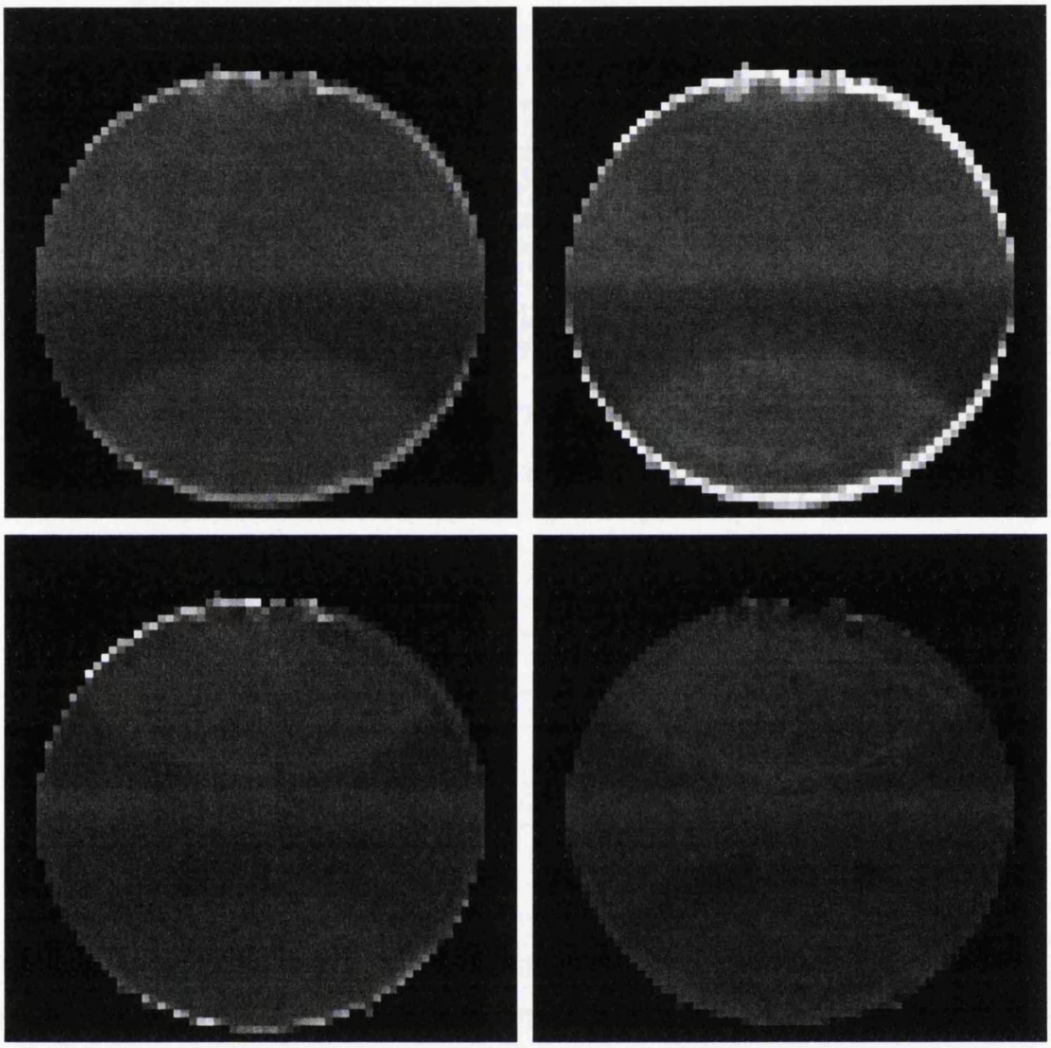

Figure 3.1: The figure shows the trace and eigenimages acquired by the single shot EPI sequences.

Top Left: The trace image

Top Right: The first eigenimage

Bottom Left: The second eigenimage

Bottom Right: The third eigenimage

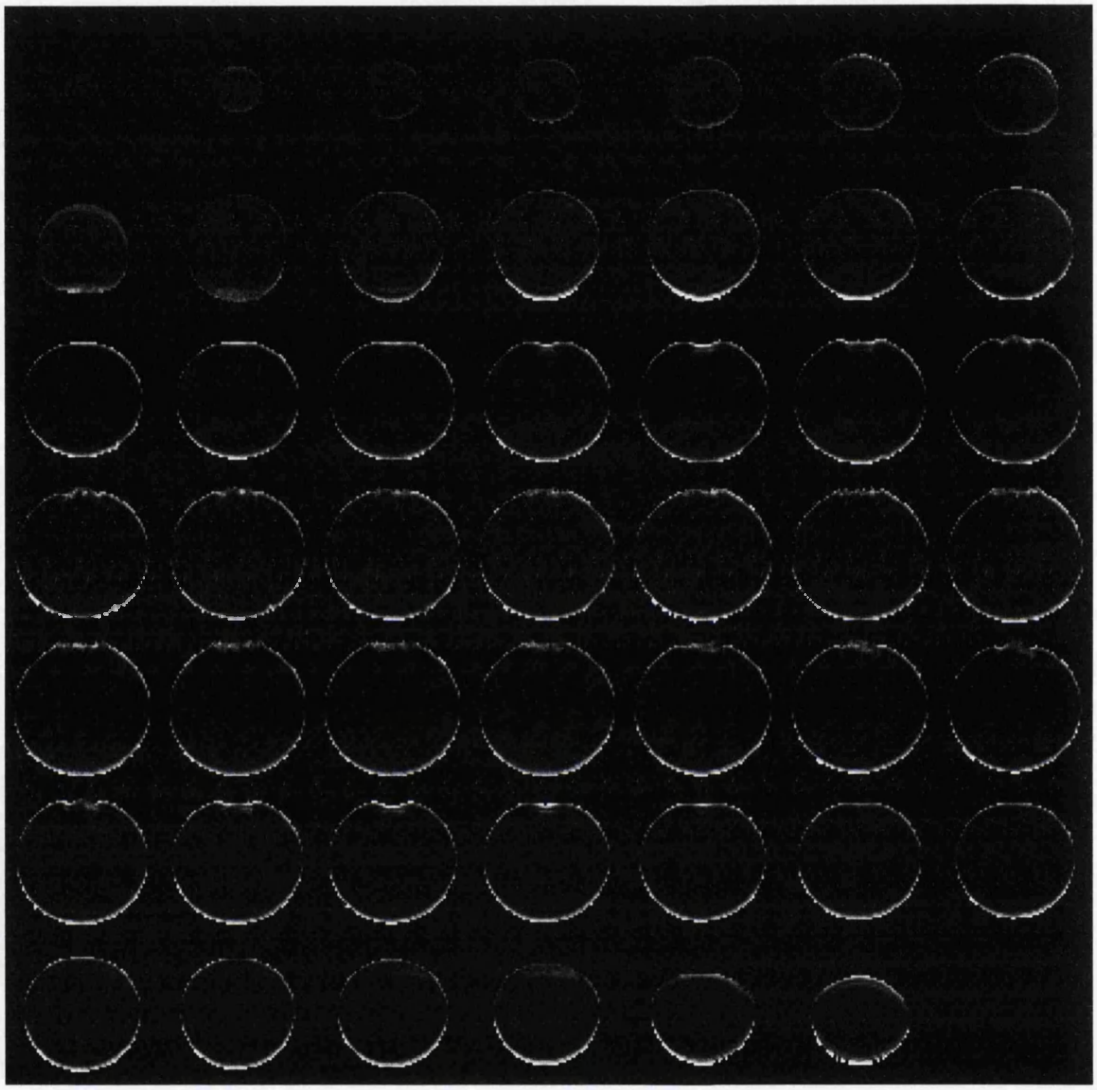

Figure 3.2: The figure shows 48 slices of the calculated Fractional Anisotropy map of the phantom acquired by the single shot EPI sequences.

the ROIs.

The mean values of Fractional Anisotropy in white matter 0.92, and in gray matter 0.31, are higher than the values reported by other groups (0.73 in Splenium Corpus Callosum and 0.20 in the head of Caudate Nucleus) (Shimony *et al.*, 1999). The variation among the six subjects in the calculated Fractional Anisotropy is larger in gray matter (19.8 % for the first measurement and 18.1 % for the second measurement) and CSF (28.9 % and 16.2 % respectively) than white matter (3.8% and 3.7 % respectively). The variation in the trace is similar among different ROIs in the six subjects, which is approximately 10 %.

The relative deviation Δ between two measurements is calculated for the Fractional Anisotropy, trace/3 and the first eigenvalue for all the six subjects. It was calculated as the squared root of the square of the differences divided by the mean values: $\Delta = \frac{2 \cdot \sqrt{(measurement_2 - measurement_1)^2}}{measurement_1 + measurement_2}$. Table 3.3 shows the Δ in % in three ROIs described above.

The variation between the measurements in various tissue types of the brain shows satisfactory reproducibility in the case of the single shot DT-EPI sequences. The variation among the subjects and between measurements can be affected by several factors such as the variations in the choice of ROIs, tissue type, the SNR in the original diffusion weighted images and the intrinsic reproducibility of the sequence. In Table 3.3, there is no clear difference between the results in different ROIs. The parameters in CSF should be close to that of pure water. The variation between measurements in CSF is probably caused by motion artefact associated with pulsatile inflow. Here CSF in general shows greatest variations in these parameters between measurements.

Single shot diffusion tensor imaging is stable among the subjects and between measurements in our scanner. In the following study, it also provides important information in the diagnosis and assessment of recovery of the stroke patient.

Parameters	Posterior Corpus Callosum		Pericalcarine	
	1st session	2nd session	1st session	2nd session
1st Eigenvalue	1.39 ± 0.17	1.40 ± 0.12	1.20 ± 0.12	1.16 ± 0.08
2nd Eigenvalue	0.42 ± 0.08	0.42 ± 0.07	0.96 ± 0.11	0.93 ± 0.08
3rd Eigenvalue	0.04 ± 0.09	0.04 ± 0.09	0.75 ± 0.10	0.75 ± 0.10
Tensor in xx direction	0.92 ± 0.16	0.94 ± 0.13	0.97 ± 0.09	0.92 ± 0.09
Tensor in yy direction	0.43 ± 0.12	0.46 ± 0.10	0.95 ± 0.12	0.92 ± 0.07
Tensor in zz direction	0.50 ± 0.04	0.46 ± 0.04	1.00 ± 0.11	0.99 ± 0.09
Trace/3	0.63 ± 0.07	0.63 ± 0.07	0.97 ± 0.10	0.94 ± 0.08
Fractional Anisotropy	0.91 ± 0.03	0.92 ± 0.03	0.31 ± 0.06	0.31 ± 0.05

	CSF	
	1st session	2nd session
1st Eigenvalue	3.39 ± 0.38	3.39 ± 0.44
2nd Eigenvalue	2.82 ± 0.35	2.79 ± 0.50
3rd Eigenvalue	2.28 ± 0.40	2.27 ± 0.40
Tensor in xx direction	2.74 ± 0.36	2.69 ± 0.53
Tensor in yy direction	2.91 ± 0.48	2.80 ± 0.35
Tensor in zz direction	2.85 ± 0.37	2.96 ± 0.50
Trace/3	2.83 ± 0.36	2.82 ± 0.44
Fractional Anisotropy	0.26 ± 0.08	0.26 ± 0.04

Table 3.2: The table shows the measured ADC in the principle directions of the diffusion tensors, the three sorted eigenvalues, trace/3 and calculated Fractional Anisotropy from ROIs in Corpus Callosum, Pericalcarine area and ventricles as mean ± standard deviation, in units of $10^{-9}m^2/sec$. Fractional Anisotropy is dimensionless.

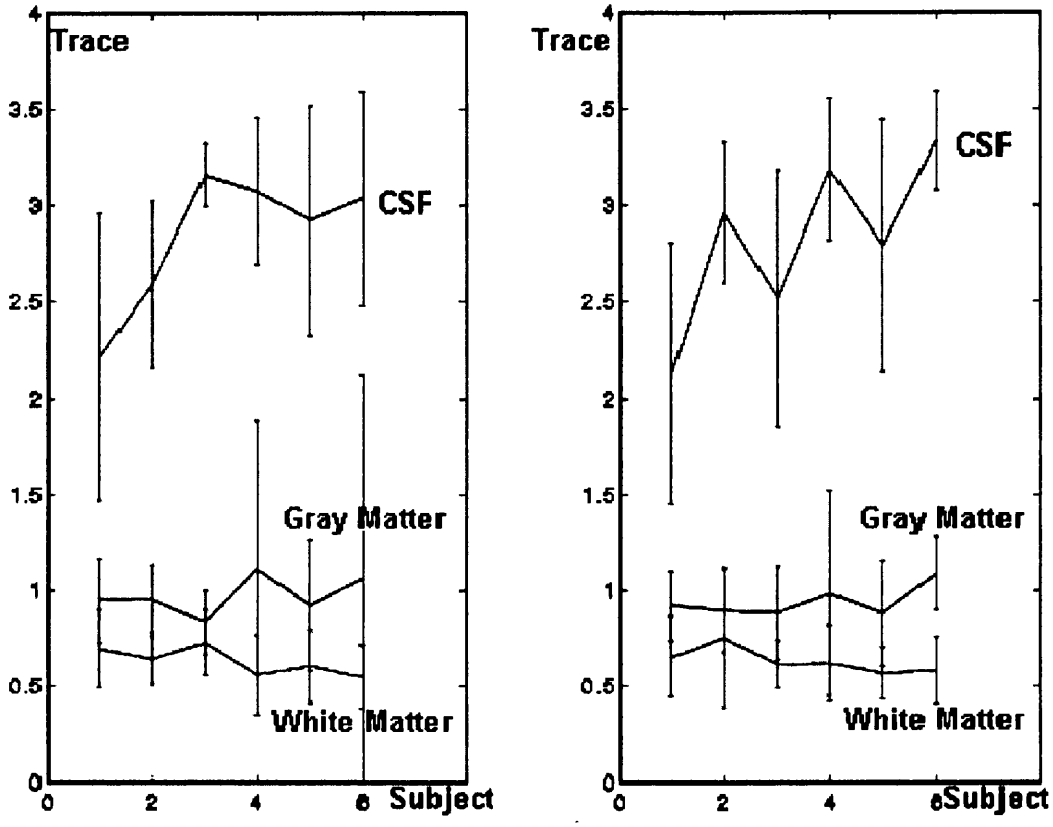

Figure 3.3: The figure shows the calculated trace/3 between two measurements among the six healthy subjects in different ROIs. The values are given in units of $10^{-9}m^2/sec.$
Left: First Measurement
Right: Second Measurement

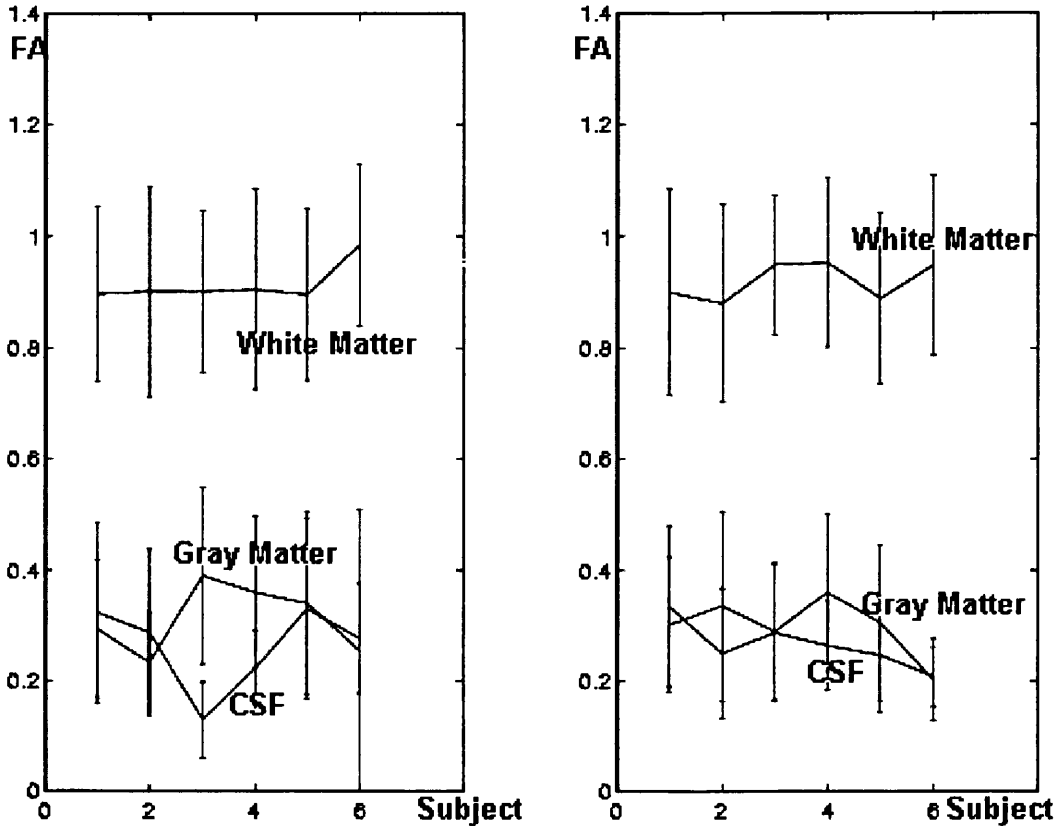

Figure 3.4: The figure shows the calculated Fractional Anisotropy from two measurements among the six healthy subjects in different ROIs.

Left: First Measurement

Right: Second Measurement

Parameters	Posterior Corpus Callosum	Pericalcarine	CSF
1st Eigenvalue	7.25 %	2.48%	7.55%
Trace/3	10.31%	5.84%	9.56%
Fractional Anisotropy	2.95%	17.08%	28.07%

Table 3.3: The table shows the fractional differences of the calculated Fractional Anisotropy, trace/3 and the sorted first eigenvalue between two independent measurements in different ROIs, averaged across the six healthy subjects.

3.3 Study on A Stroke Patient

Hindered or restricted diffusion as described in Section 2.5.1 in Chapter 2 occurs in the human environments because of the cell structures such as membranes and organelles. It will be altered or disrupted because of any pathologic process which disrupts cell membranes. The bulk diffusion and diffusion anisotropy will be changed accordingly. The change of the diffusion characteristic in the human brain thus marks the disintegration of the neurological structure. Diffusion tensor imaging provides crucial information in this regard as mentioned in Chapter 1.

One stroke patient was imaged with the single shot diffusion tensor EPI sequences. The patient is a 30 year old male with left sided Pons infarct. The site of insult is shown in Figure 3.5. The first attack was in November 2000. He was first scanned 4 weeks later in December 2000. The second scan took place in April 2001, which is 21 weeks after the stroke.

Table 3.4 shows the calculated trace/3 and the Fractional Anisotropy from ROIs in the

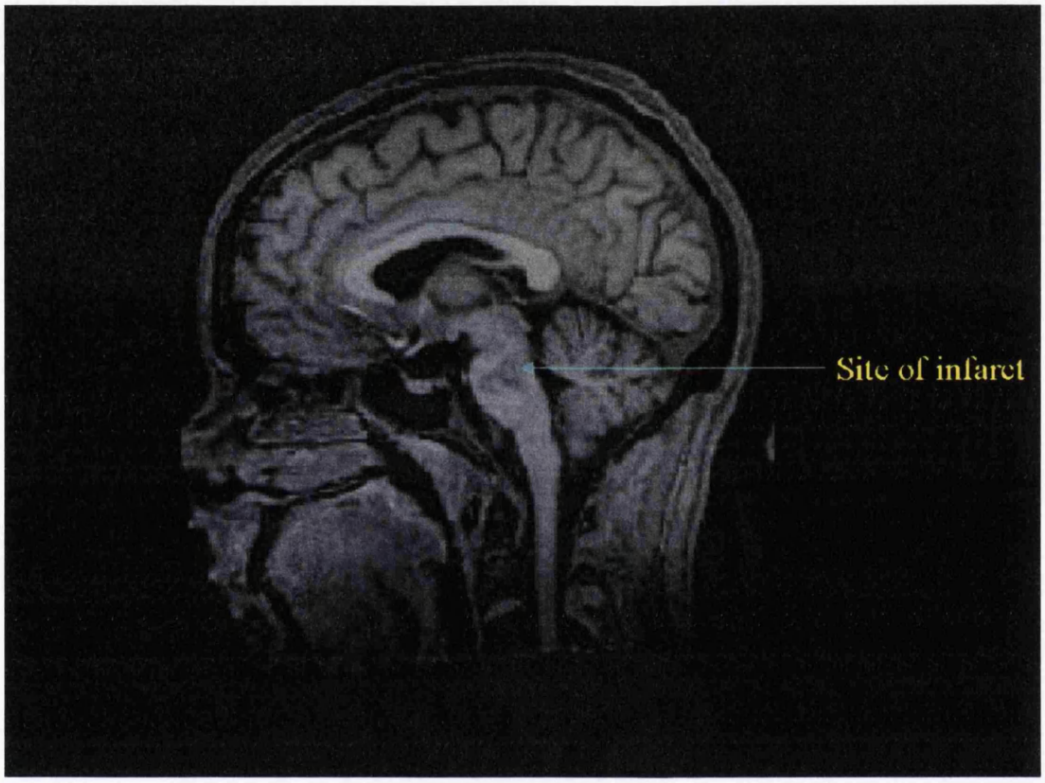

Figure 3.5: The figure shows the site of infarct in the left side Pons in the stroke patient

	Trace/3, in units of $10^{-3}\, mm^2/sec$		Fractional Anisotropy	
	Infarct	Normal	Infarct	Normal
First Session	1.53 ± 0.22	0.68 ± 0.15	0.16 ± 0.06	0.43 ± 0.13
Second Session	1.11 ± 0.27	0.74 ± 0.16	0.27 ± 0.15	0.74 ± 0.24

Table 3.4: The table shows the calculated trace/3 and Fractional Anisotropy in the regions of infarct and in nearby normal tissues from the two independent measurements.

infarct region and nearby normal tissues during the two independent measurements. The region of infarct was chosen from one slice of the images after comparing the structural images, the trace images and Fractional Anisotropy, and the region was carefully drawn by hand with the help of the attending clinician. The region containing the normal tissue was selected by hand from the Pons in the contralateral position. Fractional Anisotropy is clearly reduced and the trace increased in the region of infarct, compared with the normal tissue. Figure 3.6 shows the increase of trace/3 and decrease of Fractional Anisotropy in the affected area compared with nearby normal tissues. Figure 3.7 shows the changes in a similar area 17 weeks after the first scan.

The underlying mechanism for the change of the trace and Fractional Anisotropy is still under debate. The increase of trace is consistent with previous reports of increased water diffusion after the acute phase (> 10 days) of cerebral infarction (Lutsep *et al.*, 1997). The decrease of Fractional Anisotropy has been previously reported by Werring et al (Werring *et al.*, 2000). It is thought that cell lysis and loss of normal tissue architecture expand the extracellular space which allows water molecules to diffuse more freely (Knight *et al.*, 1994). The calculated values of Fractional Anisotropy from the nearby region is quite different between two measurements. This might be because the affected region is larger than had been identified in the DWI images. Because the two scans of the patient are separated by 17 weeks, the difference of the Fractional Anisotropy in the

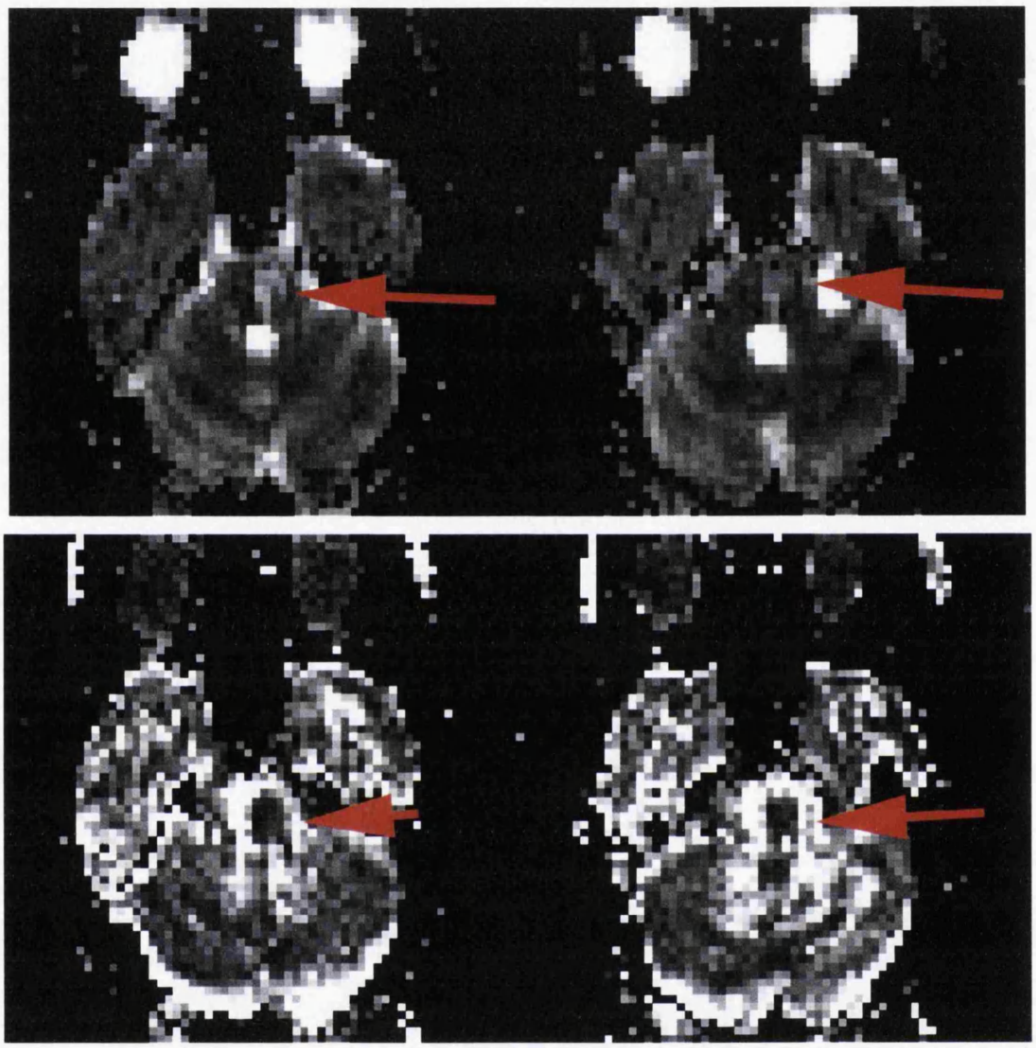

Figure 3.6: The figure shows images, at two similar positions, of the calculated trace/3 and Fractional Anisotropy from the stroke patient 4 weeks after the onset of the insult in the left of the Pons. Arrows show the suspected site of the infarct.

Top: Trace/3

Bottom: Fractional Anisotropy

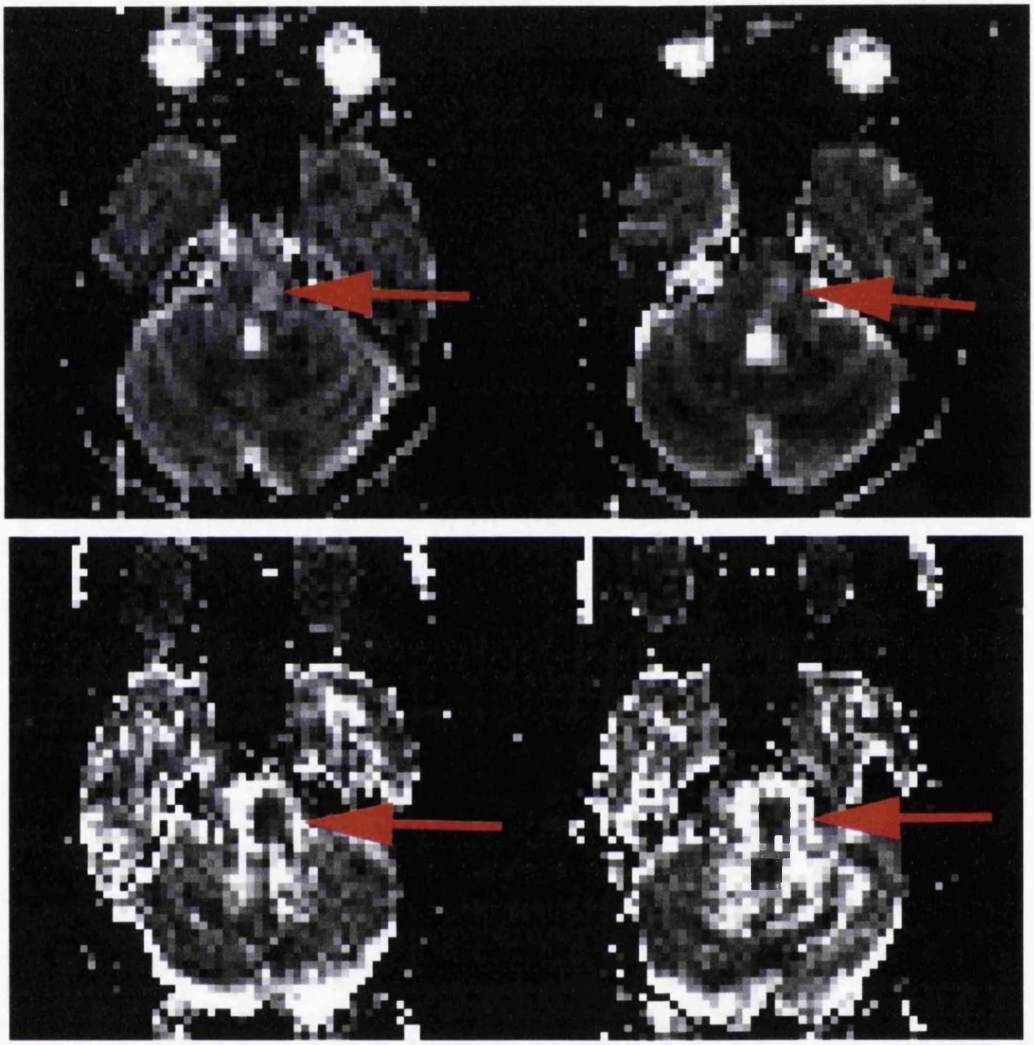

Figure 3.7: The figure shows images, at two similar positions, of the calculated trace/3 and Fractional Anisotropy from the same patient after 21 weeks of the insult. The trace/3 and Fractional Anisotropy still shows differences from the nearby healthy tissue. Arrows show the suspected site of the infarct.

Top: Trace/3

Bottom: Fractional Anisotropy

normal tissues might also be due to variations in the choice of ROIs. It is difficult to predict to what extent the region of insult can recover to its full function. A chronological study is required for further investigation on the stroke recovery mechanism.

However, the coarse spatial resolution from the single shot DT-EPI sequences as seen in the above images makes the clinical interpretation rather limited. For the patient studied here, the lesion volume is about $1000mm^3$. The spatial resolution in the single shot DT-EPI experiment corresponds to voxels of 27 mm^3, and hence the images are affected by partial volume effects. For further exploration of development during the recovery period, images with a finer spatial resolution are desirable. This leads to the main part of the project: Towards a Higher Spatial Resolution Diffusion Tensor Imaging.

Chapter 4

Diffusion Tensor EPI with High Spatial Resolution

Signal-to-Noise Ratio and spatial resolution in MRI are compromised. Because of the signal attenuation by the prolonged diffusion weighting gradient, the spatial resolution of a standard single shot EPI acquisition in a 1.5 Tesla clinical scanner is typically limited to voxels of approximately 3 mm by 3 mm by 3 mm in volume.

To obtain higher spatial resolution more extensive sampling in k-space is required, which leads to prolonged acquisition time. As TE increases, image blurring and distortions become more pronounced in several brain regions, due to the spin-spin relaxation . Thus, at 1.5 Tesla, the acquisition time per image should ideally be less than 100 msec in humans. However, most standard clinical scanners do not allow for the collection of sufficient k-space data during this time. The problem gets even worse with the introduction of long duration diffusion weighting gradients, which further extend TE and attenuate the signal.

Existing EPI techniques have been explored to meet the requirement of measuring the diffusion tensor with high spatial resolution and good SNR. This includes an interleaved EPI sequence (McKinnon, 1993; Slavin *et al.*, 1995; Kim *et al.*, 1996) and a single shot

EPI sequence with Half Fourier Acquisition method (HF-EPI) (Rzedzian, 1988; Jesmanowicz *et al.*, 1997).

4.1 Development of 2D Interleaved EPI

In a 2D interleaved EPI sequence, the data required for the reconstruction of one image are collected from two separate excitations. It is later spliced together during image reconstruction.

The sequence consists of 2 segments. It acquires sequentially the data in k-space in an interleaved order. Each segment consists of 64 phase encoding steps and is similar to a standard 2D multi-slice EPI experiment, with the acquisition of alternate lines in k-space. For every line, 128 points are sampled within the same acquisition time per echo as in the single shot EPI sequence. This results in a matrix size of 128 by 128. With the same field of view and half the slice thickness, this will yield a voxel size of 1/8 of the single shot EPI sequence.

Echo time shifting is added to improve the ghosting due to phase discontinuities (Feinberg & Oshio, 1991; McKinnon, 1993). It is a small time delay which is added in between the excitation pulse and the acquisition of the data of the second segment so that the phase evolution will vary continuously instead of in a step-wise manner.

After the acquisition, one-dimensional Fourier Transformation is performed along the readout direction and the data is phase corrected separately in each segment using the information in the navigator echoes as described in Section 2.3.2 in Chapter 2. Afterwards data from two segments are spliced together in k-space in the correct order and the final image is reconstructed with a second Fourier Transformation along the phase encoding direction. Figure 4.1 shows the acquisition order in k-space. Nine images reconstructed from a healthy volunteer are shown in Figure 4.2.

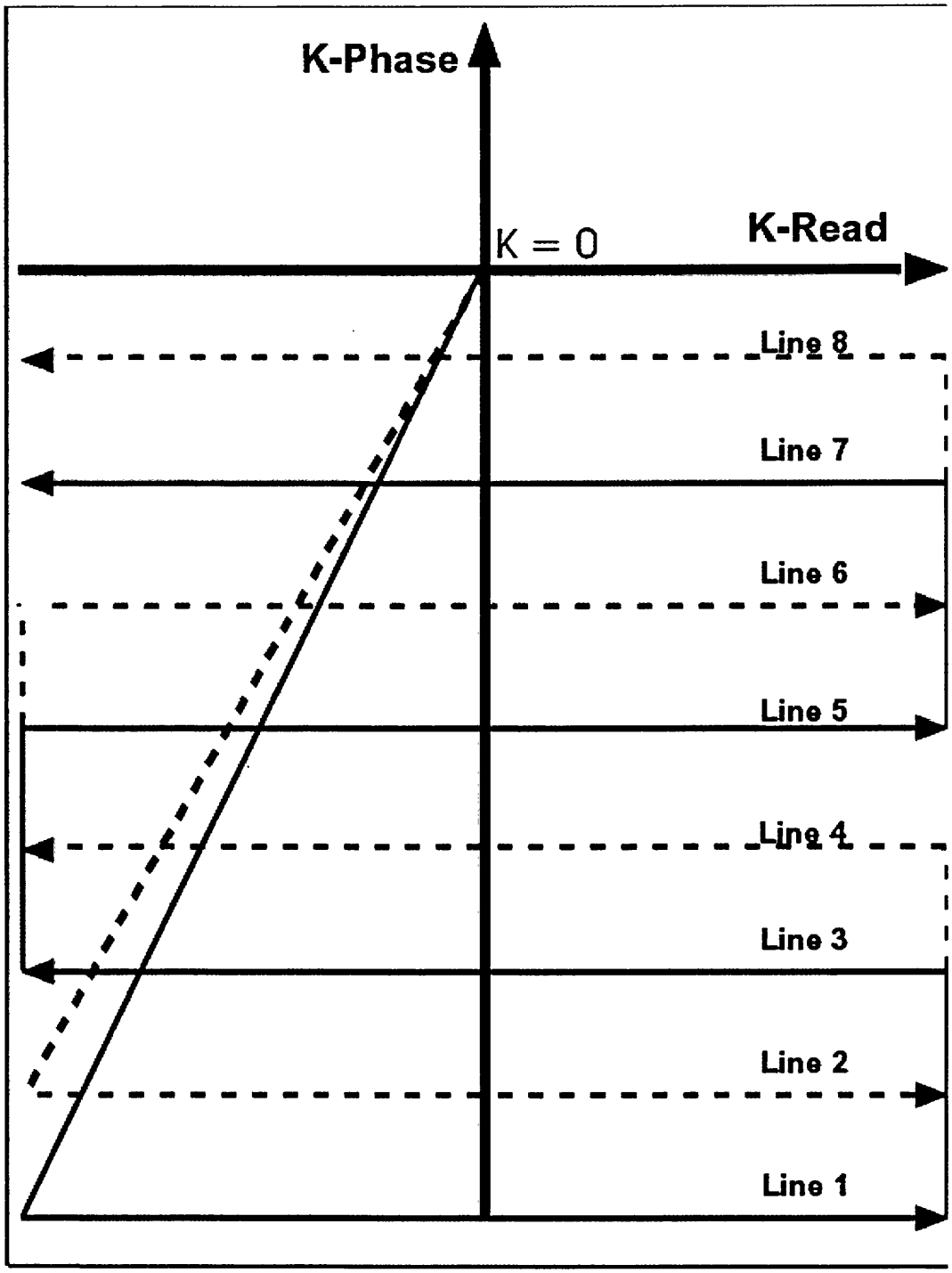

Figure 4.1: The figure shows the acquisition order in k-space of the 2D interleaved EPI sequence of two segments. The solid lines show the acquisition from the first segment and the dashed lines shows the second segment. The arrow points to the direction of acquisition for each individual k-space line.

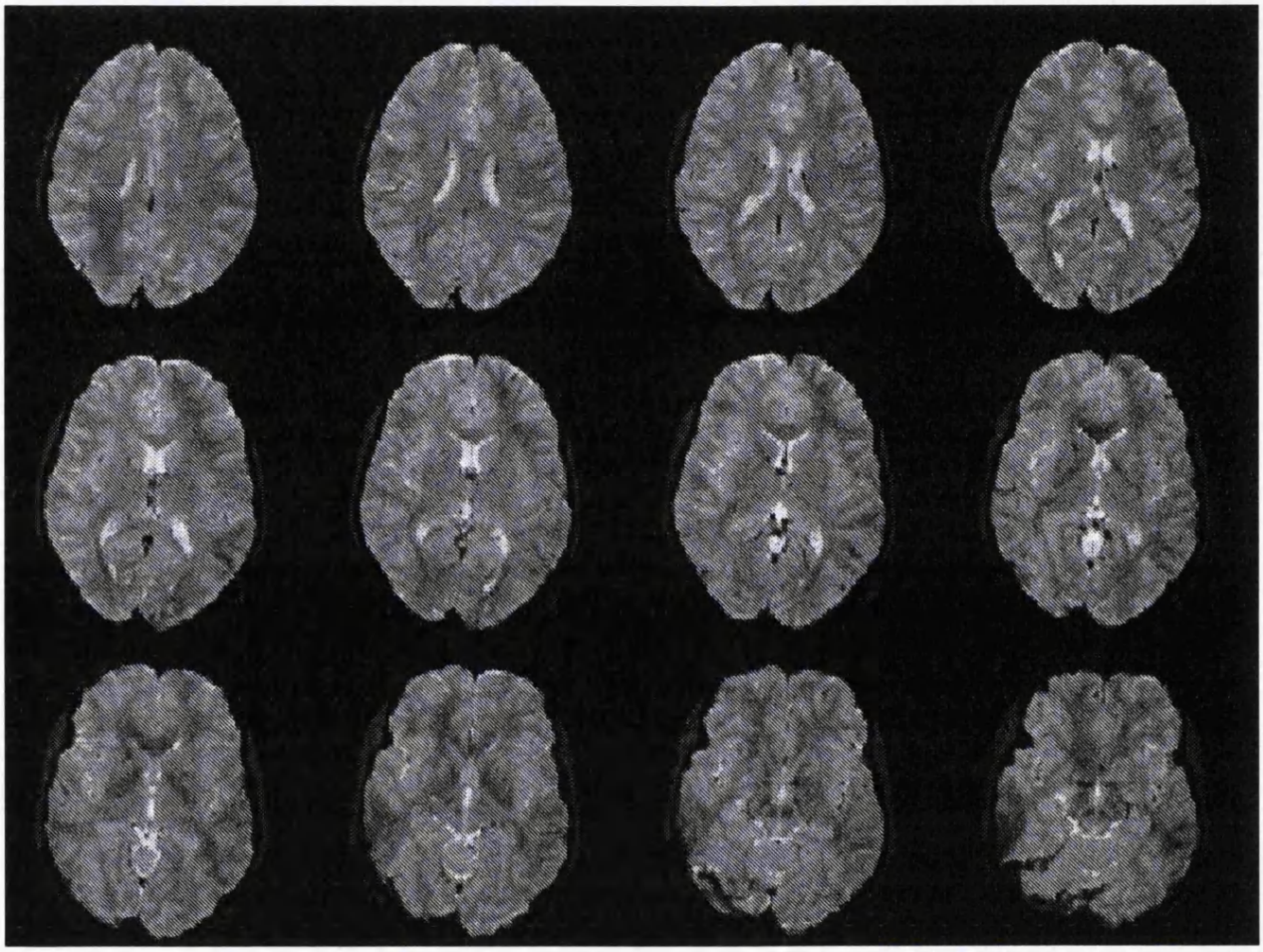

Figure 4.2: The figure shows 9 slices of the brain images acquired by the 2D interleaved EPI sequence of two segments. The voxel size is $(1.5mm)^3$

4.2 Development of EPI Sequences with Half Fourier Acquisition

From the definition of k-space, the signal in k-space s(k) is a Fourier Transformation of the spin density function $\rho(x, y, z)$ as in 4.1.

$$s(k) = \int_{-\infty}^{\infty}\int_{-\infty}^{\infty}\int_{-\infty}^{\infty}\rho(x,y,z)e^{-ikx}e^{-iky}e^{-ikz}dxdydz \tag{4.1}$$

The spin density function is a real function in which $\rho(x, y, z) = \rho^*(x, y, z)$. From Equation 4.1, the real part of the k-space signal function is symmetric such that $\Re[s(k)] = \Re[s(-k)]$ and the imaginary part is anti-symmetric such that $\Im[s(k)] = -\Im[s(-k)]$. The property of symmetry in k-space allows the development of the Half Fourier acquisition method, in which only half of the data in k-space is acquired while the other half is generated by assuming conjugate symmetry.

The HF-EPI sequence is made of two modules. The preparation part is the same as a standard 2D multi-slice Spin Echo EPI sequence. In the data acquisition part, 128 points are acquired for one echo. 53 echoes are acquired from half of k-space with another 8 echoes from the other half of k-space. The extra information from the additional 8 echoes helps to merge the two parts of k-space acquired and interpolated with the Half Fourier technique, into a continuous data set. Otherwise truncation artefacts will occur due to k-space discontinuity. The second half of k-space is interpolated from the data in the first half of k-space by Equation 4.2. After interpolation, this leads to 106 echoes in total for image reconstruction. The effective voxel volume is thus larger than obtained in the 2D interleaved EPI sequence ($(1.5mm)^3$).

$$\hat{s}(k) = \begin{cases} s_m(k) & if\ k \geq 0 \\ (s_m(-k))^* & if\ k < 0 \end{cases} \tag{4.2}$$

After the reconstruction of the complete k-space data, the image was calculated in the

same manner as the standard 2D multi-slice EPI sequence. The final images are shown in Figure 4.3.

The images of the brain reconstructed from the HF-EPI sequence as in Figure 4.3 are relatively ghost free. But, because the data is interpolated rather than acquired, the error tends to accumulate towards the edge of k-space which contains the high frequency components of the image. The final image tends to suffer from distortion and blurring. There is also a more severe Gibb's ringing artefact after the implementation of diffusion weighting gradients. The effective voxel size is 1.5 mm by 1.8 mm by 1.5 mm. This is because the actual number of phase encoding steps is less than 128. The major reservation about the use of the HF-EPI sequence is the intrinsic low SNR shown in the figure, which will be discussed later in Section 4.4.3.

Technical Considerations Regarding Higher Resolution Diffusion Tensor Imaging

The measured diffusion tensor is often affected by the low SNR inherent in diffusion weighted imaging techniques and ghosts from various sources. In this section I am going to present some of the major difficulties which prevent DTI from being used in general clinical applications, namely ghosting and low SNR, and propose a feasible solution.

4.3 Ghost in EPI and Its Correction

Ghosting artefacts in diffusion weighted EPI come from various sources and for various reasons. In the 2D interleaved EPI sequence, ghosts arises from mismatch of phase in k-space. Because the spatial position of spins in MRI is encoded in the resonant frequency

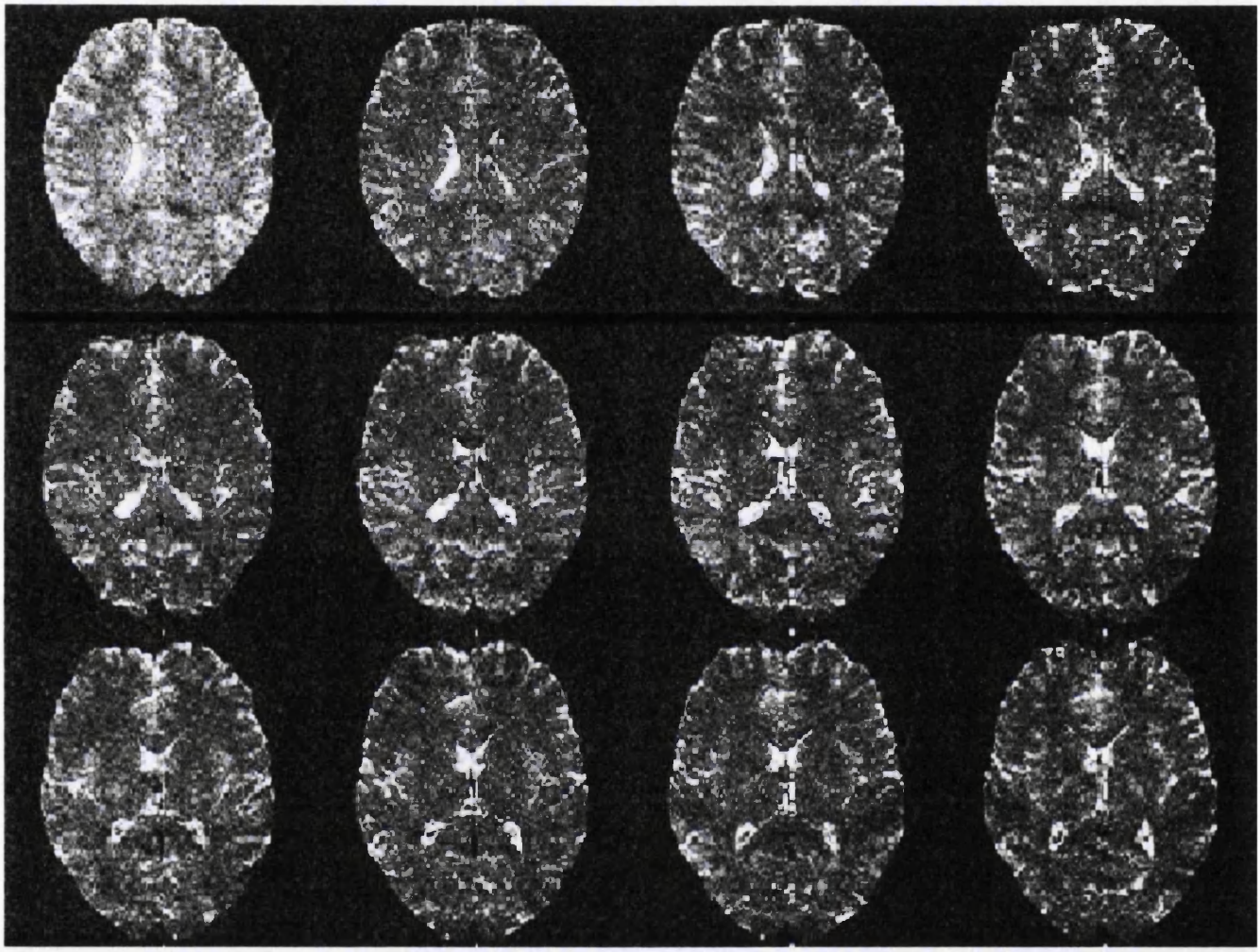

Figure 4.3: The figure shows 9 slices of images from a healthy volunteer acquired with the HF-EPI sequence. The effective voxel size is 1.5 mm by 1.81 mm by 1.5 mm.

of precession, after image reconstruction, phase difference in k-space is generally misinterpreted as difference in spatial locations and thus mis-labeled as signal from different voxels. It reveals itself as ghosts in the reconstructed image. In the following section I am going to allocate the source of error leading to the ghost, by the position of the ghost in the image, and concentrate on the ghosts induced by motion and eddy currents.

4.3.1 Location of the Ghost

Motion related artefacts can be generally corrected or minimised in the single shot EPI sequence. However, it is relatively difficult to match data from several separate excitations obtained in different motion conditions into one complete k-space data set in multi-shot EPI sequences. Any mismatch between the segments or between odd and even lines within the same segment will lead to ghosting in the final image. It is thus essential to identify the source of the ghost before any correction can be properly made. A simulation to identify the source of the Nyquist ghost is presented here.
A phantom image was created as shown in Figure 4.4. The image has a matrix of 128 by 128. The centre line of the phantom image is set to 1, everywhere else being 0. After image reconstruction, one slice profile was shown to the right of Figure 4.4.

If a 10 degree phase shift is introduced between two excitations, a ghost will be introduced in a displaced position at half the FOV. The intensity is 8.7 % of the signal of the object. The left image of Figure 4.5 shows a profile of the slice. An amplitude difference of 30 % between two segments also introduces a ghost in a position at half the FOV. The intensity of the ghost is 13 % of the object as shown in the right of Figure 4.5.

If the phase variation is within each segment, after the image reconstruction, the ghost will appear in a position at quarter of FOV. In Figure 4.6, a 20 degree phase difference

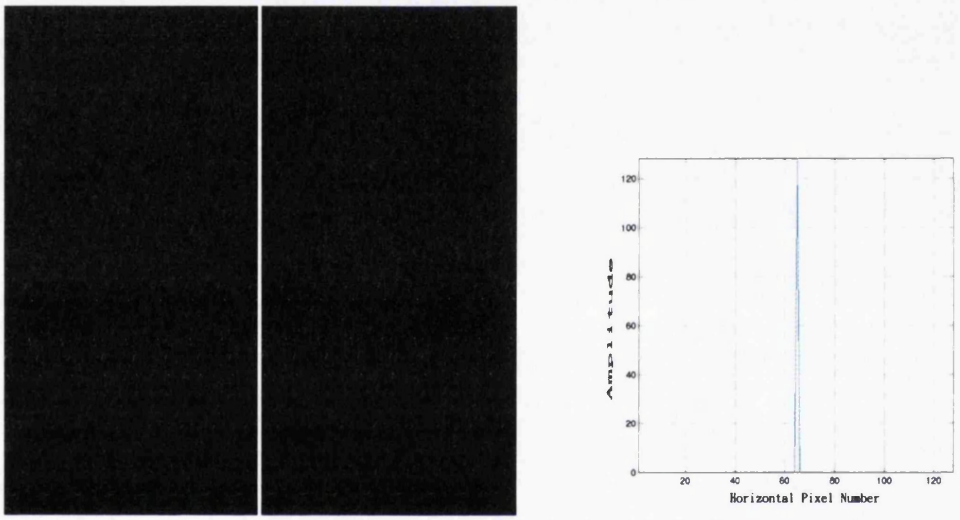

Figure 4.4: The figure shows the simulated phantom made of a matrix of 128 by 128 points. The left figure is the image of the phantom. The right figure is one slice profile which shows the position of non-zero signal intensity.

Left: Image of the Phantom created.

Right: The profile shows the position of non-zero signal intensity.

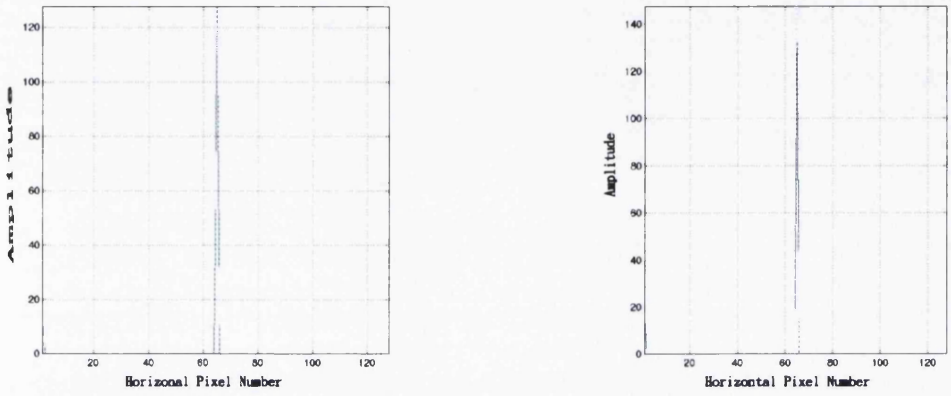

Figure 4.5: The figures show that any differences in phase or amplitude between two segments can lead to ghosting artefact occurring shifted by half of field of view.
Left: 10 degrees of phase mismatch between two segments is introduced. The ghost can be seen in a position shifted by half of the FOV.(Arrow)
Right: A 30 % amplitude difference was introduced. The ghost appears in the same position as in the left image.(Arrow)

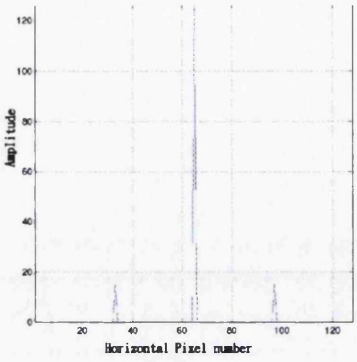

Figure 4.6: The figures show that phase variations between the odd and even lines in an interleaved EPI sequence of 2 segments can lead to ghosting artefact at the position of quarter of field of view after the data were spliced in the correct order in k-space.

was introduced between the odd and even lines within the same segments. After the image reconstruction, two ghosts appear in the position of a quarter of FOV. The intensity of the ghost is approximate 12 % of the object. It is quite unlikely that there is a big interruption in the amplitude within the same segment during EPI acquisition.

If different amounts of phase variations were introduced during the acquisitions, ghosts will appear at corresponding positions. Here 5 degree phase shift was introduced within the first segments, and 10 degree within the second segment. A 10 degree phase shift was introduced between the segments. Figure 4.7 left shows a profile of the final image. Ghosts appear at the position of half and quarter of FOV. The intensity of the ghost at half FOV is 9.9 % of the signal in the object. The intensity of the ghost at the first quarter of FOV is 21.9 % and at the third quarter of FOV is 23.5 %. If an additional amplitude difference of 30 % was introduced, the location of the ghost will not change but the intensities relative to the object become 19.7 % at half of FOV, 19.1 % at the first quarter of FOV and 20.3 % at the third quarter.

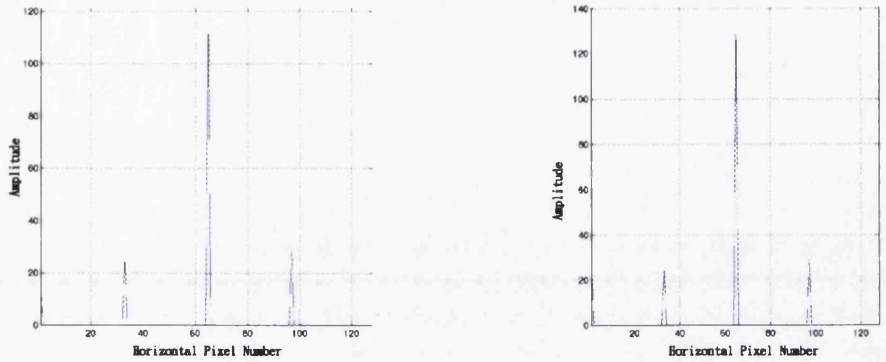

Figure 4.7: The figure shows that different sources of errors in k-space lead to ghosts at distinct parts of the field of view after properly splicing the data in the correct k-space order.

Left: 10 degrees of phase mismatch between segments, 5 degrees error within the first segment and 10 degrees error within the second segment.

Right: In addition to phase variations, a 30 percent amplitude mismatch between segments was introduced.

In interleaved EPI, data are reorganized in k-space as shown in Figure 4.1. Errors may be due to a phase mismatch between the two segments or a phase mismatch between even and odd lines within a segment. In the first case, the phase variation has a period of two lines in k-space. After Fourier Transformation, this results in a Nyquist ghost which is shifted by 50 % of the FOV. In the latter case, the phase variation has a period of four lines which results in a ghost shifted by 25 % of the FOV after Fourier Transformation.

4.3.2 Sources of the Ghost

Any imperfection, from system hardware during acquisition, to the image reconstruction during post processing, will reveal itself as artefacts and ghosts in the final image. Here we have only concentrated on those which are more problematic to DTI; that is ghosts due to eddy currents and motion.

Eddy Current Induced Ghost

Standard diffusion measurements typically use a Spin Echo type sequence in combination with two balanced unipolar pulsed diffusion weighting gradients. Unfortunately, such a sequence is easily affected by artefacts arising from eddy currents induced by the long and powerful diffusion weighting gradients.
Eddy currents may be induced in conductive material throughout the MR system. The rapidly changed switching gradient may lead to rapid changes of flux in the RF coil, shield, main magnet and even the subject being imaged. This induced electrical field $\vec{E}$ can be expressed by the following equation:

$$\int \vec{E} d\vec{l} = -\frac{\partial \phi}{\partial t} = \int_{area} \frac{\partial \vec{B}}{\partial t} \cdot d\vec{A} \tag{4.3}$$

The majority of the eddy current appears in the RF coil or in the shielding that surrounds the main magnet. It is clear from Equation 4.3 that the induced current opposes the gradient field which creates it. This will lead to a distortion in the imaging gradient and a time delay between the voltage being applied and the gradient becoming established. The resulting images will look distorted because of the phase errors induced by the eddy current. Eddy currents due to gradients applied in different directions can lead to different types of artefact. The effect of eddy current in the frequency encoding direction is a shearing of the image because the pixels in the image will be shifted in the phase encoding direction proportionally to its position in the frequency encoding direc-

tion. The effect of eddy current in the phase encoding direction is mainly a stretching or shrinking of the image. The B_0 eddy current will lead to a bulk shift of the image in the phase encoding direction. Distortion in the individual diffusion weighted image will in turn lead to mis-registration in the calculated ADC maps, thus an inaccurate estimation of the diffusion parameters.(Jezzard *et al.*, 1998)

Unfortunately, although artefacts caused by eddy currents are usually reproducible, they are normally difficult to predict or measure and often require complicated phase correction. Hasselgrove and Moore proposed a cross-correlation of the diffusion image data with a template image (Hasselgrove & Moore, 1996), which is computationally demanding. Jezzard et al (Jezzard *et al.*, 1998) used an extra set of navigator echoes in both the frequency and phase encoding directions in an interleaved EPI sequence, with the penalty of increased scanning time. A robust phase unwrapping algorithm was used by Jezzard et al to fit both the navigator echoes and the eddy current interleaved echoes.

In diffusion weighted EPI, eddy currents are often induced during the ramping period of the strong and long-duration diffusion weighting gradient. Conventionally, an additional time delay is inserted after the ramping down of the diffusion weighting gradient. To avoid eddy current artefacts, instead of the standard Spin Echo EPI experiment with a single 180 degree RF pulse, two 180 degree RF pulses can be used (Feinberg & Jakab, 1990; Heid, 2000). Two pairs of diffusion weighting gradients of opposite signs, separated by the 180 degree RF pulses, are applied between the 90 degree RF pulse and data acquisition. However, the echo time TE will be further extended because of the additional diffusion weighting gradients used. Figure 4.8 shows the gradient pulses activity of such a sequence.

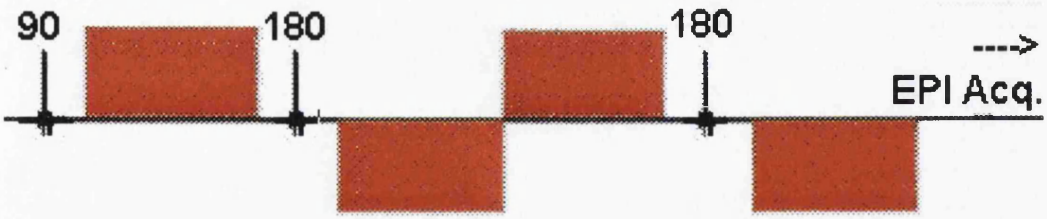

Figure 4.8: The figure shows the gradient activity and pulse diagram of the EPI sequence with two 180 degree RF pulses and two pairs of diffusion weighting gradients with opposite signs, which were displayed in the red shaded area. Such a diffusion encoding scheme produces a satisfactory eddy current compensation.

Motion Induced Ghost

In multi-shot techniques, it is necessary to combine the data from different acquisitions to form the final image. The phase variation between separate excitations often leads to ghosting artefacts as discussed in Section 4.3.1. In a biological environment, one of the major sources of such phase variation is motion.

The diffusion coefficient is a measurement of thermal motion at the molecular level. The effects of diffusion are very easily obscured by the bulk head movement or other biological motion. Pulsatile motion during the cardiac cycle introduces serious motion artefacts in many diffusion weighted imaging techniques. Cardiac triggering is a generally adopted approach to minimise the pulsatile input during systole. However, this can seriously affect the temporal resolution.

If the motion is only translational, the ghost level normally can be improved by phase information extracted from the navigator echoes collected immediately before the EPI data acquisition (Ordidge *et al.*, 1994; Dietrich *et al.*, 2000). For rotational movement, the data needs to be re-acquired. In Chapter 5 new post processing algorithms are described which do not require cardiac triggering. The corrupted data are discarded through a thresholding procedure. This strategy will, therefore, increase the speed of

acquisition.

4.3.3 Three Navigator Echoes Correction

For the EPI sequences supplied on the Siemens Vision scanner which was used as a template for development, two navigator echoes are acquired immediately before the data acquisition (Ordidge *et al.*, 1994). Unfortunately information extracted from such navigator echoes will re-introduce the off-resonance artefact caused by the fact that the acquisitions of the echoes are at different times. Any local off-resonance effect causes a phase difference between the navigator echoes. Here, three navigator echoes are acquired instead of the more usual two echoes (Heid, 1997). The first and third navigator echoes, S_1^+ and S_3^+, acquired at e.g. the positive lines in k-space, are averaged to produce a composite reference echo, S_2^+, which has a mean echo time similar to that of the second echo, S_2^-, acquired at a negative k-space line.

Assuming the $T2^*$ decay time is larger than the difference in echo times, the signal from the composite reference echo will be as in the Equation 4.4:

$$S_2^+ = \frac{TE_3 - TE_2}{TE_3 - TE_1} S_1^+ + \frac{TE_2 - TE_1}{TE_3 - TE_1} S_3^+ \tag{4.4}$$

Because $TE_3 - TE_2 = TE_2 - TE_1$, Equation 4.4 can be simplified as Equation 4.5:

$$S_2^+ = \frac{S_1^+ + S_3^+}{2} \tag{4.5}$$

After the acquisition of the complete k-space information for all slices, a pixel by pixel phase correction of the raw data was performed based on the phase information extracted from navigator echoes mentioned above.

Figure 4.9 shows the efficacy of phase correction by the three navigator echoes. The left image is reconstructed in the standard way with phase information extracted from two navigator echoes. To the right is the same slice but reconstructed from phase correction

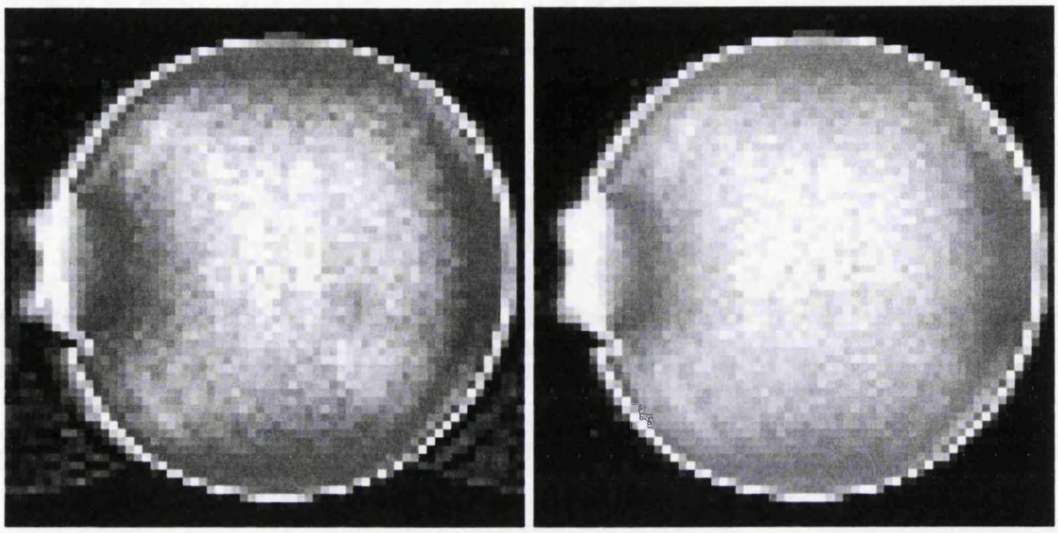

Figure 4.9: The figure shows the efficacy of the phase correction with information extracted from the three navigator echoes, compared with image reconstructed from phase information extracted from two echoes.
Left: Image with two navigator echoes phase correction.
Right: Image with three navigator echoes phase correction.

with three navigator echoes. There is a clear improvement in the intensity of the ghost at the half of field of view in the right image.

4.4 Signal-to-Noise Ratio

4.4.1 Definition of SNR

Signal-to-Noise Ratio is a very important imaging factor. The MR signal has to be reasonably higher than the noise level so that the object of interest in the image can be recognised.
In MRI, the signal mainly comes from the net magnetization available within the voxel

of interest. If the proton density function for a voxel at a point x, y, z, and of size dx, dy and dz is $\rho(x, y, z)$, the signal $\vec{s}(k_x, k_y, k_z)$ can be expressed as in Equation 4.6 (Haacke *et al.*, 1999; D.Stark & Bradley, 1992)

$$\vec{s}(k_x, k_y, k_z) = \int\int\int dxdydz\rho(x, y, z)e^{-i(k_x x + k_y y + k_z z)} \tag{4.6}$$

Naturally the larger the voxel, the more protons it contains and thus the better the SNR. In a homogeneous sample, the signal normally depends on the imaging parameters such as repetition time TR, echo time TE, the size of the voxel, sampling bandwidth, and the history of the magnetization within the voxel and so on. In this section, the temperature and relaxation time of the sample are not considered.

With shorter TR, for example in 3D phase encoded EPI, the magnetization is excited before full T_1 relaxation of spins, therefore less magnetic moment will be available for the next acquisition, which results in less signal. The transverse magnetization available within the volume of the voxel determines the final signal presented in the voxel. With longer TE, signal will be decreased extensively by T_2 relaxation. Thus the SNR will be smaller.

The random noise in MRI mainly comes from thermal effects. In an optimised experiment, the noise from digitisation error can be neglected and only the fluctuation in the coils, electronics and the sample itself will contribute to the majority of the thermal noise. In a well-designed high field system, the thermal noise due to the coil and pre-amplifier circuit should be minimal. The noise is typically assumed to be Gaussian distributed with a zero mean and variance of σ^2.

However, what is of main concern in the final image is not the absolute level of signal and noise but the ratio of the signal to the noise. Unfortunately some parameters which affect the SNR are not measurable. Here we will skip the detail of derivation and only present the expression as in Equation 4.7.

Considering a voxel at position $\vec{r}$ of volume dV, with the number of multiplexes in the readout, phase encoding and slice selection direction of N_x, N_y, N_z respectively, the sampling bandwidth is BW_x and N_{avg} is the number of averages, the SNR in the final image will be (Haacke *et al.*, 1999)

$$SNR \propto Q \cdot \mid M_T(\vec{r}) \mid \cdot dV(\vec{r}) \cdot \sqrt{N_x N_y N_z N_{avg}} \cdot \frac{1}{\sqrt{BW_x}} \tag{4.7}$$

where Q is a proportional coefficient describing the quality factor of the coil.
From the above description we can see when a specific spatial resolution is desired from a sequence, the most common practice to increase SNR is by multiple averaging. Decreasing the sampling bandwidth will increase the SNR. Yet, this also increases the sampling time per echo, which results in a longer image acquisition time and worse T_2/T_2^* decay. Alternatively, to achieve a satisfactory SNR, it is necessary to use a large voxel size. For an isotropic voxel, the resolution in the single shot EPI sequence is generally larger than $(3mm)^3$, which will unavoidably worsen the partial volume artefact. If it is necessary to increase the in-plane resolution, frequently it is achieved by using a relatively thick slice to compensate for the loss of SNR in the transverse directions. This will lead to anisotropic voxels and potential bias in the measurement of the diffusion tensor.
In this project, the measurement of SNR was conducted by measuring the mean signal from an ROI within the subject of interest and dividing by the standard deviation from an ROI in the background where there is no artefact.

4.4.2 Effects of Low SNR

Images of low SNR are difficult to interpret. In diffusion tensor imaging where quantitative data is required, images of low SNR will lead to error in the calculation of important parameters (Pierpaoli & Basser, 1996).
The accuracy of the diffusion measurement depends on the SNR. As the SNR decreases,

the diffusion coefficient tends to be underestimated. This is because the diffusion coefficient is usually calculated from the exponential decrease of the signal attenuation between one low or non-diffusion weighted image, and a highly diffusion weighted image. With noise present in the measurement, the curve of signal attenuation will not decay to zero baseline but instead, to the noise level above zero. This can be mis-interpreted as a slower decay and thus a smaller diffusion coefficient.

The noise level will lead to deviations in the size and direction of the eigenvalues and eigenvectors. The deviation in the size of eigenvalues will cause errors in the sorting of the eigenvalues, which leads to errors in the estimation of diffusion anisotropy. Noise will also change the direction of eigenvectors. The low SNR can thus lead to mistakes in most techniques of white matter fiber tracking based on following the principal eigenvector.

In Table 4.1, the trace/3, the sorted eigenvalues and Fractional Anisotropy are calculated from the water phantom with the single shot DT-EPI sequences. Clearly at low SNR, the largest eigenvalue tends to be over-estimated and the smallest eigenvalue underestimated. The second eigenvalue is less affected by low SNR. The absolute value of trace/3, which results from the sum of the eigenvalues, is relatively stable across the whole range of SNR. However, the standard deviation of the trace and eigenvalue measurements increase as the SNR decreases, which is shown in the left graph of Figure 4.10. The errors in the calculated eigenvalues will change the accuracy of diffusion anisotropy indexes. The result is close to the observation from Pierpaoli et al (Pierpaoli & Basser, 1996). Yet, even for those which do not rely on the sorting order of eigenvalues, as SNR decreases, the estimated anisotropy still increases, as shown in the right graph of Figure 4.10. When SNR decreases to 23.65, the calculated Fractional Anisotropy increases to 0.11 for isotropic water, compared with 0.08 when SNR is 91.

Figure 4.11 and Figure 4.12 show the effect of SNR on the calculated trace and Fractional Anisotropy in the images of a slice of human brain. Trace images usually did not display much contrast between white matter and gray matter in the brain and are less affected by low SNR. Yet in the figures as SNR increases, the subtle detail of the brain is better

Number of Averages	1	4	9	15
SNR	23.65	53.17	68.15	91.44
First eigenvalue	2.23	2.20	2.20	2.20
Second eigenvalue	2.01	1.99	1.99	1.99
Third eigenvalue	1.86	1.90	1.90	1.90
Trace/3	2.03	2.03	2.03	2.03
FA	0.11	0.09	0.08	0.08

Table 4.1: The table shows the effect of SNR on the measurement of diffusion properties. The values are given in unit of $10^{-9}m^2/sec$. Fractional Anisotropy is dimensionless.

defined in the trace, as can be seen in the edge of the ventricles and the structure of the cortex.

With a single average, the Fractional Anisotropy map does not show clear contrast between the relatively isotropic CSF in the ventricle and the nearby anisotropic Corpus Callosum in the white matter. As the SNR improves with the increased number of averages, the contrast between various tissues in the brain becomes better defined in the Fractional Anisotropy map of Figure 4.12.

To maintain an acceptable SNR in DTI, most of the measurements are limited to relatively low spatial resolution. The results from the dataset of low resolution are often hard to interpret and subject to partial volume artefacts. This makes a sequence of high spatial resolution and high SNR very desirable. In the following section, there will be further investigation of the SNR of the sequences developed during the project.

4.4.3 Comparison of SNRs from Various Sequences

Assume the SNR of the image measured with a standard 2D single shot EPI sequence is 1. The voxel size is 3 mm by 3 mm by 3mm and the matrix size is 64 by 64. The effect

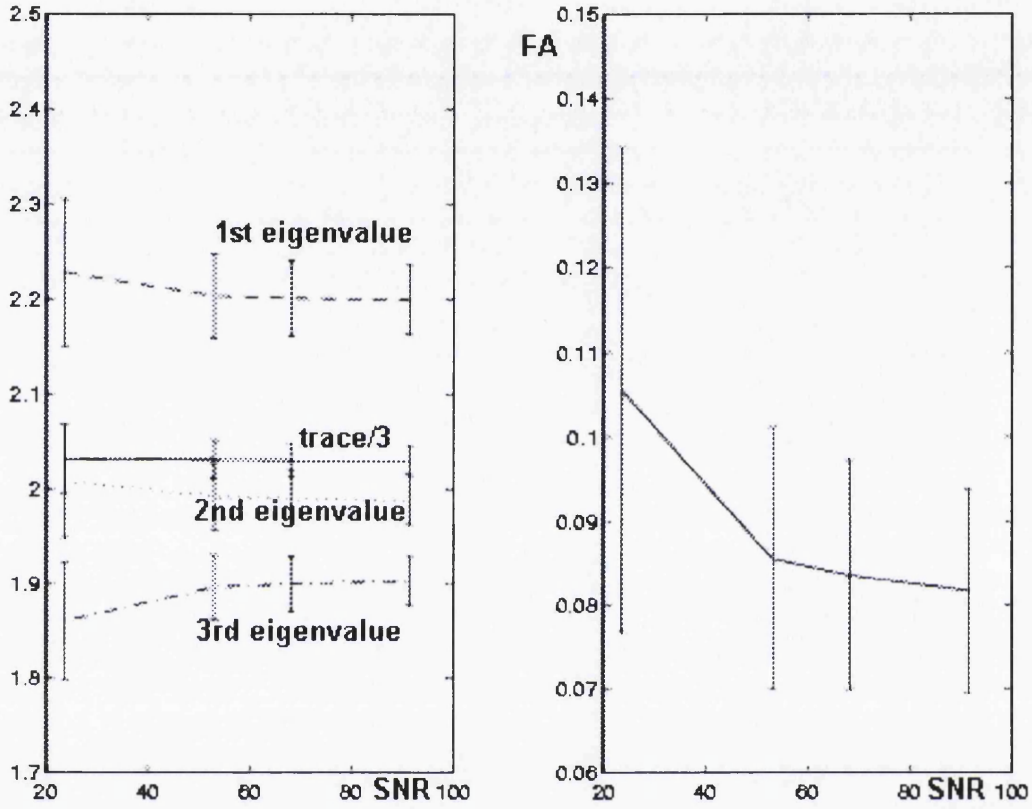

Figure 4.10: The figure shows the effect of SNR on the calculation of eigenvalues and Fractional Anisotropy of a water phantom.

Left: Trace/3 and sorted eigenvalues relative to SNR. The values are given in units of $10^{-9}m^2/sec$

Right: Calculated Fractional Anisotropy relative to the SNR.

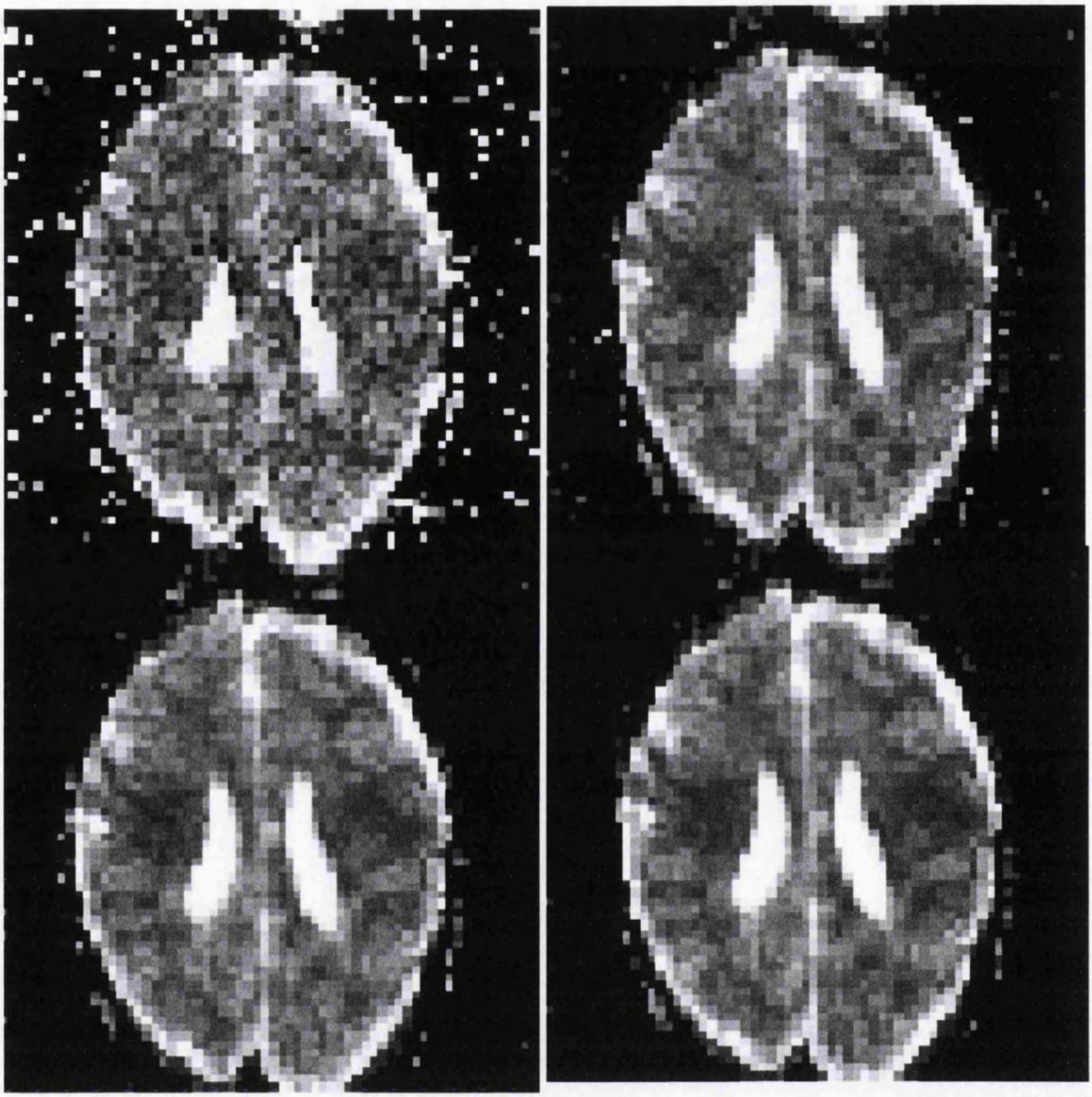

Figure 4.11: The figure shows the effect of SNR on the calculation of the diffusion trace in human.

Top Left: Trace image measured with the 2D single shot DT-EPI sequences with single average.

Top Right: Trace image with 4 averages.

Bottom Left: Trace image with 9 averages.

Bottom Right: Trace image with 15 averages.

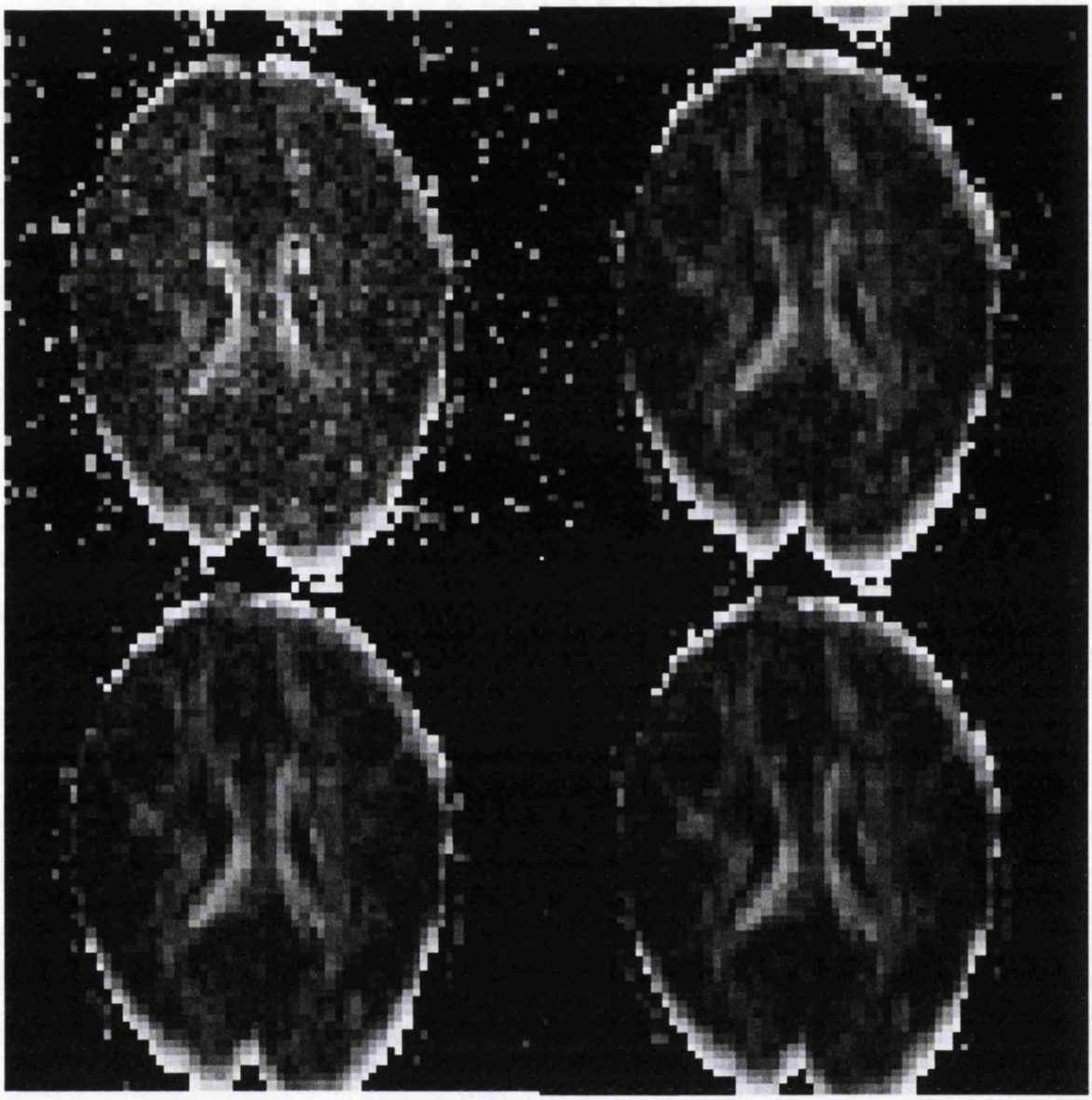

Figure 4.12: The figure shows the effect of SNR on the calculation of Fractional Anisotropy.

Top Left: Fractional Anisotropy measured with the 2D single shot DT-EPI sequences with single average.

Top Right: Fractional Anisotropy image with 4 averages.

Bottom Left: Fractional Anisotropy image with 9 averages.

Bottom Right: Fractional Anisotropy image with 15 averages.

of relaxation is ignored because the sequences for comparison are designed to have the same echo time TE, and images from the first measurement alone are used.

SNR in the HF-EPI Sequence

In the sequence of HF-EPI as developed in Section 4.2, the effective voxel size of interest $dx \cdot dy \cdot dz$ for a FOV of 192 mm is 1.5 mm by 1.81 mm by 1.5 mm. The size of the matrix at acquisition was 128 by 64 and was interpolated to 128 by 106 after post processing. To keep the echo time TE constant, the sampling bandwidth in the frequency encoding direction was doubled. 128 points were sampled for each echo during the same acquisition time per echo as for the 2D single shot EPI sequence.
With double N_x and BW_x, the SNR in images acquired by the HF-EPI sequence will be as $SNR_{HF-EPI} = SNR_{2D} \cdot (\frac{1.81}{3}) \cdot (\frac{1.5}{3}) \cdot (\frac{1.5}{3}) \cdot \sqrt{\frac{128}{64}} \cdot \frac{1}{\sqrt{2}}$, which is only 15.08 % of the SNR measured with the 2D single shot EPI sequence.
The acquisition time for one individual slice remains the same as in the case of the 2D single shot EPI sequence. Yet to cover the same range in the brain with slices of half the thickness, it is necessary to double the number of slices, which will double the total scanning time.
Therefore, compared with the SNR of the images from the 2D single shot EPI sequence, the image measured with the HF-EPI sequence has almost double the spatial resolution, with a loss of SNR and twice the scanning time for the same coverage.

SNR in the Interleaved EPI Sequence with Two Segments

In the interleaved EPI sequence with two segments, the size of voxel of interest $dx \cdot dy \cdot dz$ reduces to half in each direction. 128 points were sampled for each echo in the same acquisition time as in the 2D single shot EPI sequence. The bandwidth was thus doubled. Sixty-four phase encoding steps were repeated in each segment. The matrix size is 128 by 128.

The SNR of the images acquired by the 2D interleaved EPI sequence will be $SNR_{interleaved} = SNR_{2D} \cdot (\frac{1.5}{3})^3 \cdot \sqrt{\frac{128}{64}} \cdot \sqrt{\frac{128}{64}} \cdot \frac{1}{\sqrt{2}}$, which will be $\frac{\sqrt{2}}{8}$.
Because the sequence consists of two segments, each of which is similar to a single shot EPI acquisition, the acquisition time for one slice will be twice the time of that of the 2D single shot EPI sequence. To cover the same range of the brain with half the slice thickness, it is necessary to acquire twice the number of slices. Compared with the 2D single shot EPI sequence, the advantage in spatial resolution is acquired with a reduction of SNR to 17.67 % of its normal value and four times the total scanning time.

Conclusion for Comparison

The result can be summed up in Table 4.2. The 2D single shot EPI sequence provides better SNR per unit time. Yet the spatial resolution of 3mm is poorer than desirable. For high spatial resolution with isotropic voxel size of 1.5 mm and the matrix size of 128 by 128, the acquisition time with one single excitation will be much too long, so that T_2 relaxation eliminates most of the signal by the end of the acquisition. This will also lead to image distortion and blurring. The situation is even worse after adding in long duration diffusion weighting gradients, which further extends the acquisition and attenuates the signal.
For images of high spatial resolution with isotropic voxel size of 1.5 mm, the available choices are between the interleaved EPI sequence with two segments and the HF-EPI sequence. From spatial resolution considerations, the SNR of the HF-EPI sequence is approximately 85 % of the SNR of the interleaved EPI sequence with two segments.
In the data from the HF-EPI sequence, the number of the sampling points in the phase encoding direction is only 106. To keep an isotropic voxel size of 1.5 mm, the FOV in the phase encoding direction has to be at least 159 mm. This is slightly smaller than the average size of a normal adult brain. Regional saturation pulses need to be implemented

to saturate the signal from outside of the FOV. This makes the implementation of the HF-EPI sequence more complicated. Alternatively, a slightly larger voxel size has to be used.

The images acquired by the HF-EPI sequence tend to suffer from image distortion and blurring. This makes the application to fiber tracking with diffusion tensors acquired from the HF-EPI sequence quite limited, because the result of the fiber tracking greatly relies on the alignment of the measured principal eigenvector with the direction of neuron fibers. Image distortion and blurring might lead to deviations in the estimation of the directions of eigenvectors which are difficult to quantify.

Considering the necessity to implement DTI with high spatial resolution, the interleaved EPI sequence with 2 segments becomes the sequence of choice, even though the SNR obtained is only 17.67 % of the equivalent 2D single shot EPI sequence and the acquisition time for the whole volume is 4 times longer.

An even larger number of averages is required in the interleaved EPI sequence of 2 segments because of the smaller voxel size, which leads to lower SNR. It is still intrinsically challenging to combine the data from two separate acquisitions into one single complete set in k-space. In the following chapter, we will propose a new method of averaging which requires no cardiac gating and, thus, allows a larger number of averages within the same time scale. Two selective averaging algorithms are analysed and compared.

	Single Shot EPI	HF-EPI	Interleaved EPI
$VoxelSize_x$	3mm	1.5mm	1.5mm
$VoxelSize_y$	3mm	1.81mm	1.5mm
$VoxelSize_z$	3mm	1.5mm	1.5mm
$Multiplex_x$	64	128	128
$Multiplex_y$	64	64	128
BW_x	BW	2 * BW	2 * BW
SNR	1	15.08 %	17.67 %
Scanning Time	1	2	4

Table 4.2: The table shows the relative SNR of the interleaved EPI and HF-EPI sequences to the 2D single shot EPI sequence with the imaging parameters used.

Chapter 5

Selective Averaging

As most methods for the reduction of the motion artefacts in the interleaved DT-EPI sequences are based on using cardiac gating, the total useable scanning window is greatly reduced to approximately 1 or 2 images per heartbeat compared with 3 to 4 images per second feasible without cardiac gating. However, as the number of averages increases, the intensity of the ghost due to motion will, in general, be reduced.

The pulsatile cardiac inflow only occurs during a short systolic period of about 200 to 400 msec after the peak of the R wave. Therefore, if we sample the data continuously and discard only the data contaminated by strong pulsatile motion acquired during the short systolic period, the averaged data can be relatively free from motion artefact. The total scanning time can thus be reduced. In the following sections, the technique of multiple averaging which requires no cardiac gating will be further explored. Selective averaging algorithms with thresholding are developed to extract the motion corrupted data and to allow for a larger number of averages within the same time limit .

5.1 Data Acquisition and Thresholding

5.1.1 Data Acquisition with Interleaved EPI

The interleaved EPI sequence was developed as described in Section 4.1 in Chapter 4. For each image, k-space data were acquired in two segments by performing two separate excitations. Multiple averages of the data were collected continuously without cardiac gating. After the acquisition of the full dataset, data were processed with the selective averaging algorithm described below for every individual slice.

The acquisition time per echo was 768 μsec, and the matrix size was 128 by 128. The field of view was 192 mm by 192 mm and the slice thickness was 1.5 mm, resulting in an isotropic voxel size of 1.5 mm. The sequence was tested *in vitro* on a gel phantom and *in vivo* on a healthy male volunteer. The effective echo time was 102 msec. The k-space was sampled asymmetrically as described in Chapter 3. Sixteen slices and 50 averages were acquired within one hour scan time for the *in vivo* measurements with high diffusion weighting. For *in vitro* data 16 slices and 60 averages were obtained in a scan time of 72 minutes with high diffusion weighting. For low diffusion weighted measurements, ten averages were measured in both cases.

The standard diffusion encoding scheme as described in the Section 2.6 in Chapter 2 was used. The diffusion weighting was implemented by using two 180 degree RF pulses and two pairs of diffusion weighting gradients as described in Section 4.3.2. The b factors chosen were 868 $\cdot 10^6 sec/m^2$ for measurements in the 3 principal directions, and 405 $\cdot 10^6 sec/m^2$ for measurements along the off-diagonal directions. The b factor for the low diffusion weighting measurement was 58 $\cdot 10^6 sec/m^2$.

5.1.2 Thresholding

Three navigator echoes were collected before the EPI data acquisition for each single excitation. The first and the third navigator echoes were averaged and Fourier-transformed to obtain a 'composite profile' for each segment. A reference profile was constructed by averaging the single composite profiles. Because motion leads to severe signal dropout in EPI data, motion contaminated segments must be excluded from the image calculation. Such segments can be detected easily by comparing the amplitude of the respective composite profiles to the averaged 'reference profile' and discarding the data from the averages if the amplitude from the respective profile is below a certain threshold value. In detail, the procedure was as follows:

(i) the averaged magnitude of all the composite profiles belonging to the same segment was calculated all through the averages and used as a 'reference profile';
(ii) the threshold was set to 80 percent of the amplitude of the reference profile;
(iii) if the amplitude of a composite profile was less than this threshold value, the data from the respective measurement were regarded as 'motion contaminated' and discarded.

5.2 Selective Averaging Algorithms

For the uncorrupted data, a one dimensional Fourier Transformation along the readout direction was performed. The phase information from the respective navigator echoes was extracted. The data were then phase corrected on a pixel-by-pixel basis. The corrected data were averaged either in complex or modulus domain as described in the following section.

Complex Averaging

The uncorrupted contributions to each segment were averaged after the phase correction. The averaged data for both segments were spliced together and a second Fourier Transformation was performed along the phase encoding direction, which produces the final image. This algorithm is thus based on the averaging of phase corrected complex data.

Modulus Averaging

Single uncorrupted contributions to both segments were first spliced together, after the phase correction, a second Fourier Transformation was performed and a modulus image calculated for each individual average. This was repeated for all uncorrupted contributions. Finally the single modulus images were averaged. This algorithm is thus based on the averaging of modulus image data instead of complex data. If one segment of a particular image was discarded, data from the corresponding segment in the next average were used instead.

5.3 A Phantom Study

Figure 5.1a shows the trace images of the gel phantom. Figure 5.1b shows the averaged ADC values measured in an ROI within the object for all slices. The images in Figure 5.1a are based on complex averaging (left) and modulus averaging (right). The mean ADC value, measured from the gel phantom under normal condition (1 atmosphere pressure, 20 $^{\circ}C$) was 2.04 $\pm$ 0.05 $\cdot 10^{-9} m^2/sec$ for complex averaging and 2.00 $\pm$ 0.02 $\cdot 10^{-9} m^2/sec$ for modulus averaging. The result is comparable to 2.05 $\cdot 10^{-9} m^2/sec$ for pure water measured under similar conditions reported by Harris et al (Harris & Woolf, 1980).

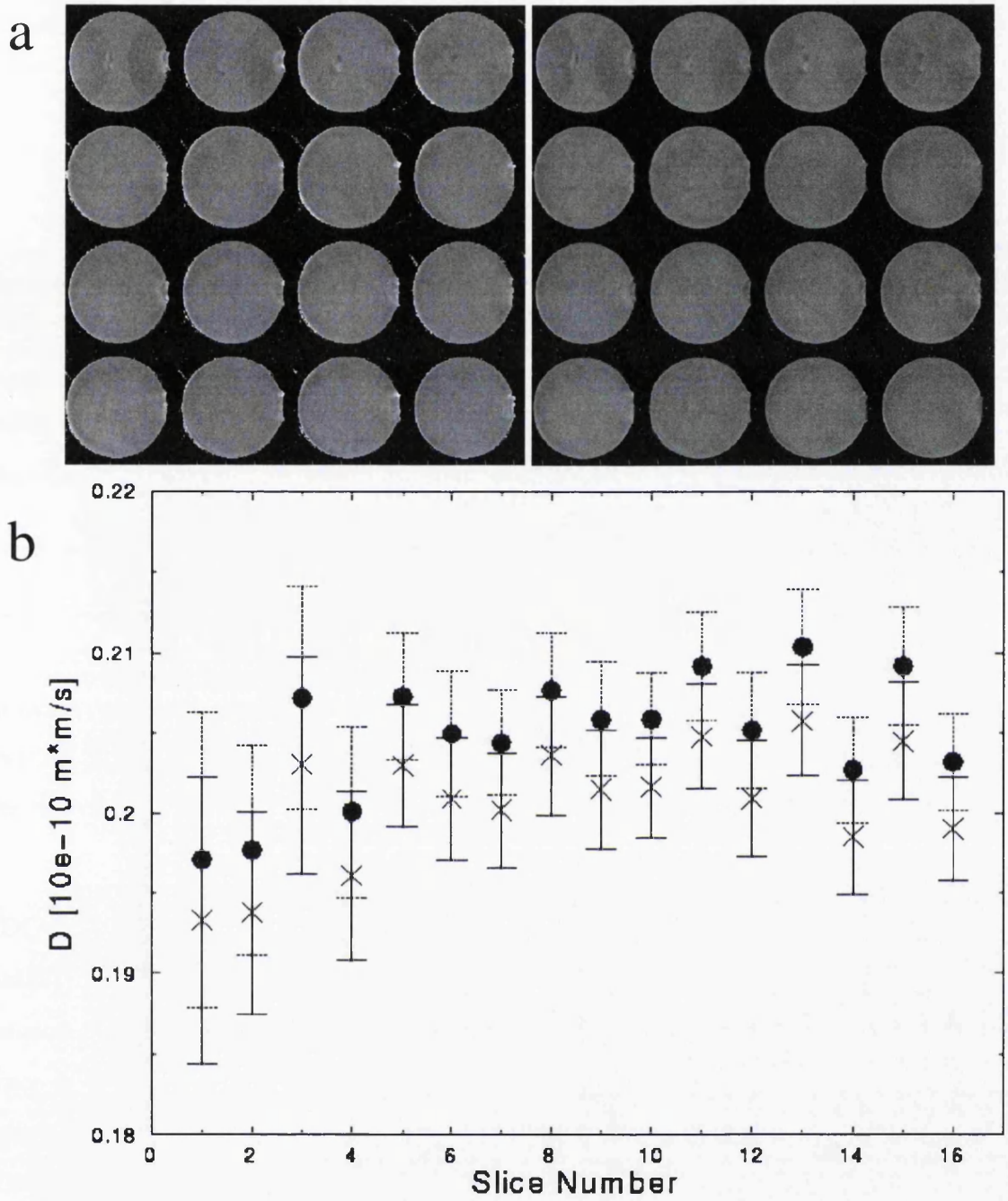

Figure 5.1: The trace images and ADC values of the gel phantom measured across all the slices with both averaging algorithms.

a: complex averaging (left) and modulus averaging (right).

b: ADC value from complex averaging (•), and ADC value from modulus averaging (×).

Direction of Diffusion Weighting	First Segment	Second Segment
Slice Selection	42.1	42.2
Read Out	42.4	42.8
Phase Encoding	49.4	49.8
Slice Selection/Read Out	42.8	43.3
Slice Selection/Phase Encoding	45.0	45.7
Read Out/Phase Encoding	44.8	44.9

Table 5.1: Average number of non-discarded data sets across all the slices in 6 diffusion encoding directions from both segments. The number of acquired averages was 50.

5.4 Study on the Human Volunteer

Table 5.1 shows the number of non-discarded data sets for human brain imaging, acquired over 16 slices for the *in vivo* experiment. The threshold for discarding contaminated data was 80 percent of the amplitude of the reference profile.

ADC values and Fractional Anisotropy were calculated from regions of interest in white matter (Splenium, Internal Capsule and Anterior Commissure) and in gray matter (Sensorimotor Cortex, Primary Visual Cortex and Anterior Cingulate). The values of Fractional Anisotropy from these ROIs are shown in Table 5.2. The averaged Fractional Anisotropy in white matter from Table 5.2 is comparable to the values in similar regions of white matter reported by Pierpaoli et al (Pierpaoli & Basser, 1996). In white matter, the averaged Fractional Anisotropy is 0.81 $\pm$ 0.07 in the Corpus Callosum and 0.72 $\pm$ 0.04 in the Anterior Internal Capsule. The value in gray matter reported by the same group in cortical gray matter is 0.31 $\pm$ 0.05, which is smaller than our result.
Figure 5.2 shows the Fractional Anisotropy map calculated pixelwise from the diffusion tensor for the whole volume (a) and for a selected slice (b).

White Matter	Internal Capsule	Splenium	Anterior Commissure
Complex Averaging	0.74 ± 0.13	0.82 ± 0.09	0.76 ± 0.11
Modulus Averaging	0.72 ± 0.14	0.77 ± 0.10	0.78 ± 0.11
Gray Matter	Sensorimotor Cortex	Primary Visual Cortex	Anterior Cingulate
Complex Averaging	0.46 ± 0.16	0.54 ± 0.13	0.47 ± 0.16
Modulus Averaging	0.41 ± 0.19	0.40 ± 0.11	0.42 ± 0.16

Table 5.2: Fractional Anisotropy calculated by both complex and modulus averaging algorithms in ROIs in white matter and gray matter.

5.5 Discussion

As expected in the motionless gel phantom, none of the data sets needed to be discarded during the averaging procedure. The trace images in Figure 5.1 based on complex averaging show greater noise and larger standard deviations than the trace images based on modulus averaging. Modulus averaging, which by definition did not require any phase information of the image, seems to produce less ghost. The ADC values calculated from the images based on complex averaging are consistently larger than the respective results based on modulus averaging. However, the difference between the mean ADC values is within the range of the standard deviation. The result is stable across all the slices except in the first three or four slices where the data was contaminated by ghosting artefacts as shown in Figure 5.1 a.

Figure 5.3 shows a single slice from the diffusion weighted data set with diffusion weighting gradients in the slice selection direction. The images were calculated by selective averaging and by simple averaging without discarding any data. It shows clearly the

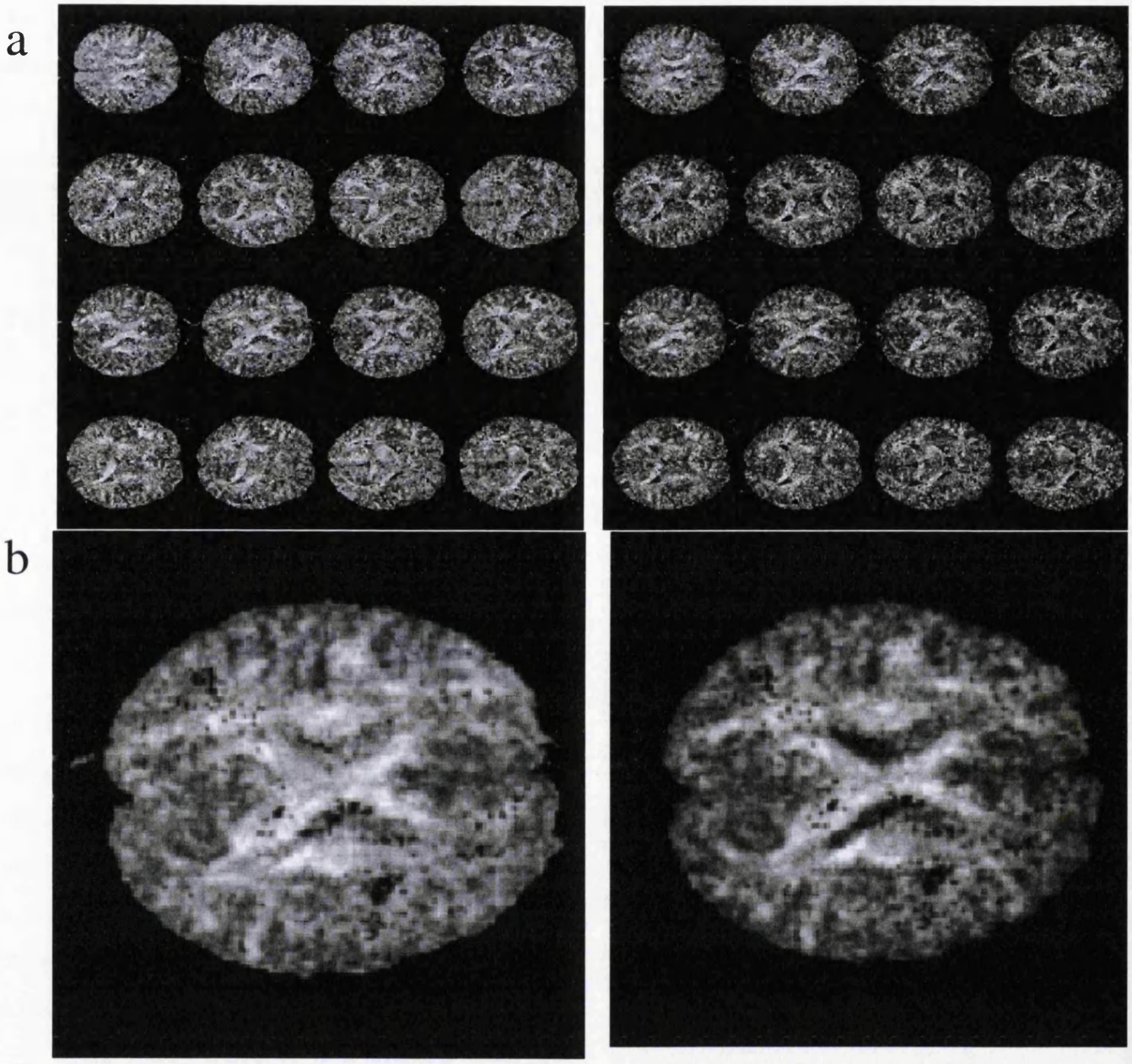

Figure 5.2: Fractional Anisotropy map from the human subject for the whole volume (a) and for a selected slice (b).

Left : complex average

Right: modulus average.

improvement in ghost suppression in diffusion weighted images with selective averaging. Without discarding the motion corrupted data, images with complex averaging show signal dropout noticeably in the areas nearby ventricles because of phase interferences. With modulus averaging, such phase variation forms overlapping ghost artefacts at the position of Half of FOV. With threshold at 80 % of the reference profile, both images from complex and modulus averaging show improvement.

The signal intensity from the ghost in the background was calculated for 5, 10, 20, 30, 40, 50 averages respectively with complex averaging. Compared with the signal measured from an ROI within the subject where the ghosting artefacts is not overlapping with the subject, Figure 5.4 shows that at least 30 averages are required in the selective averaging algorithm for the level of the ghost intensity to decrease below 20 % compared to the signal within the subject. However, even with 50 averages, the ghost level will only be reduced to 17 %.

In the human trace images in Figure 5.5, data from complex averaging shows increased variations and higher ADC values, which is consistent with the *in vitro* results. The discrepancy between the ADC values measured with both averaging algorithms may be due to the fact that if modulus averaging is applied, the averaged signal intensity in a region of interest will not approach zero for high diffusion weighting images but an offset value related to the noise level. This is misinterpreted as a slower decay which corresponds to a slightly lower ADC.

The averaged SNR in the diffusion weighted images is approximately 18:1 for both algorithms. Although the SNR in the diffusion weighted images based on modulus averaging is generally higher than in the images based on complex averaging, the difference in SNR is marginal. Table 5.1 shows that an average of 12 percent of the data (corresponding

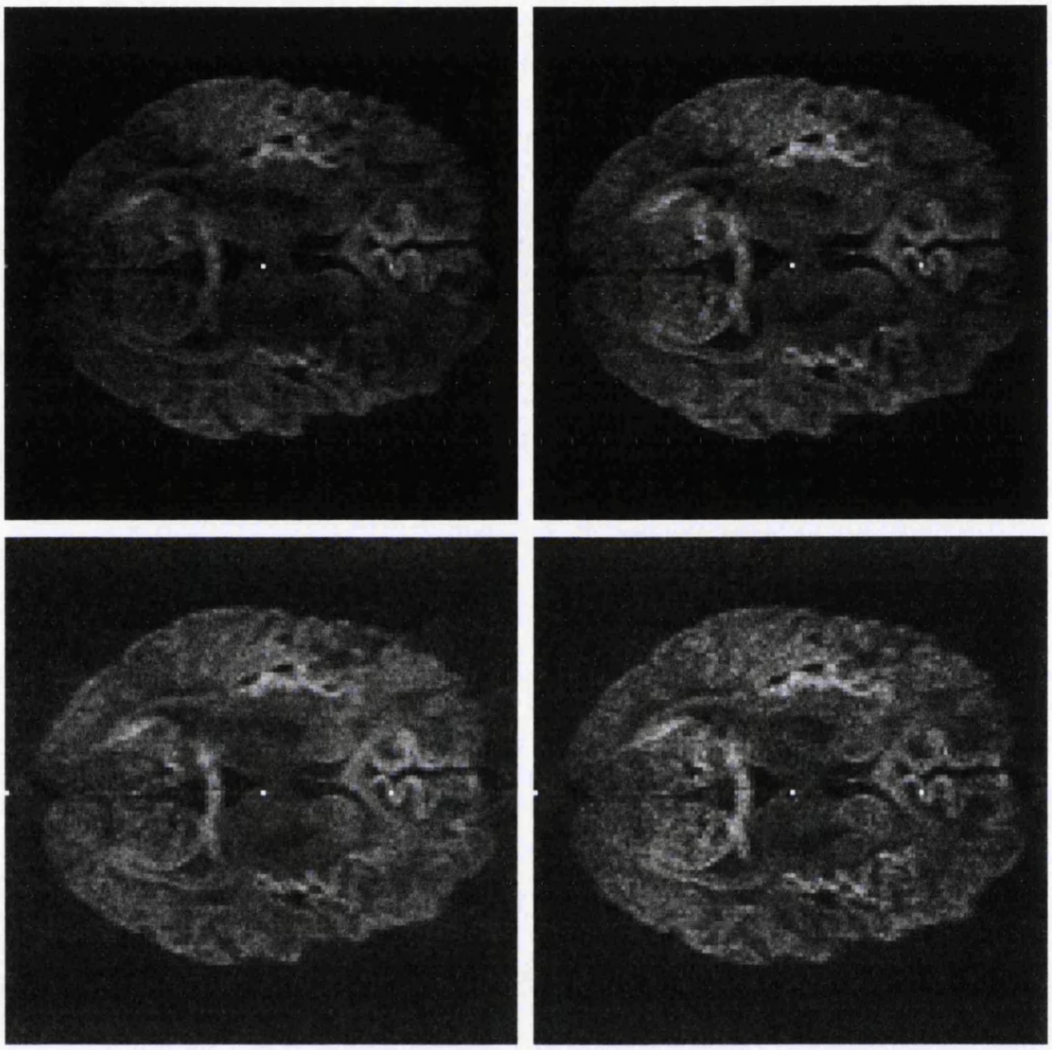

Figure 5.3: The figure shows the improvement of ghosting artefacts with selective averaging in the 2D interleaved EPI sequence with 2 segments.

Top Left: simple complex averages

Top Right: complex averaging with thresholding at 80 %.

Bottom Left: simple modulus averages

Bottom Right: modulus averaging thresholding at 80 %.

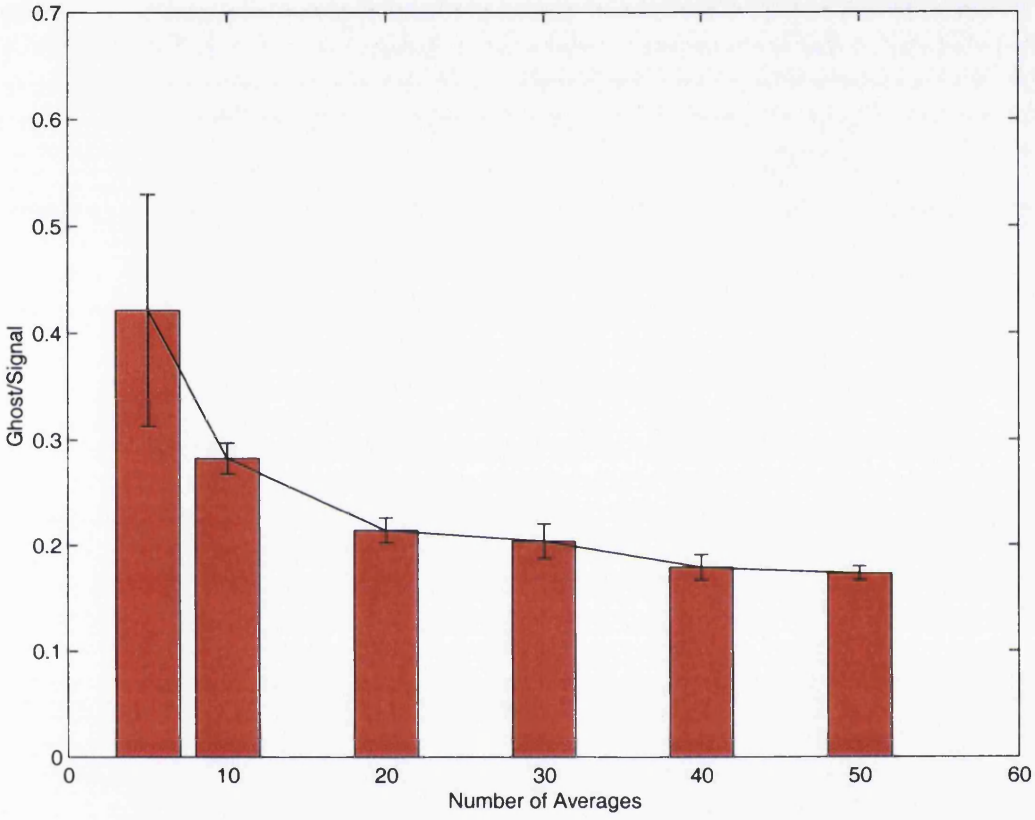

Figure 5.4: The figure shows the ratio of the intensity of the N/2 ghost and the intensity of the signal within the subject relative to the number of averages.

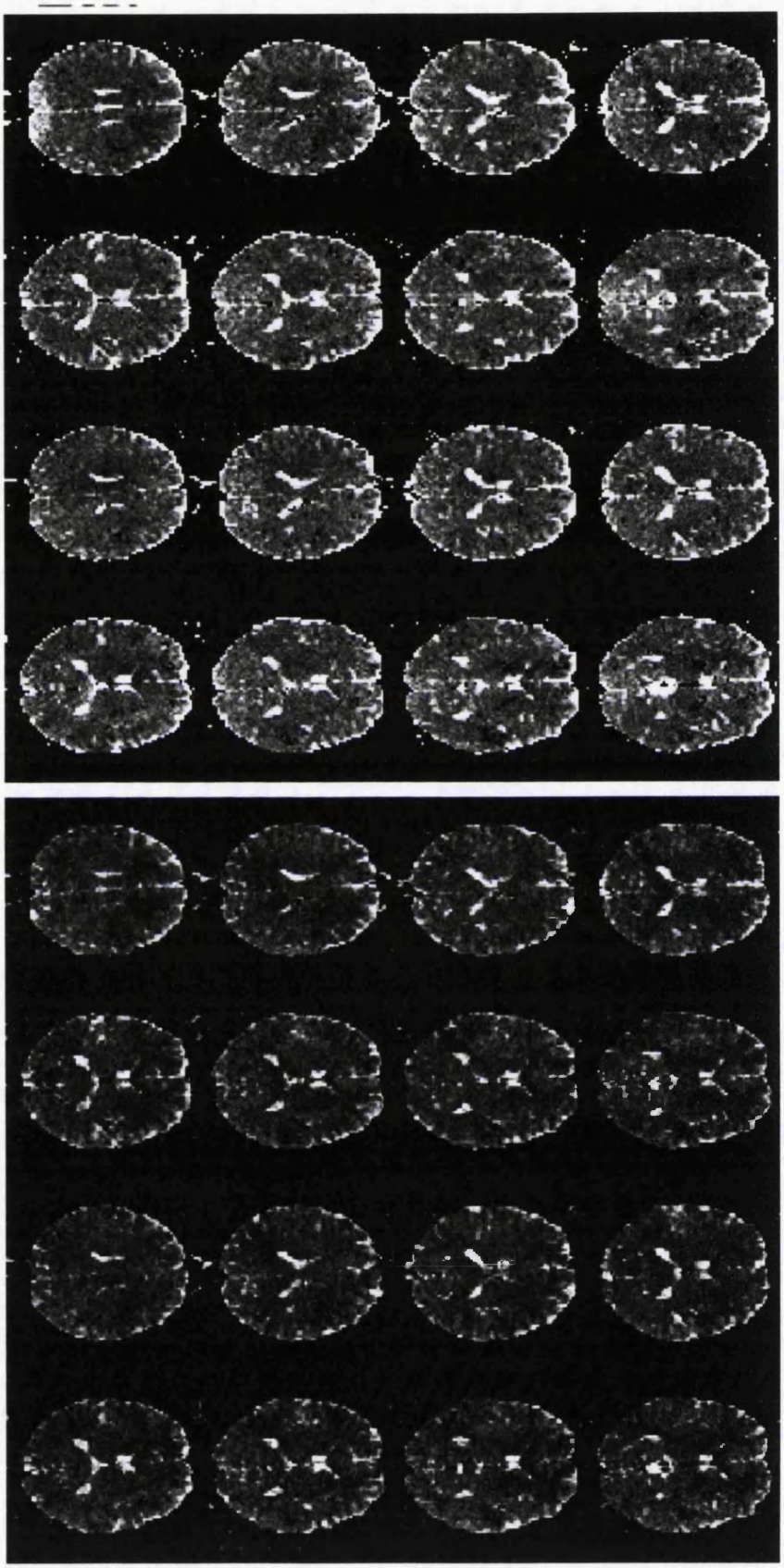

Figure 5.5: Trace images from a male human volunteer.

Top : complex average

Bottom: modulus average.

to approximately 6 measurements) was discarded due to motion artefacts. According to Table 5.1, these motion artefacts seem to be independent of the type of acquisition since the number of discarded measurements is similar for both segments. If the number of averages had been considerably different for both segments, this might have resulted in ghosting artefacts. Diffusion weighting images in the phase encoding direction also showed the lowest sensitivity to motion. The loss of raw data did not seem to have an appreciable effect on the ADC values.

The Fractional Anisotropy map showed significant differences between the different averaging algorithms. This is particularly obvious in areas such as the ventricle in Figure 5.2b. From Table 5.2 it can be seen that complex averaging tends to yield higher Fractional Anisotropy values than modulus averaging in both white matter and gray matter. This is also true for some ventricle regions.

5.6 Conclusion

The multi-shot EPI sequence is very susceptible to motion artefacts because it requires the combination of raw data from different acquisitions into one complete k-space data set. Conventional approaches using cardiac gating greatly extend the total acquisition time. Here we propose a selective averaging algorithm based on the information in navigator echoes. The data were sampled continuously and contributions contaminated by motion were discarded in post processing. This proved to be practical in diffusion tensor imaging.

After thresholding, the data were averaged in the modulus or complex format. Modulus averaging tends to under-estimate the measured ADC. Complex averaging, on the other hand, introduces complicated artefacts due to the phase interferences between segments. In the next chapter, a new ghost free acquisition sequence will be presented, and will be compared with the interleaved EPI sequence with 2 segments.

Chapter 6

Half-FOV DT-EPI

6.1 Phase Variations in the Interleaved EPI Sequence

To reconstruct a ghost free image in MRI, the phase of the data in k-space has to evolve smoothly without interruption. Any mismatch of such phase variation will lead to ghosting as demonstrated in Section 4.3.1.

Unfortunately, for data from separate acquisitions, such phase variations may arise from various sources such as motion and eddy currents. The amplitude of ghosting artefacts from random sources such as motion can be reduced by selective averaging as described in the previous Chapter 5. Yet, ghosts from reproducible sources such as eddy currents cannot be removed simply by multiple averaging. This chapter describes a technique designed to overcome phase mismatch artefacts in multi-shot EPI sequences.

6.2 Sequence of Half-FOV EPI

In Half-FOV EPI, images are created by combining magnitude data in the image domain. The phase information is purposely discarded to avoid the introduction of phase variations from separate acquisitions when splicing the data in k-space. The data are acquired continuously without cardiac gating.
The sequence structure is similar to the standard interleaved EPI sequence of two segments. However, in Half-FOV EPI, a modulus image is constructed from each segment. Each image only contains spatial information from half the object. The signal from the other half of the object is removed by pre-saturation. During the acquisition of one segment, only half of the raw data are collected with twice the step size between successive k-space lines. The FOV is reduced by 50 % for each image along one direction. The data were then Fourier Transformed and phase corrected with the information extracted from the three navigator echoes described in Section 4.3.3 to create one modulus image. The two modulus images are then combined in the image domain rather than in the time data domain. Because modulus images are combined, phase errors between the acquisitions of both segments will not lead to ghosting artefacts. No selective averaging was used here. Figure 6.1 shows the idea behind the sequence.

To avoid aliasing, the upper/lower part of the brain is saturated by partially selective saturation pulses applied throughout acquisition of the first/second segment respectively. The RF pulse used was a standard Siemens saturation pulse, which selectively excites half of the FOV. A spoiler gradient was applied immediately after the saturation pulse to null the signal. To improve the slice profile, the saturation pulse was repeated twice with spoiler gradients of different amplitudes. Figure 6.2 shows the residual longitudinal magnetization of a simulated excitation profile after single and double application of the saturation pulses.

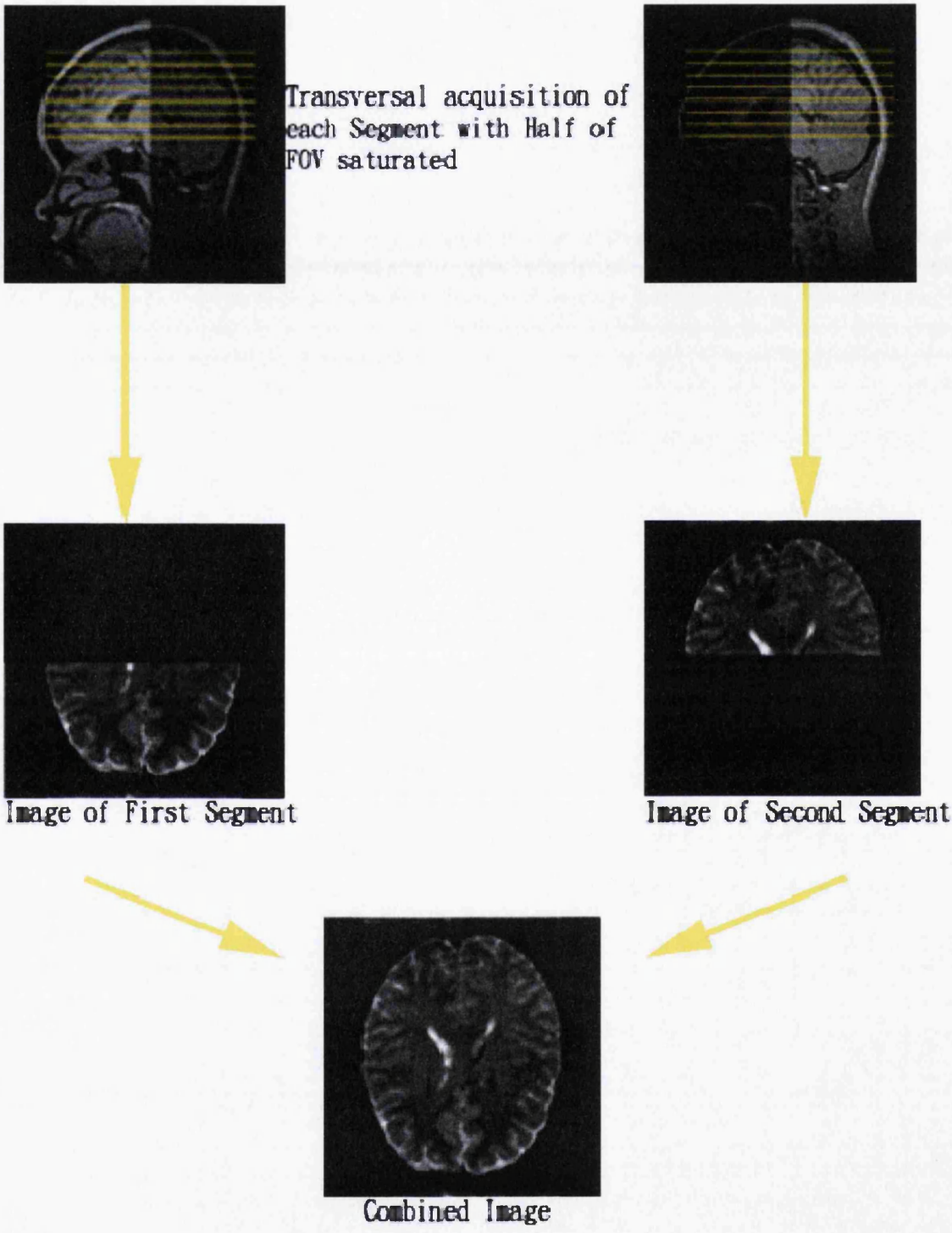

Figure 6.1: The diagram shows the acquisition order of the Half-FOV EPI sequence. Each segment acquires the data from half of the FOV. During the acquisition of one segment, the other segment is constantly saturated by applying a saturation pulse. The modulus data from both segments are combined later in the image domain.

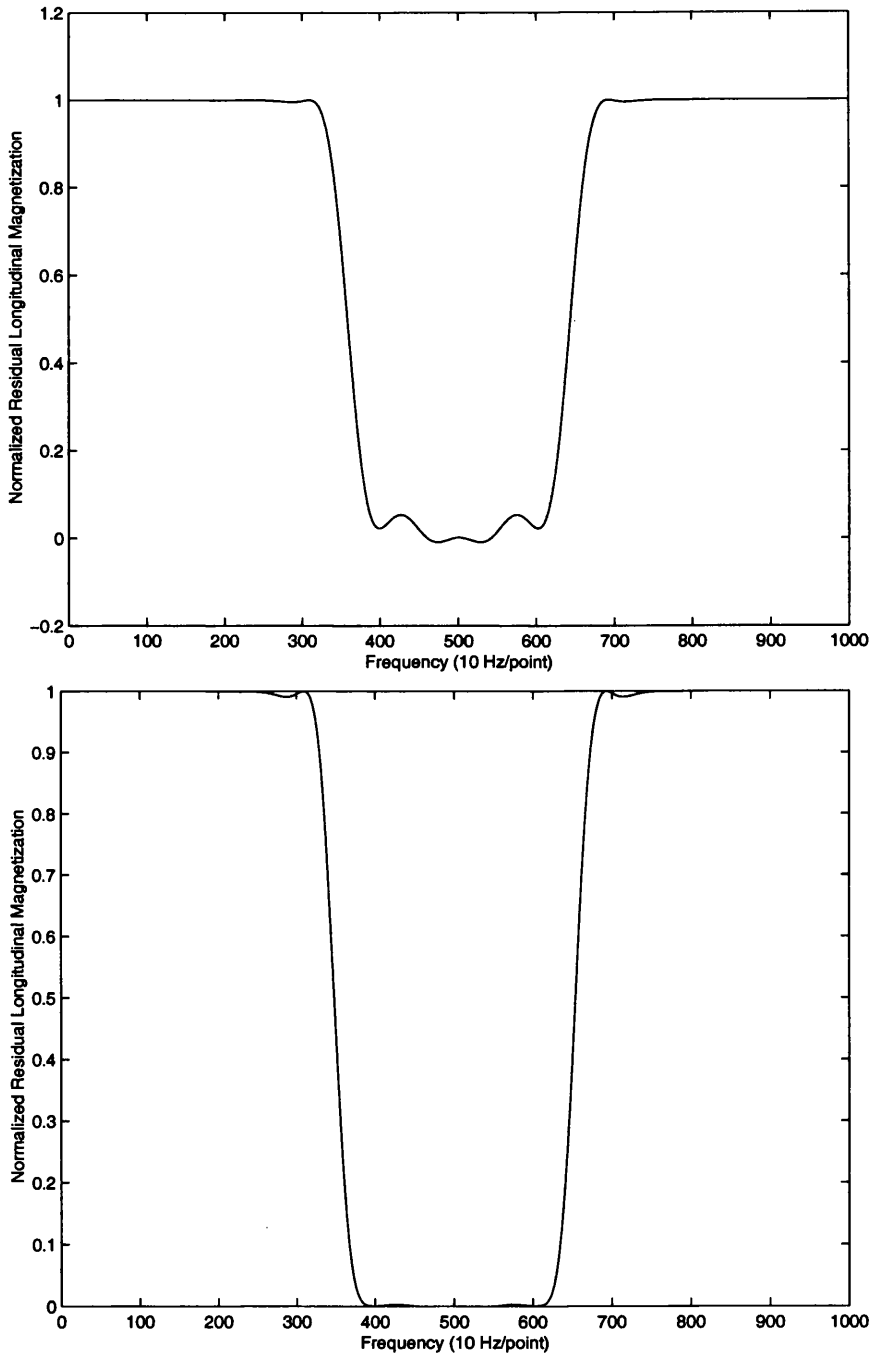

Figure 6.2: The figure shows the residual longitudinal magnetization after the application of the saturation pulse.

Top: The slice profile after the application of single saturation pulse.

Bottom: The slice profile after the application of two saturation pulses.

An additional time delay of 7000 msec was added after the acquisition of each segment to allow for full signal relaxation from the saturation pulse. This slowed down the acquisition speed considerably. However, during this time delay, it is possible to acquire slices in different positions. When large amount of slices were used to cover the whole brain, this time delay between segments became less important.

6.3 Study on the Phantom with Half-FOV DT-EPI

The sequence was implemented as a standard Spin Echo EPI sequence with the tetrahedral diffusion encoding scheme as described in Section 2.6 in Chapter 2. It was first tested on the Siemens water phantom. Eight slices of 1.5 mm isotropic voxel size were acquired with a matrix size of 128 by 128.

Table 6.1 shows the principal diffusion coefficients, the sorted eigenvalues, trace/3 and Fractional Anisotropy calculated from an ROI located outside the area of the overlapping ghost. The measured Fractional Anisotropy and trace/3 are 0.15 ± 0.05 and $1.99 \pm 0.07 \cdot 10^{-9} m^2/sec$ respectively. Compared with the values measured with the single shot EPI sequence from the same phantom, the difference in trace is 2.02 %. The difference in Fractional Anisotropy is 28.8 % but all the measured values are within the standard variations of the values calculated from the single shot EPI experiment.

6.4 Study of Human Brain with Half-FOV DT-EPI

The sequence was tested on two healthy males (aged 29 and 31). Fifty-two slices were acquired with 1.5 mm isotropic voxel size to cover the major part of the brain. The total acquisition time was approximately 63 minutes for 9 averages. The tetrahedral diffusion encoding scheme was used. An additional time delay of 1 msec was inserted

D_{xx}	1.88 ± 0.14
D_{yy}	1.87 ± 0.13
D_{zz}	2.20 ± 0.15
First eigenvalue	2.27 ± 0.13
Second eigenvalue	1.96 ± 0.10
Third eigenvalue	1.74 ± 0.10
Trace/3	1.99 ± 0.07
FA	0.15 ± 0.05

Table 6.1: The table shows the diagonal elements of the diffusion tensor, the sorted eigenvalues, trace/3 and Fractional Anisotropy of the water phantom measured with the Half-FOV EPI sequences. The values are given in unit of $10^{-9}m^2/sec$ except for Fractional Anisotropy which is dimensionless.

after ramping down the diffusion weighting gradient. Figure 6.3 shows, for one of the subjects, 52 slices of the diffusion weighted data with the weighting applied in the (-1, 1, 0) direction. Figure 6.4 and 6.5 show 52 slices of the trace/3 and the Fractional Anisotropy maps measured *in vivo.*

Table 6.2 shows the values of the diagonal elements of the measured diffusion tensor, trace/3 and Fractional Anisotropy from ROIs in white matter (Posterior Commissure), gray matter (Medial Parietal Cortex) and CSF in both subjects.

Compared with the previous measurement from the single shot DT-EPI sequences as shown in Table 3.2 in Chapter 3, the calculated trace/3 and Fractional Anisotropy values measured with the sequences of Half-FOV EPI are within a similar range for all tissue types. The advantage of the Half-FOV EPI sequence is that no cardiac gating is required because the phase variations between segments are discarded before image combination.

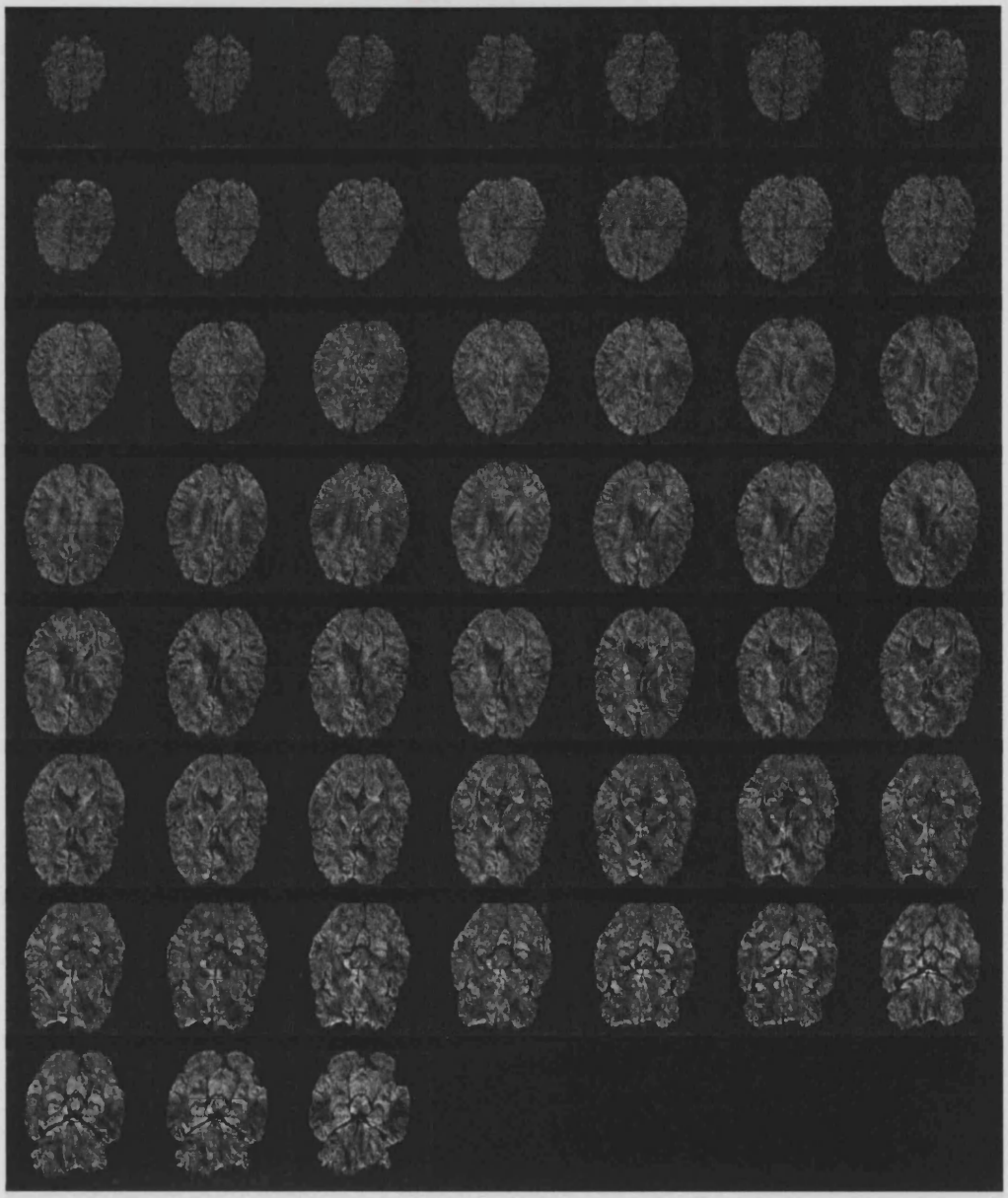

Figure 6.3: The figure shows 52 slices of diffusion weighted images from the brain acquired with the Half-FOV EPI sequences. The diffusion weighting gradients were applied in (-1, 1, 0) direction.

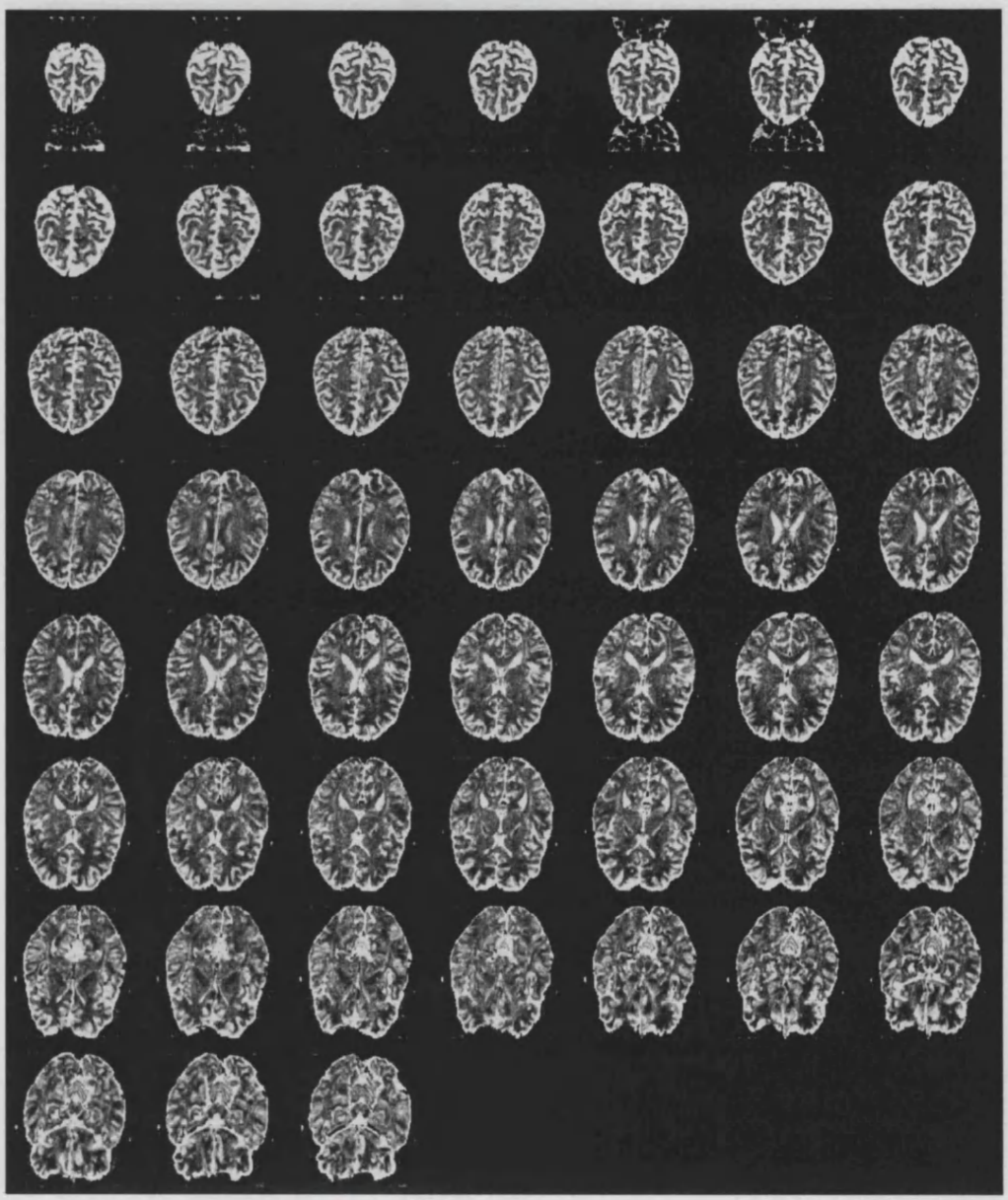

Figure 6.4: The figure shows 52 slices of the trace images of the volunteer acquired with the Half-FOV EPI sequences with 9 averages.

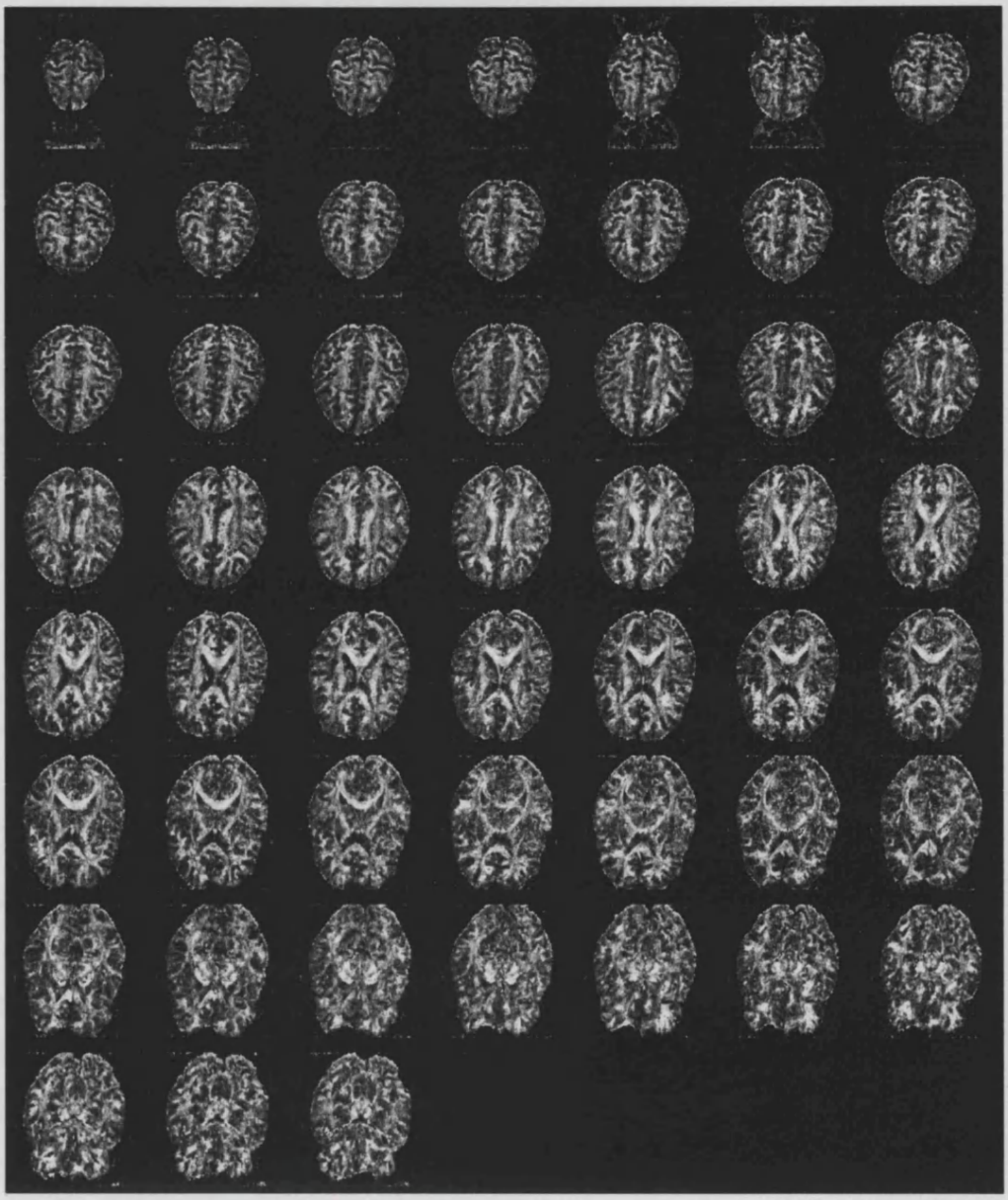

Figure 6.5: The figure shows 52 slices of the Fractional Anisotropy of the brain acquired with the Half-FOV EPI sequence with 9 averages.

	Posterior Commissure	Medial Parietal Cortex	CSF
D_{xx}	1.18 ± 0.32	0.72 ± 0.33	2.41 ± 0.37
	1.08 ± 0.46	0.70 ± 0.31	2.60 ± 0.36
D_{yy}	0.41 ± 0.23	0.87 ± 0.39	2.60 ± 0.33
	0.33 ± 0.19	0.88 ± 0.32	2.86 ± 0.34
D_{zz}	0.28 ± 0.21	0.89 ± 0.32	2.89 ± 0.36
	0.43 ± 0.24	0.99 ± 0.33	2.87 ± 0.29
Trace/3	0.60 ± 0.12	0.86 ± 0.30	2.72 ± 0.29
	0.63 ± 0.16	0.87 ± 0.26	2.78 ± 0.14
Fractional Anisotropy	0.94 ± 0.10	0.45 ± 0.17	0.24 ± 0.11
	0.95 ± 0.12	0.44 ± 0.16	0.17 ± 0.05

Table 6.2: The table shows the averaged values of the diagonal components of the diffusion tensor along the principal directions, the trace/3 and the Fractional Anisotropy from ROIs in CSF, Posterior Commissure and Medial Parietal Cortex for both the volunteers measured with the Half-FOV EPI sequences. Diffusion values are given in units of $10^{-9}m^2/sec$. The Fractional Anisotropy is dimensionless.

The sequence is slower compared to the standard interleaved EPI sequence with two segments because of the additional time delay between the acquisitions of separate segments. This time delay is required for the full relaxation of the spins from the saturation. Because of the saturation pulses applied constantly to half of the brain throughout the acquisition, it is potentially prone to exceeding the limit of SAR. Such saturation pulses and the subsequent spoiler gradients can also potentially lead to artefacts due to stimulated echoes. It is therefore essential to adjust the time delay between the acquisitions of separate segments, and after the diffusion weighting gradients, to minimise the extent of the ghost and to speed up the data acquisition.

Chapter 7

DT-EPI with High Spatial Resolution

7.1 Methods and Material

The Half-FOV EPI sequence was compared with other high resolution DT-EPI techniques developed in the project. Six healthy subjects (5 males and 1 female aged between 23 and 31, average age 25 $\pm$ 3.6 years) were scanned. The total scanning time was one hour per subject. The sequences used for comparison were single shot EPI, Half-FOV EPI and interleaved EPI. The Half-FOV EPI and interleaved EPI sequences were tested with and without cardiac gating. The tetrahedral diffusion encoding scheme was used in all sequences. Table 7.1 shows the parameters used in the experiment. The scanning time was calculated for the time duration required for the measurement of the full diffusion tensor. It was only an estimation for the sequences with cardiac gating. It should be noticed that in the case of the interleaved EPI sequence without cardiac gating, only 14 averages instead of 24 were acquired for the low diffusion weighted measurement.

Sequence	Isotropic Voxel Size	Averages	Slices	Scanning Time
Single Shot EPI	3mm	15	8	2.7 min
Interleaved EPI with gating	1.5 mm	6	8	11.2 min
Interleaved EPI without gating	1.5 mm	24	8	10 min
Half-FOV EPI with gating	1.5 mm	3	8	14 min
Half-FOV EPI without gating	1.5 mm	6	26	11.2 min

Table 7.1: The table shows parameters used for the comparison of the single shot EPI, interleaved EPI, and Half-FOV EPI sequences. Scanning time for triggering is an estimation.

For the sequences with cardiac gating, ECG leads were placed on the left shoulder, right shoulder and below the left rib. The scanner was triggered 400 msec after the detection of an R wave during the cardiac cycle.
For the sequences without cardiac gating, data were acquired continuously. The complex averaging algorithm described in Chapter 5 was used to process the non-motion contaminated data from the interleaved EPI sequence without cardiac gating. The threshold for discarding motion contaminated data was 85 % of the amplitude of the averaged reference profile.

7.2 Result from Comparison

7.2.1 Signal-to-Noise Ratio

In MRI, signal from the echo covering the centre of k-space normally has the highest impact on the intensity of the reconstructed image. Usually this echo is acquired in the

centre of the acquisition window. However, to reduce signal losses due to the T_2 decay, in all sequences, this echo was acquired at the end of the first quarter of the acquisition window, thereby asymmetrically sampling k-space (Hennel & Nedelec, 1995).
In the Spin Echo diffusion weighted sequence, the spins are refocused by a 180 degree RF pulse. The time between spin echo formation and the 180 degree RF pulse is the same as the time between the 90 degree and 180 degree RF pulses. In this project, the echo time TE is defined as the time between the 90 degree RF pulse and the spin echo formation. If there is an additional time delay, TB, between the spin echo formation and the acquisition of the gradient echo covering the centre of k-space, the MR signal will be subject to an extra decay. During the time TE between the 90 degree excitation RF pulse and spin echo formation, the MR signal experiences T_2 relaxation. There is an additive T_2^* relaxation during the time TB. This relaxation behaviour can be described by Equation 7.1:

$$S(TE) = S(0) \cdot e^{\frac{-TE}{T_2}} \cdot e^{\frac{-TB}{T_2^*}} \tag{7.1}$$

The SNR depends on imaging parameters, relaxation times, the receiver gain and other hardware-specific parameters, as discussed in Section 4.4. Table 7.2 shows the imaging parameters used in the various sequences and the theoretical SNR relative to the SNR of the single shot EPI measurement. The T_1 relaxation was ignored because of the long TR used in both the interleaved DT-EPI and the Half-FOV DT-EPI sequences. For calculation, T_2 and T_2^* in the brain were assumed to be 100 msec and 60 msec respectively.

The advantage of multiplexing in the x direction is compensated by the double sampling bandwidth which was necessary to keep the acquisition time per echo constant. In the interleaved EPI sequence of 2 segments, the SNR is increased by a factor of $\sqrt{2}$ because of multiplexing in the y direction. In Half-FOV EPI, data were combined in the image domain. Thus, there is no multiplexing in the phase encoding direction. This sequence also has a slightly longer TE and TB, because of a short time delay placed after ramping

	Single Shot EPI	Interleaved EPI	Half-FOV EPI
Matrix	64 by 64	128 by 128	128 by 128
Voxel Size	3mm	1.5mm	1.5mm
Bandwidth	BW	2* BW	2 * BW
Multiplex in X direction	1	2	2
Multiplex in Y direction	1	2	1
TE	80 msec	82 msec	82 msec
TB	19.1msec	18.1 msec	19.1 msec
SNR Predicted	1	17.63 %	12.26 %

Table 7.2: The table shows the parameters used by the sequences in comparison and the SNR expected in both the Interleaved EPI and Half-FOV EPI sequences relative to the single shot EPI sequence.

down the diffusion weighting gradients.

The signal for each sequence applied *in vivo* was calculated from the averaged value inside an ROI in the Posterior Commissure in the low diffusion weighted images from one single measurement. Noise was calculated from the standard deviation in an ROI in the background outside the brain and the Nyquist ghost. To avoid saturation effects, in the single shot EPI sequence, the first measurement was used. For the other sequences, a full T_1 relaxation may be assumed due to the long TR values. The SNR was calculated from the third or a later measurement which displayed minimum ghosting. The top part of Figure 7.1 shows the SNR for all subjects and all sequences.

The measured SNR for all sequences relative to the measured SNR for the single shot EPI sequence was calculated for all subjects. The bottom part of Figure 7.1 shows the averaged results and standard deviations (solid line), and the theoretical results (red solid bars).

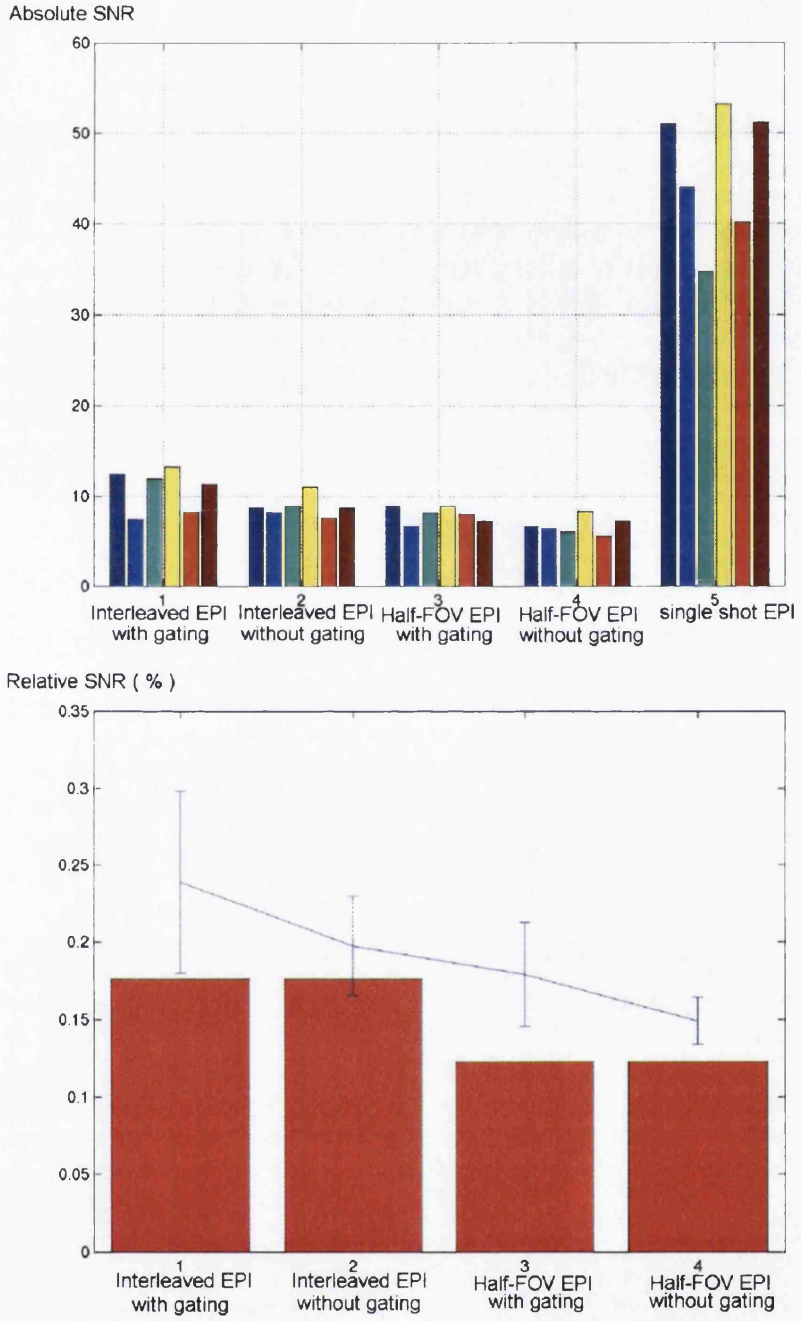

Figure 7.1: The figure shows the SNR from an ROI in the Posterior Commissure for all sequences and all subjects.

Top: The Absolute SNR. Each solid bar indicates the SNR for each individual, which was repeated for different sequences.

Bottom: The percentage of the SNR of the sequences of high resolution relative to the SNR of the single shot EPI sequence. The solid line shows the SNR averaged over all subjects and was displayed for four different sequences of interest. The red bars show the predicted theoretical values.

Sequence	CSF	Posterior Commissure	Medial Parietal Cortex
Single Shot EPI	2.14 ± 0.28	0.79 ± 0.18	0.84 ± 0.10
Interleaved EPI with gating	2.62 ± 0.24	0.81 ± 0.12	0.86 ± 0.19
Interleaved EPI without gating	3.35 ± 0.40	1.26 ± 0.21	1.14 ± 0.21
Half-FOV EPI with gating	2.83 ± 0.26	0.70 ± 0.15	0.79 ± 0.21
Half-FOV EPI without gating	2.50 ± 0.23	0.68 ± 0.15	0.74 ± 0.19

Table 7.3: The table shows the averaged values of trace/3 for all sequences in ROIs in CSF, white matter (Posterior Commissure) and gray matter (Medial Parietal Cortex). All values are given in units of $10^{-9} \cdot m^2/sec.$

7.2.2 Apparent Diffusion Coefficient

Figure 7.2 shows the diagonal diffusion coefficients in the measured diffusion tensor from different DT-EPI sequences.

7.2.3 Trace

The values of trace/3 were calculated from ROIs in white matter (Posterior Commissure), gray matter (Medial Parietal Cortex) and CSF for all subjects and for all sequences. The averaged values are shown in Table 7.3. Figure 7.3 shows one slice of the trace image from one subject for various sequences.

7.2.4 Fractional Anisotropy

The values of the Fractional Anisotropy were calculated from the same ROIs as in the trace/3. Figure 7.4 shows one slice of the Fractional Anisotropy map from one subject measured with various sequences in the DT-EPI comparison experiment. Table 7.4 shows

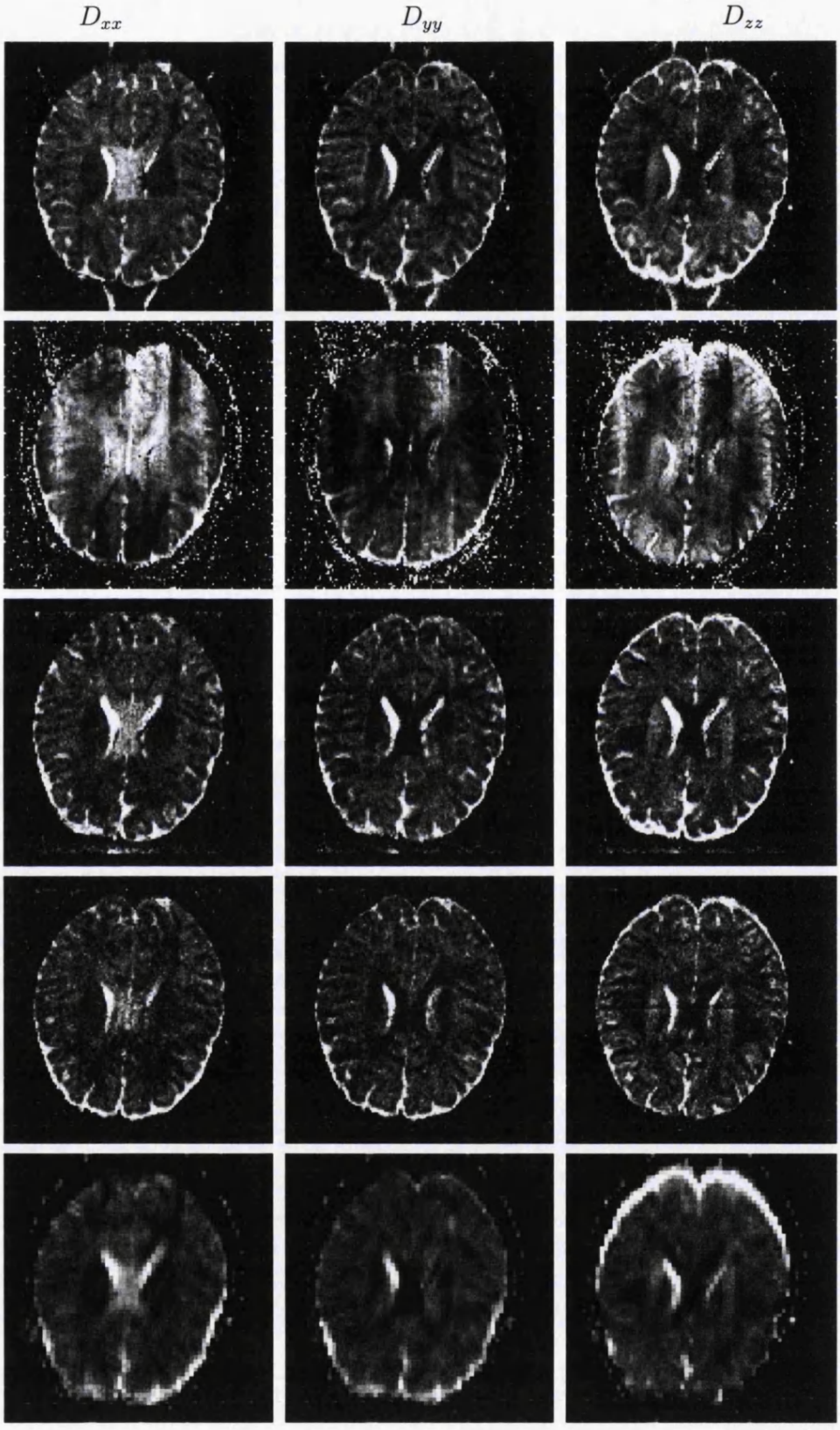

Figure 7.2: The figure shows the diagonal components of the diffusion tensor along the three principle directions measured with different DT-EPI sequences.
Row 1: Interleaved DT-EPI with gating. Row 2: Interleaved DT-EPI without gating. Row 3: Half-FOV DT-EPI with gating. Row 4: Half-FOV DT-EPI without gating. Row 5: Single Shot DT-EPI

Without Cardiac Gating With Cardiac Gating

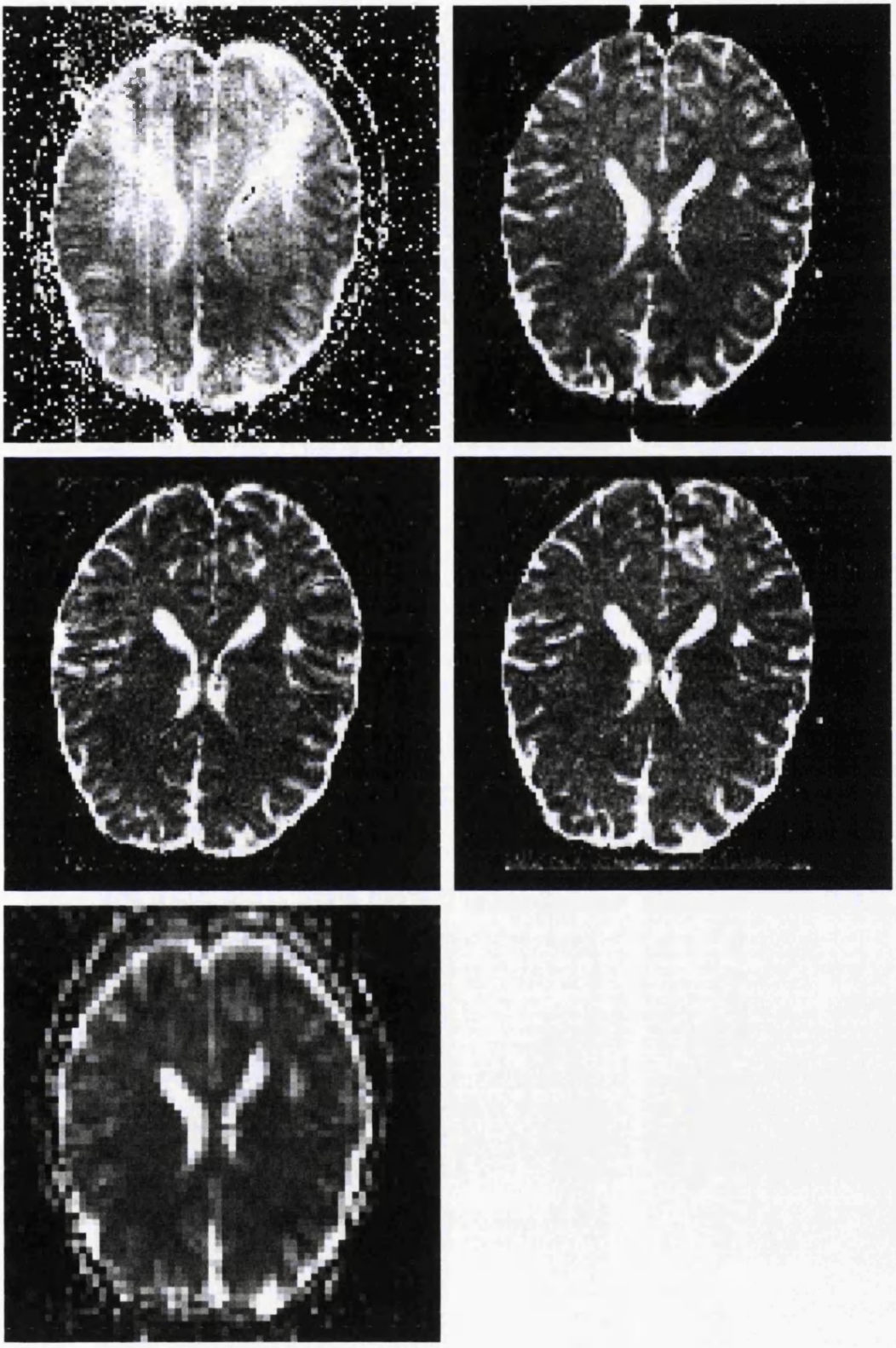

Figure 7.3: The figure shows one slice of the trace image for one subject measured with different DT-EPI sequences.

Top Row: Measured by the interleaved EPI sequences.

Middle Row: Measured by the Half-FOV EPI sequences.

Bottom Row: Measured by the single shot EPI sequences.

Sequence	CSF	Posterior Commissure	Medial Parietal Cortex
Single Shot	0.28 ± 0.09	0.83 ± 0.10	0.30 ± 0.09
Interleaved EPI with gating	0.21 ± 0.08	0.89 ±0.10	0.45±0.14
Interleaved EPI without gating	0.38 ±0.11	0.85 ± 0.09	0.53 ± 0.13
Half-FOV EPI with gating	0.26 ± 0.09	0.92 ± 0.13	0.50 ± 0.17
Half-FOV EPI without gating	0.23 ± 0.09	0.90 ± 0.12	0.51 ± 0.17

Table 7.4: The table shows the Fractional Anisotropy averaged among subjects in ROIs in CSF, Posterior Commissure and Medial Parietal Cortex measured with sequences in comparison.

the averaged values of Fractional Anisotropy among the subjects.

7.3 Discussion

The single shot DT-EPI sequences are the fastest in the comparison. The major disadvantage is the low spatial resolution, which largely restricted its application. Two multi-shot DT-EPI sequences with high spatial resolution were developed during the project. The result of the comparison is discussed in the following section.

7.3.1 Acquisition Speed

Within approximately the same acquisition time, the largest number of averages may be achieved with the interleaved EPI sequence of two segments without cardiac gating. The number of averages is almost 8 times higher than for the Half-FOV EPI sequence with cardiac gating. Unfortunately, the interleaved EPI sequence suffers from ghosting

Without Cardiac Gating With Cardiac Gating

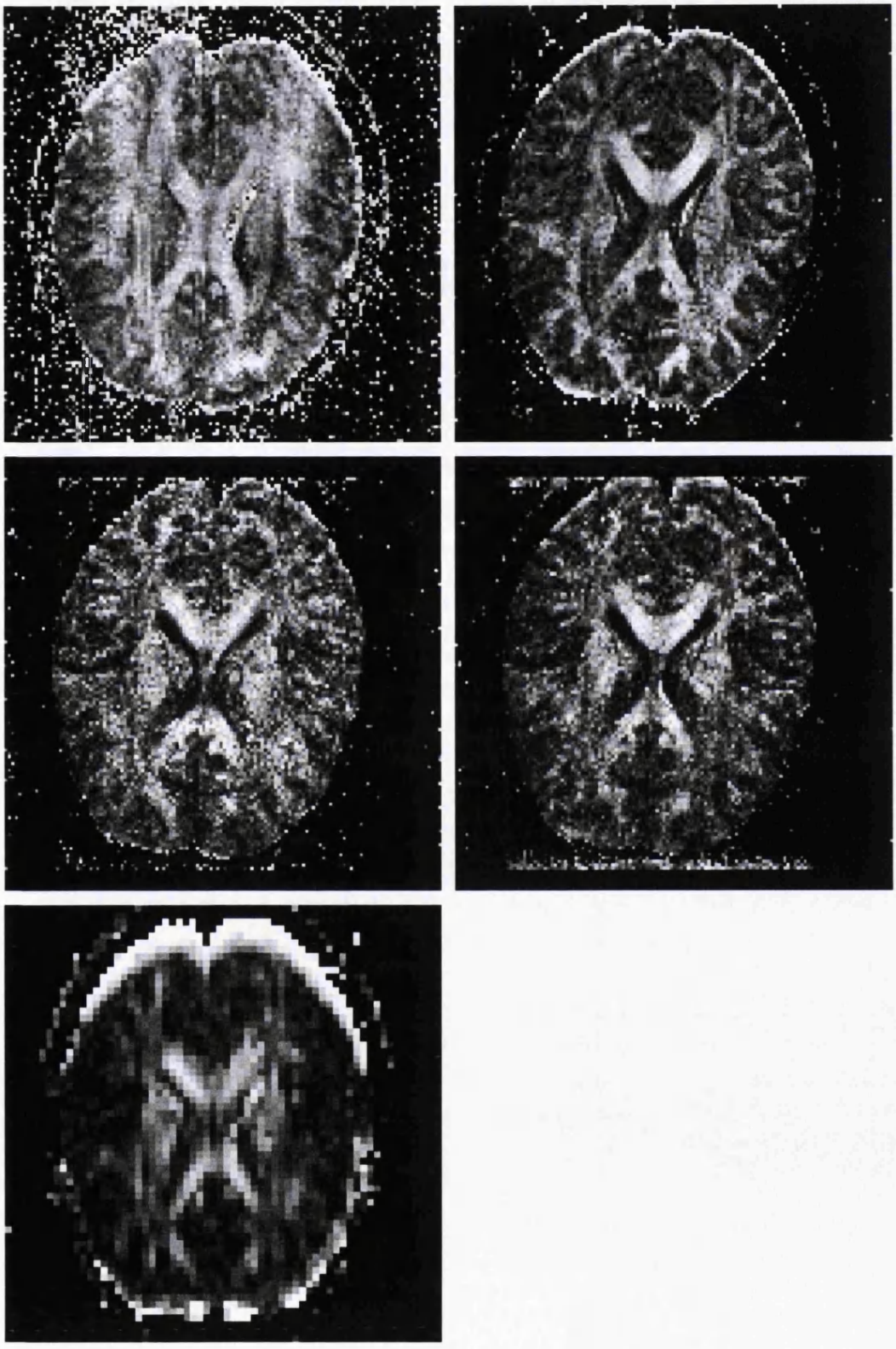

Figure 7.4: The figure shows one slice of the Fractional Anisotropy map of one subject measured with sequences in the DT-EPI comparison experiment.

Top Row: Measured by the interleaved EPI sequences.

Middle Row: Measured by the Half-FOV EPI sequences.

Bottom Row: Measured by the single shot EPI sequences.

artefacts due to phase mismatch between the segments. Such phase variations can result from subject bulk head motion, involuntary pulsatile inflow or eddy currents. Even though the motion contaminated data were discarded through selective averaging as described in Chapter 5, the intensity of the ghost would still be high. The diffusion weighted images are thus contaminated by interfering artefacts.

Cardiac gating is generally used to reduce motion artefacts. In the interleaved EPI sequences, gated acquisitions are four times slower than non-gated ones. Unfortunately, the ghosting artefacts in the interleaved EPI sequence cannot be removed completely by cardiac gating because the phase variations arise from various sources in addition to cardiac motion. The intensity of the residual ghost in the background ranges from approximately 25 % to 30 % of the signal in the brain, measured where the ghost is not overlapping with the brain in the interleaved EPI sequences with cardiac gating.

In the Half-FOV EPI sequence, signal from the other half of the FOV was constantly saturated during acquisition of one segment. A time delay was required for the full signal relaxation before the acquisition of the second segment. Yet, it is possible to collect data from slices at different positions during this time delay. In the experiment, for the Half-FOV EPI sequences without cardiac gating, 26 slices with 6 averages were acquired within 11.2 minutes. The interleaved EPI sequence without cardiac gating would be able to acquire 8 averages of the same number of slices within the same time. Yet images acquired with the Half-FOV EPI sequence are free from the ghosting artefacts prevailing in all the interleaved EPI sequences.

No Nyquist ghost was found in the images acquired with the sequences of Half-FOV EPI, because the data were combined in the image domain. Cardiac gating did not affect the ghost level in the final images. Therefore in the sequence of Half-FOV EPI, cardiac gating increases the acquisition time without changing the ghost intensity.

Technically, the scanner was triggered by detecting the R-R peaks in the ECG signal. It was noticed that the recorded ECG signal was influenced by the image acquisition process. This leads to irregular triggering patterns. Figure 7.5 shows one of the ECG

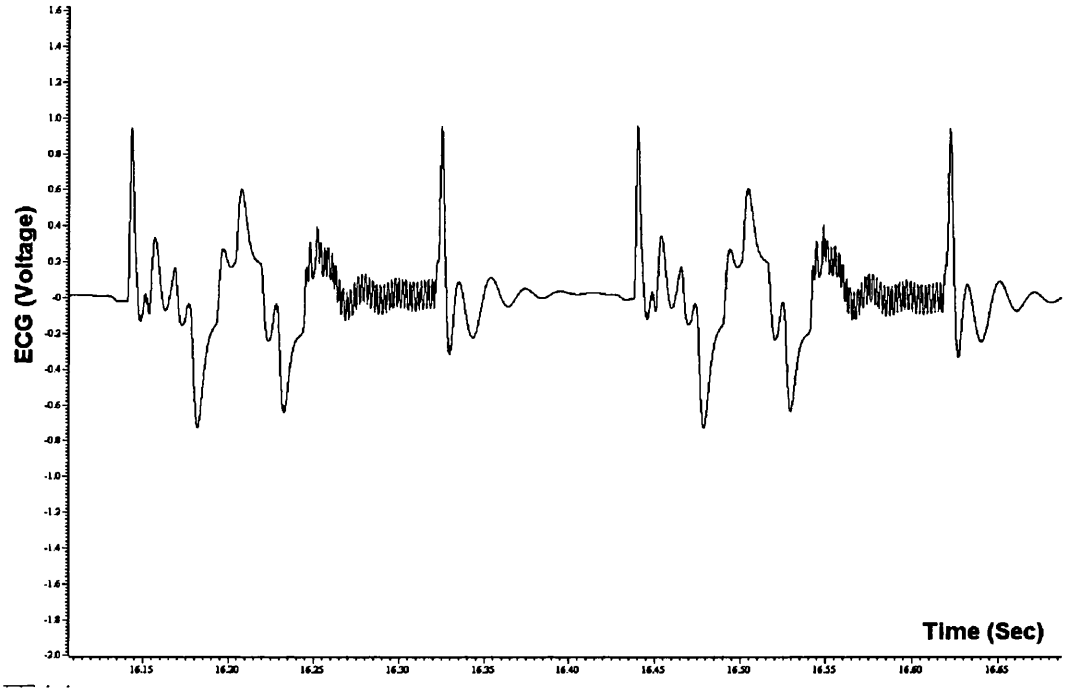

Figure 7.5: The figure shows the recorded ECG curve within the scanner from a normal volunteer during the diffusion tensor imaging experiment.

recordings from inside the scanner. The recorded ECG signal can be affected by motion due to the vibration of the scanner bed induced by the strong diffusion weighting gradients or by patient body movement. Because the ECG signal is an indirect measurement of the physiological flow, it might be more accurate to trigger the scanner with signal from infrared detectors placed on the finger tip of the subject, which offers a more direct estimation of the pulsatile flow than ECG recording.

7.3.2 SNR

The SNR is generally higher and with larger variations for the gated sequences compared with the non-gated counter part. The SNR of the non-cardiac gated sequences is ap-

proximate 82.5 % of the SNR of the cardiac gated versions for both sequence types. The averaged SNR in the interleaved EPI sequence with cardiac gating was $25.12 \pm 6.23\%$ compared with $20.76 \pm 3.39\%$ in the non-gated version. In the Half-FOV EPI sequence, the SNR in the cardiac gated acquisition was $18.82 \pm 3.54\%$ compared with $15.64 \pm 1.61\%$ in the non gated acquisition.

The SNR of the Half-FOV EPI sequence is approximate 75 % of the SNR of the interleaved EPI sequence, which is close to the theoretical value of 69 %. The measured SNRs from the interleaved EPI sequences and the Half-FOV EPI sequence are higher than the theoretical values relative to the SNR of the single shot EPI sequence, as shown in the bottom part of Figure 7.1. This difference could be due to assumptions made of the T_2 and T_2^* values in the brain. It might also result from the choice of ROIs in white matter during the measurements of SNR, which can be affected by the partial volume artefacts in the single shot EPI sequences.

7.3.3 Trace

From Table 7.3, the calculated values of trace/3 obtained with the interleaved EPI sequences with cardiac gating and the Half-FOV EPI sequences with and without gating are quite close to the values measured with the single shot EPI sequence. However, the values of trace/3 are in general higher for the Half-FOV EPI sequences with cardiac gating than for the non-gated counter part.

The values of trace/3 measured with the interleaved EPI sequences without cardiac gating are generally higher than the values measured with all the other sequences and are contaminated by ghosting artefacts. The ghosting artefact does affect the accuracy of the measurement, which excludes the interleaved EPI sequence as the choice for the measurement of the trace.

The trace values measured with the Half-FOV EPI sequence with and without cardiac

gating are similar to each other for all three types of tissues, but are smaller than the values measured with the single shot EPI sequence and the interleaved EPI sequence with cardiac gating. However, the values are close to the results from the measurements in Chapter 3. One reason for the variations in the trace values might be the choice of the ROI in the brain.

The bottom part of Figure 7.6 shows for one slice the difference of the trace images measured with the Half-FOV EPI sequences (Top Left) and the single shot EPI sequences (Top Right). The image of the trace measured with the single shot EPI sequences was interpolated to a matrix size of 128 by 128 by zero filling. Since the slice thickness of the trace image measured with the sequences of single shot EPI was 3 mm, two images of the trace of slice thickness 1.5 mm measured with the Half-FOV sequences without cardiac gating from adjacent slices were averaged to produce the equivalent image for comparison. The subtraction image was calculated from the subtraction of the traces measured with both sequences and divided by the averaged values of the traces.

Figure 7.6 shows clearly the effects of the different degree of image distortion in the different images: notably near the edges of the brain and nearby the ventricles, where the partial volume artefacts are prominent. There are subtle differences in some cortical regions, especially around the Medial Parietal cortex.

7.3.4 Fractional Anisotropy

The calculated values of Fractional Anisotropy measured with different sequences are quite similar in all types of tissues, as shown in Table 7.4. The Fractional Anisotropy measured with the Half-FOV EPI sequences was generally higher in similar ROIs. Because of the ghosting artefacts, the value of Fractional Anisotropy measured with the interleaved EPI sequences without cardiac gating was different from the values measured with the other sequences in the comparison.

The values of Fractional Anisotropy in white matter (Posterior Commissure) measured

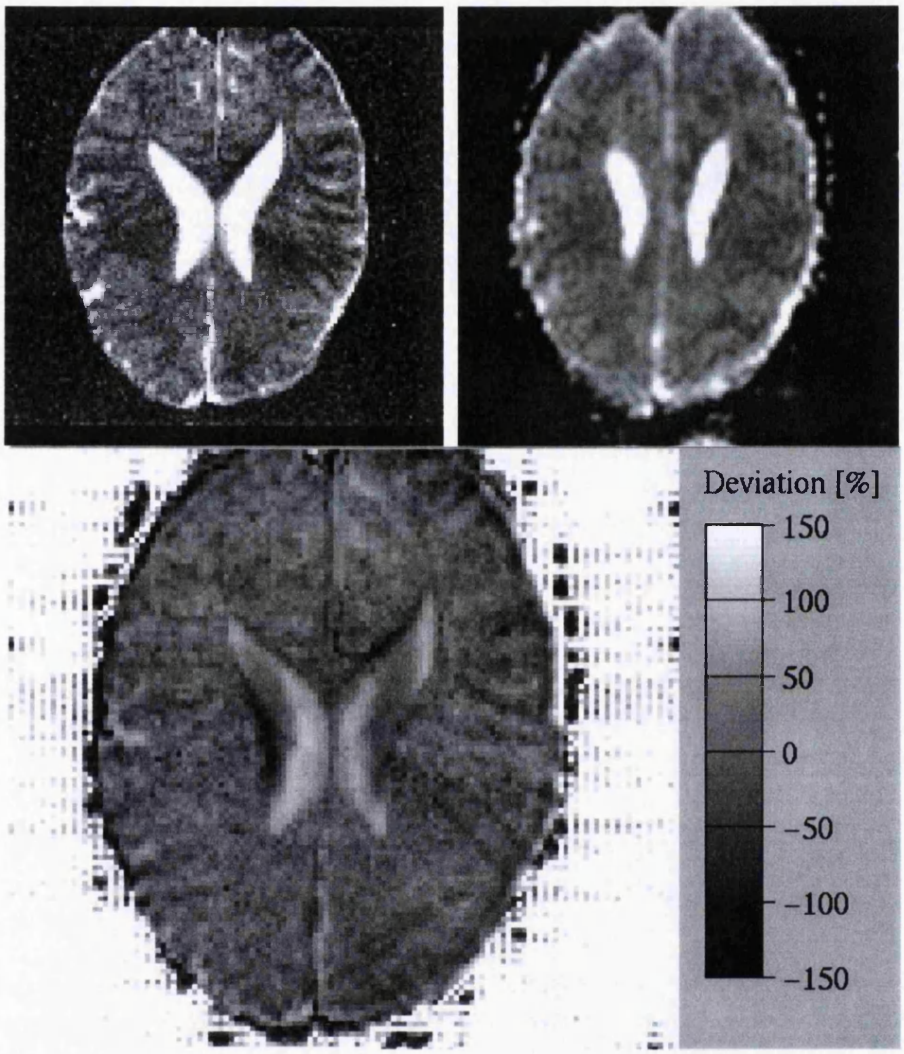

Figure 7.6: The figure shows the difference of the trace images measured with the Half-FOV EPI and single shot EPI sequences.

Top Left: One slice of the trace image measured with the Half-FOV EPI sequence.

Top Right: One slice of the trace image measured with the single shot EPI sequence.

Bottom: The difference image, computed as the difference divided by the mean image.

with the multi-shot sequences are higher than the respective values measured with the single shot EPI sequences. In CSF, the values of Fractional Anisotropy were smaller for both the multi-shot sequences.
In the bottom of Figure 7.7 is shown, for one slice, the difference of the Fractional Anisotropy maps measured with the Half-FOV EPI sequences (Top Left) and the single shot EPI sequences (Top Right).
The Fractional anisotropy map measured with the Half-FOV EPI sequence is less affected by eddy current related artefacts, which appeared as the bright ring in the edge of the top right image in Figure 7.7 measured with the single shot EPI sequence. The white matter, notably in the Posterior Commissure, is better defined in the image measured with the Half-FOV EPI sequence. The difference image in the bottom of Figure 7.7 shows the improvement of the measurement of Fractional Anisotropy with the Half-FOV EPI sequence, notably a clearer definition of the white matter fiber tract structure and better contrast in sub-cortical regions.

7.4 Conclusion

To achieve high spatial resolution, either the interleaved EPI or Half-FOV EPI sequence should be chosen. If a large number of slices for whole brain coverage is necessary, the acquisition time is similar for both sequences.
In the interleaved EPI sequence, the acquisition was either triggered by the ECG signal or the motion contaminated data were discarded by means of data post processing. However, it was difficult to remove the ghosting artefacts due to a phase mismatch between the two segments, which were mainly from movement and eddy current. Images measured with the Half-FOV EPI sequences were free from Nyquist ghosts. Cardiac gating did not improve the image quality of this sequence type.
The SNR in the images measured with the sequences of interleaved EPI was higher than the SNR in the images measured with Half-FOV EPI sequence. This was mainly due to

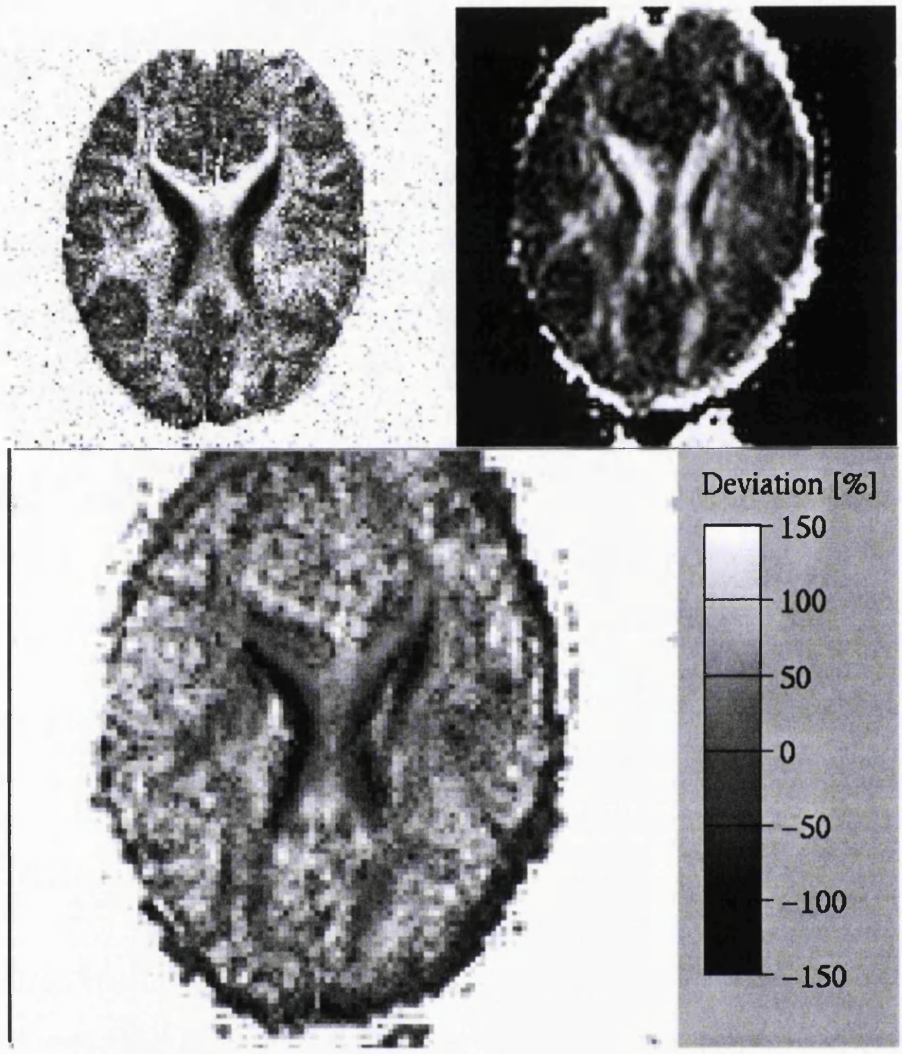

Figure 7.7: The figure shows the difference of the Fractional Anisotropy map measured with the Half-FOV EPI and single shot EPI sequences.

Top Left: One slice of the Fractional Anisotropy image measured with the Half-FOV EPI sequence.

Top Right: One slice of the Fractional Anisotropy image measured with the single shot EPI sequence.

Bottom: The difference image, computed as the difference divided by the mean image.

the multiplexing in the phase encoding direction in the interleaved EPI sequences.
The diffusion properties such as trace and Fractional Anisotropy measured with both the multi-shot sequences were similar for all types of tissues. The images measured with the interleaved EPI sequences suffered from ghosting artefacts. The images measured with the Half-FOV EPI sequences demonstrated a clear reduction of partial volume effects when compared to the images measured with the single shot EPI sequence.
The results suggest that the Half-FOV EPI sequence without cardiac gating is the best choice for high resolution diffusion tensor imaging with a large brain coverage. If only a restricted part of the brain is of interest, the interleaved EPI sequence without cardiac gating, which allows more averages in a limited time, could be used provided good eddy current compensation was available.

Chapter 8

Neuron Fiber Tracking With the Diffusion Tensor

8.1 Introduction to white matter fiber tracking

It has been realized for centuries that the brain is the centre of cognition. However, the research into the functioning of human brain is quite limited. Even the relatively smaller brains of animals are tremendously complicated. In the human brain, cognitive function does not occur as a single entity. Instead, a higher cognitive function is normally segregated into several independent modules acting in concert to achieve complete function. Information processing in the brain occurs in anatomically distinct regions, which are each called a 'functional neural area'. A functional neural area is a group of neurons lying within an anatomically specific area in the brain, which performs a specific function. Several independent functions performed by separate functional areas work together to form a more complicated cognitive task.(Gay *et al.*, 1995). Within the modules defined by the functional segregation, there are heavy interconnections between all the components.

Some information about anatomical connectivity can be obtained from functional brain imaging techniques such as EEG or fMRI. Alternatively the anatomical connectivity of the brain can only be measured from post mortem studies because most of the approaches required the sacrifice of the animal and thus cannot be performed on humans *in vivo*. Usually tracers labeled by fluorescent or radio-active isotopes are injected in to the axons retrogradely or anterogradely. The connection map of the brain is then acquired by the three-dimensional reconstruction of the serial sections.
MR diffusion tensor imaging offers a new method to study the connectivity in white matter. One of the great advantages of this technique is that it is completely non-invasive and can be performed *in vivo*. The principal eigenvector of the measured diffusion tensor might be considered aligned with the direction of the fiber bundle across the voxel of interest. Considering the directions of the principal eigenvectors in the neighbouring voxels, we can map out the structures of the neuron fibers in white matter.
Figure 8.1 plots the direction of the principal eigenvector from pixel to pixel, in an ROI in one branch of the Corpus Callosum. It shows clearly that the direction of the eigenvector follows the direction of the main neuron fiber bundles. However, the direction can be easily deflected by the noise presented in the measurement.

Various tracking algorithms have been developed from several research sites independently. Mori et al (Mori *et al.*, 1999b) used the FACT algorithm (Fiber Assignment by Continuous Tracking) to determine the anterior commissure, olfactory tract, middle forebrain bundle and fornix in an adult Sprague-Dawley rat brain fixed on 5 % formalin for 2 weeks. The tracking started from the centre of the voxel of interest and proceeded along the direction of the principal eigenvector within the voxel. At crossing the boundary, the direction of the tract changed to the direction of the principal eigenvector of the neighbour. This procedure was iterated until a terminal situation was met. The tracking is, in principle, continuous and pixelwise with interpolation.
Conturo et al (Conturo *et al.*, 1999) used a similar algorithm combined with fMRI study

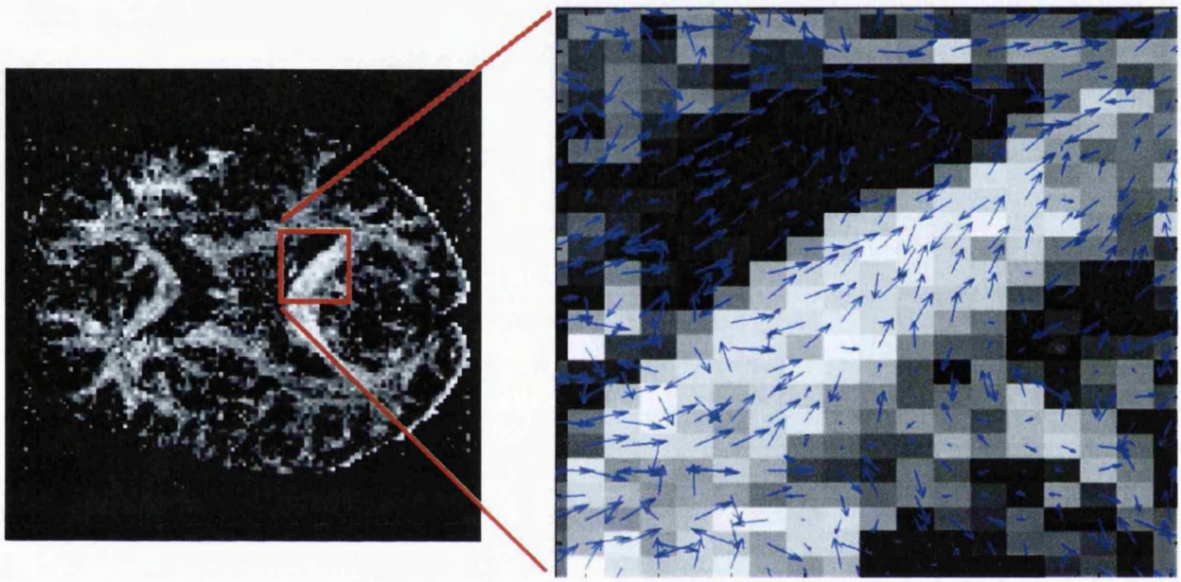

Figure 8.1: The figure shows the direction of the principal eigenvector in an ROI in the Corpus Callosum

Left: Fractional Anisotropy Map shows the diffusion anisotropy in the slice of interest.

Right: A quiver map shows the direction of the principal eigenvector in an ROI in one branch of the Corpus Callosum, overlapped with the Fractional Anisotropy map.

with visual stimulus to follow the geniculo-calcarine visual pathway on four normal males. The fiber tract started from the lateral geniculate nucleus of the thalamus and was followed to the occipital horns of the lateral ventricle.

These pixel-by-pixel tracking algorithms are dependent on good resolution and unable to distinguish between afferent and efferent fibers. Further complications include fiber crossing, touching and merging. A different approach based on Markovian random field theory was proposed by Poupon et al (Poupon *et al.*, 1998; Poupon *et al.*, 1999), which takes into account of the usual fan shaped merge of several fascicles in one large bundle. A regularised direction map inferred from diffusion tensor data was proposed, which stems from *a priori* knowledge on the white matter geometry embedded in a model of the bending energy. The result was successfully demonstrated on fibers near the Corpus Callosum and around the pyramidal pathways which merges thalamo-parietal and cortico-spinal fibers.

G.J.M. Parker in Institute of Neurology, University College London developed the fast marching algorithm, which is based on the theory of level sets (Parker, 2000). This algorithm allows for branching or merging of bundles, and for the definition of the paths of most likely connection between multiple points. The algorithm successfully traced out the axial extent of the left crus cerebrum within the brain stem.

Dr. Martin Koch from Universitaetsklinikum Hamburg-Eppendorf, Neurologische Klinik, Hamburg, Germany, developed a numerical assessment of anatomical connectivity between arbitrary cortical regions. Instead of generating a trajectory by following the direction of the major eigenvector, a probability approach was investigated. If a particle in a voxel A is jumping in a random order from voxels to voxels within the brain, it is reasonable to assume that the probability is higher to enter a neighbouring voxel which lies in the direction of the largest diffusion coefficient of the current voxel. The particle will move with a higher probability along the direction of fibers. If the experiment was repeated, a relative measure of the probability of a particle in the starting voxel reaching the target voxel can be obtained. This probability provided a reflection of the anatomi-

cal connectivity. The frequency which each voxel was hit as a result of a particle jump during its path or at its terminating point was recorded and normalised to the maximum over all considered voxels in the volume. A detailed description of the algorithm can be found in (Koch *et al.*, 2002).

To compensate for the signal loss intrinsic in the diffusion weighted MR experiment, most of the measurements in the above mentioned fiber tracking algorithms required relatively thick slices. To maintain the high in-plane resolution, anisotropic sized voxels are often used, which leads to bias in the tracking along the slice selection direction. With the Half-FOV diffusion tensor EPI, we will show the effect of such bias in a typical voxel by voxel fiber tracking algorithm.

8.2 Method and Theory

8.2.1 Diffusion Tensor Data Used in the Fiber Tracking

Two normal male volunteers aged 31 and 29 were scanned with the Half-FOV DT-EPI sequences in four separate sessions. Each session acquired fifty-two slices to cover the major part of the brain. The voxel is isotropic and 1.5 mm in size. The total acquisition time for each individual session was approximately 63 minutes for 9 averages. The tetrahedral diffusion encoding scheme was used. The number of averages in the first subject was 8, 10, 6, and 10 respectively and for the second subject was 9 for all sessions.

The tracking algorithm was implemented by Jacques-Donald Tournier in London(Tournier *et al.*, 2002). It follows the fiber track voxel by voxel from a starting point based on the direction of the principal eigenvector at each single voxel.

The diffusion tensor was calculated for each single session as described in the previous chapter. The eigenvalues are sorted according to the absolute magnitude. The Fractional Anisotropy map was calculated and used as a threshold to avoid tracking in the

	First Subject			second Subject		
	1st session	2nd session	3rd session	1st session	2nd session	3rd session
X axis	0.95	0.06	-0.09	-2.01	0.28	-2.16
Y axis	0.76	1.45	-1.32	-4.92	-0.02	-2.44
Z axis	-6.49	-3.56	-4.66	1.76	-1.51	11.17

Table 8.1: The table shows the degree of rotation for both subjects along the three principle axes after coregistration by SPM99.

	First Subject		second Subject	
	single session	coregistered	single session	coregistered
SNR	18.2	35.1	17.3	33.6
FA	0.97 $\pm$ 0.02	0.96 $\pm$ 0.03	0.92 $\pm$ 0.01	0.91 $\pm$ 0.01

Table 8.2: The table shows the SNR and calculated Fractional Anisotropy for both subjects from data acquired in single session and the coregistered data from four sessions.

ventricle, gray matter or outside of the brain. The limit was set at 0.4.
The heads of the subjects were carefully fixed with the immobilization pad provided by Siemens. The slice positions were then carefully adjusted to be as close as possible for each single session. The data from separate sessions were co-registered by SPM99 to produce a combined data set, which provided improved SNR. Table 8.1 shows the degree of rotation along different axis by the co-registration procedure.

Table 8.2 shows the SNR and Fractional Anisotropy from both subjects measured in one single session and in the coregistered data. The ROI was selected in the Genu of the Rostrum of the Corpus Callosum.

Three data sets were created from the original diffusion tensor data. In the first set, data from every two slices in the measured diffusion tensor were added to create a new data set of double slice thickness, which is equivalent to 3 mm. In the second data set, every three slices were added to create a data set of 4.5 mm slice thickness. In the last data set, every four slices were added to create a new data set of 6 mm slice thickness. Those four data sets, with slice thicknesses of 1.5mm, 3mm, 4.5mm and 6 mm respectively, were used for the tracking.

8.2.2 Fiber Tracking Algorithm

The tracking algorithm started from a seed point defined by the user. The procedure of tracking was iterated until a terminating condition was met. The track was generated by calculating the next point along the path from the current point with the information contained in the eigenvectors of the diffusion tensor.
The algorithm was implemented by Mr. Jacques-Donald Tournier, unit of Biophysics, Institute of Child Health, University College London, United Kingdom. The measured diffusion tensor was linearly interpolated before the calculation of the eigenmatrix. The interpolation depends on the step size of the track specified by the user. In the project, the step size was specified as either 0.5 or 0.1 of the voxel size. The track was generated in an iterative manner described below.
(a) The diffusion tensor was calculated for the point of interest by linear interpolation from the nearest 8 points in the same plane.
(b) The eigenvalues at the point of interest were sorted according to the magnitude. The principal eigenvector, which corresponds to the largest eigenvalue, was computed.
(c) A displacement vector was calculated by the multiplication of the normalised eigenvector and the step size.
(d) The next point in the track was calculated by adding the displacement vector to the

current point.

The trajectory cannot move to a direction that is perpendicular to the fiber direction from the previous point. This procedure was iterated until a terminating condition was met. The terminating condition was under the following situation:

(a) When the Fractional Anisotropy falls below the threshold, which is 0.4 in the experiment

(b) When the trajectory reaches the target point, here specified as the starting point

(c) When the trajectory reaches a maximum distance or is repeated for a maximum number of steps

(d) when the trajectory moves outside the volume

The detail of the algorithm can be found in (Tournier *et al.*, 2002)

8.3 Fiber Tracking in the Genu of the Corpus Callosum

8.3.1 Data acquired in Single Session and Coregistered Data

A starting point was selected from one branch of the Genu of Corpus Callosum. The algorithm was applied to the data acquired in single session and the data coregistered from all the sessions.

Figure 8.2 shows the trajectory in the data acquired from a single session. The trajectory followed nicely along the curve of the genus and stretched into the sub-cortical regions. Two step sizes were used here: 0.5 and 0.1 of the voxel size.

Figure 8.3 shows the trajectory calculated from the coregistered data. After coregistration, the diffusion tensor from certain measurements was rotated. However, the rotation was sufficiently small not to affect the result from the tracking algorithm, which is clear

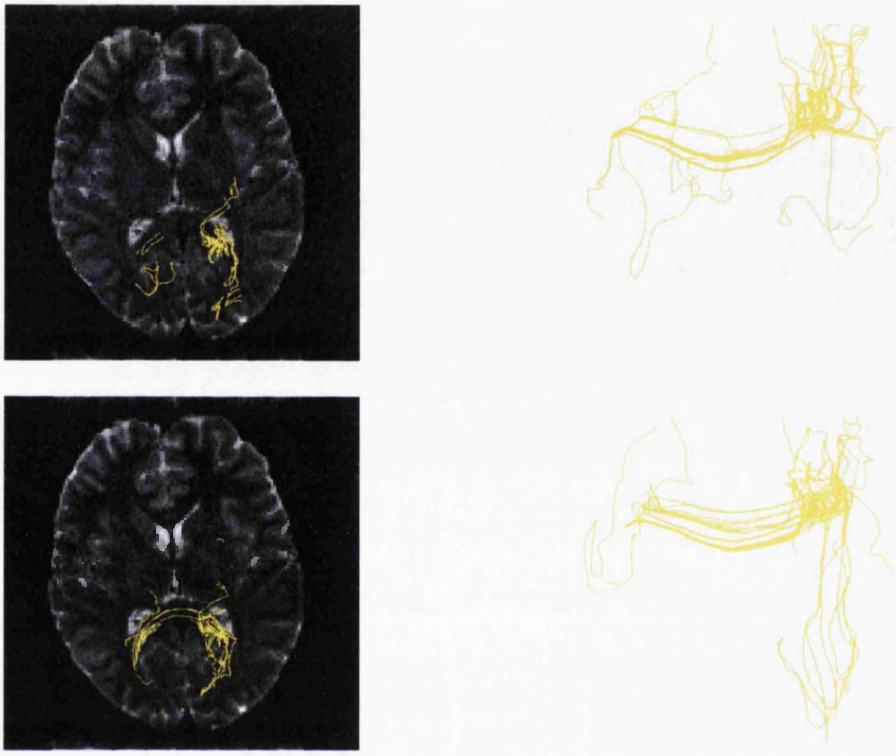

Figure 8.2: The figure shows the trajectory staring from one branch of the genu in the corpus callosum and extended to the other side of the Genu. The data is from one single session.

Top Left: The trajectory shown in the transversal plane, overlapped with the low-diffusion weighted image from the same plane as the starting point. The step size used in the computing is 0.5.

Top Right: The same trajectory viewed from the coronal plane.

Bottom Left: The trajectory shown as in the image from the top row but the step size used in the computing is 0.1.

Bottom Right: The same trajectory viewed from the coronal plane.

from Figure 8.3.

From Figure 8.2 and Figure 8.3, it is clear that the trajectories followed smoothly along the curve of the Genu of the Corpus Callosum in both the single session data set and the coregistered data set. The results are very similar in both data sets. However, the trajectory in the single session is inclined to move into sub-cortical areas, noticeably towards the end of the individual track. The trajectory is more uniform and consistent in the coregistered data set. Because of the inferior SNR in the single session data set, some tracks will move away from the known fiber bundles in the Corpus Callosum.
The step size of interpolation also has a sizeable effect on the trajectory. Larger step sizes tend to introduce noise in the trajectory, which then wandered off to sub-cortical areas where the directionality of diffusion is not so strong.
In general, the trajectory produced by the tracking algorithm does follow the known anatomy in the region of interest in Corpus Callosum. The SNR was greatly improved by the coregistration. Although the tensor was rotated as shown in Table 8.1, the degree of rotation was small enough to keep the trajectory produced following the fiber bundle in Corpus Callosum.

8.3.2 Trajectory in Anisotropic Voxels

A starting point was selected in the equivalent position in the Corpus Callosum in all the diffusion tensor data sets. The step size was selected as 0.1 of the voxel size. Figures 8.4 and 8.5 shows the result of the tracking from different angles of view.

From the top left images in both Figures 8.4 and 8.5, it is seen that the trajectory in the data set of slice thickness of 1.5 mm stretched along the curve of the Genu of Corpus Callosum, which matched the known anatomy. The shapes of the trajectory look very

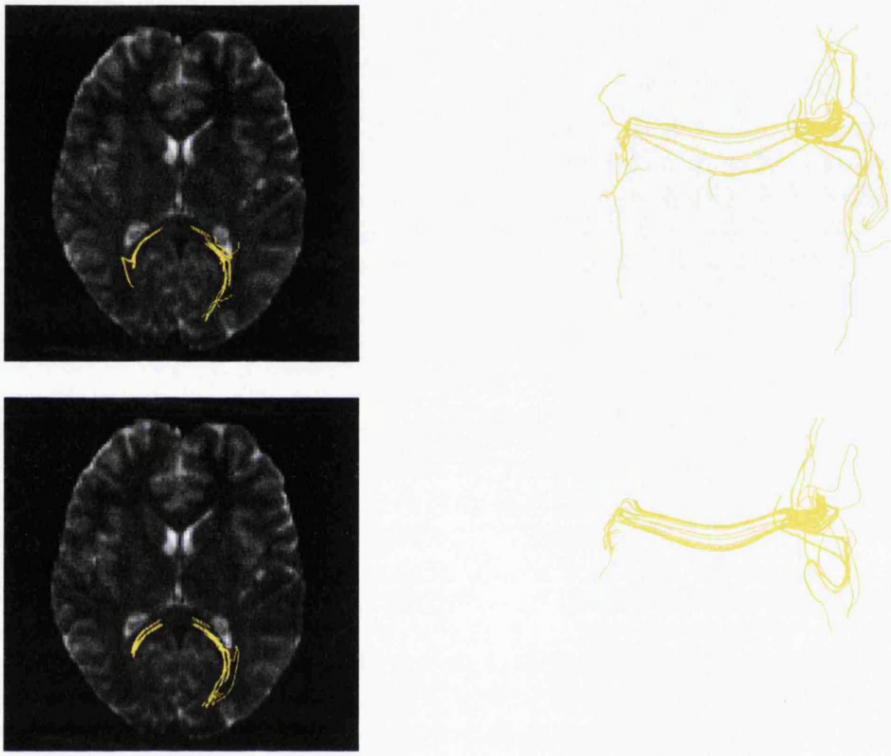

Figure 8.3: The figure shows the trajectory starting from one branch of the genu of the corpus callosum in the coregistered data. The step size in the trajectory is 0.5 (Top row) and 0.1 (Bottom Row).

Top Left: The trajectory shown in the transversal plane, overlapped with the low-diffusion weighted image from the same plane as the starting point. The step size used in the computing is 0.5.

Top Right: The same trajectory viewed from the coronal plane.

Bottom Left: The trajectory shown as in the image from the top row but the step size used in the computing is 0.1.

Bottom Right: The same trajectory viewed from the coronal plane.

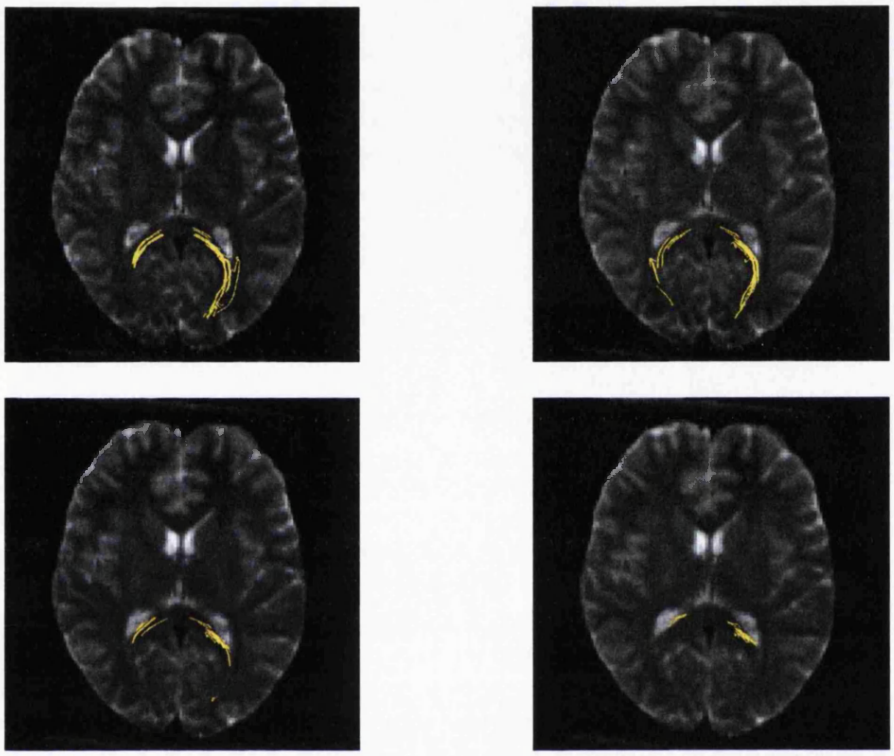

Figure 8.4: The figure shows the trajectory starting from one branch of the Genu of the Corpus Callosum for difference slice thickness. The step size in the trajectory is 0.1.

Top Left: slice thickness is 1.5 mm.

Top Right: slice thickness is 3.0 mm.

Bottom Left: slice thickness is 4.5 mm.

Bottom Right: slice thickness is 6.0 mm.

Figure 8.5: The figure shows the trajectory starting from one branch of the Genu of the Corpus Callosum for difference slice thickness, displayed at coronal view. The step size in the trajectory is 0.1.

Top Left: slice thickness is 1.5 mm.

Top Right: slice thickness is 3.0 mm.

Bottom Left: slice thickness is 4.5 mm.

Bottom Right: slice thickness is 6.0 mm.

similar in the data sets with slice thicknesses of 1.5 mm, 3.0 mm and 4.5 mm. However, the tracks connecting both sides of the Genu are less dense in both the data sets of 3.0 mm and 4.5 mm slice thickness.

The trajectory in the data set with slice thickness of 6.0 mm shows less connections between both sides of the Genu of the Corpus Callosum. Instead most of the tracks are shorter and, either wandered off vertically, or merged to the neighbouring track, as shown in the coronal view of the bottom right image of Figure 8.5.

8.4 Discussion

The diffusion coefficient is calculated from the logarithmical signal attenuation in two images with different diffusion weighting. The diffusion tensor is used to characterise the diffusion in various directions. Any translation, rotation and shearing introduced in the original diffusion weighted images will potentially affect the accuracy in the estimation of the diffusion tensor. It is thus intrinsically dangerous to change the diffusion data, which might change the directions of the diffusion tensor.

However, if the SNR in a diffusion tensor data set is low, the estimation of the eigenvalues will be inaccurate and the direction of the eigenvectors will be affected by noise. Any fiber tracking algorithm based on following the direction of the principal eigenvector will fail if the SNR is too low.

Co-registration is a commonly used technique to register the data from the same subject but suffering from mis-alignment. To coregister the diffusion data from separate sessions will lead to a diffusion data set of improved SNR. Yet the direction of the diffusion tensor might be changed as well. However, without coregistration, the direction of the diffusion tensor might be affected by the noise. It is thus the choice of the individual investigators whether to apply the technique of coregistration or not.

In this project, the positions of the heads of the subjects were carefully guided by markers in the face and fixed by immobilization pads. The degree of rotation during coregistra-

tion is sufficiently small not to affect the tracking algorithm seriously, as can be seen from Figure 8.3.

The diffusion data were further interpolated before the tracking process. The step size of the interpolation will affect the resulting trajectory. In the project, linear interpolation was implemented, which lead to an optimal result when tracking at a step size of 0.1 of the voxel size.

Thick slices are often used in the tracking when high in-plane resolution and SNR are necessary. Anisotropic voxel size will lead to potential bias in the slice selection direction. The diffusion weighted image is the result of the diffusion averaged within the whole pixel. Several consecutive slices were added to create a new diffusion tensor data set which is equivalent to the diffusion tensor measured with various slice thicknesses.

Using a voxel by voxel tracking algorithm with interpolation, the results of the trajectories showed different track distributions with different slice thickness. It is difficult to quantify the bias in the tracking in the expected direction but it does show less tracks to go along the curve of the Genu in the thick slices, which lies in the horizontal directions in Figure 8.5.

When the slice thickness is doubled, the trajectory looks sufficiently similar to the trajectory from the original data set. As slice thickness increases, the tracks merged because of the increased voxel size. This will reduce the possibility to distinguish from between merging or touching fibers in some areas.

In the project, the terminal point was selected the same as the starting point. The track will continue until a fixed distance has been reached or the Fractional Anisotropy fell under the threshold, which means the track reached beyond the white matter neuron fibers. In this project, the track often ended in the sub-cortical area, as can be seen in Figure 8.4. If combined with functional study, it would be interesting to test if a track starting from one neuron area reaches a target neuron area.

The tracking algorithm was applied only to a starting point in the Corpus Callosum. There is no way currently to validate the resulting trajectory . We can only compare the

trajectory to the well known big fiber bundles. In less understood and complicated areas, it would be difficult to determine whether such a trajectory does match the existence of real neuron fibers. For comparison between different data sets, it is thus more reliable to study a well understood area.

8.5 Conclusion

From the quiver map in Figure 8.1, it has been shown that the direction of the principal eigenvector in the diffusion tensor is aligned with the direction of the neuron fiber. A voxel by voxel tracking algorithm was successfully applied to the diffusion tensor acquired by the Half-FOV EPI sequence. Several trajectories were traced in the Genu of the Corpus Callosum from various data sets. The result shows that with careful positioning, data set coregistered from separate sessions produces similar and good tracks compared with data obtained in a single session, which is more affected by the noise.
When thick slices were used to compensate for the signal loss in high in-plane resolution diffusion tensor images, potential bias occurred in the slice selection direction in the voxel by voxel tracking algorithm.

Chapter 9

Conclusion

In this project, diffusion tensor echo planar imaging was successfully carried out in human brain. Studies based on the single shot EPI sequence were conducted in healthy volunteers to demonstrate the reproducibility of this technique. The result showed that DT-EPI was a stable and non-invasive technique for the measurement of diffusion *in vivo*. DT-EPI provides quantitative information about the bulk diffusion and shows the anisotropic nature of diffusion in the biological environment.

The technique was used in a study on the recovery of a stroke patient with left Pons infarct. DT-EPI showed the sensitivity of diffusion properties to the hyper-chronic ischaemic insult compared with the nearby normal tissues. It also demonstrated the recovery process. However, the low spatial resolution, which results in serious partial volume artefact, greatly limited the applications of this technique. New sequences with high resolution and satisfactory SNR were deemed necessary. Sequences of multi-shot EPI were successfully developed to improve the spatial resolution, which included the interleaved EPI sequence of two segments and the Half-FOV EPI sequence.

Various sources leading to the ghosting artefacts in diffusion imaging were discussed together with proposed solutions. A selective averaging algorithm was developed for the interleaved EPI sequence with two segments. The data were sampled continuously without cardiac gating. The motion contaminated data were screened out by comparing the reference profile from the navigator echoes and discarded where necessary.

To acquire a Nyquist ghost free image, the Half-FOV EPI sequence was developed which combined the data in the image domain, and thus was free from the phase variations between acquisitions.

A comparison study was made between the interleaved EPI and the Half-FOV EPI sequences, both with and without cardiac gating. The single shot EPI sequence was used as the base of reference. The result shows that cardiac gating improves the image quality acquired by the interleaved EPI sequence but has no effect on the images from the Half-FOV EPI sequence. The acquisition time for sequences with cardiac gating is greatly extended. In the interleaved EPI sequence, even after the motion corrupted data were discarded, the final images were still contaminated by ghosting artefacts from phase mismatch between segments, which resulted from sources other than motion.

Images from the Half-FOV EPI sequence have slightly lower SNR compared with images from the interleaved EPI sequences (75 %). The total acquisition time is similar for both techniques if a large number of slices were acquired. The images acquired with the Half-FOV EPI sequence are free from Nyquist ghost, which made it the sequence of choice.

The data from the diffusion tensor measurements by the Half-FOV EPI sequence were used for the white matter fiber tracking. A voxel by voxel algorithm, based on following the direction of the principal eigenvector, was developed by a collaborating research

group. ROIs in the Genu of the Corpus Callosum were selected. The result shows that the algorithm successfully tracked the major fiber bundles in the white matter from the diffusion tensor measured from the Half-FOV sequence, for the coregistered data, which were acquired from several separate sessions, and the data from a single session.
The algorithm also demonstrated the potential bias when tracking in anisotropic voxels, which is a common practice in DTI. The effect appeared as the slice thickness increased to more than twice the pixel size in the slice selection direction.

Future Work

To improve the acquisition speed of the Half-FOV EPI sequence, a shorter echo time will be designed while maintaining the satisfactory eddy current compensation in the scanner.
Further improvement in the measurement of diffusion will be investigated. This includes data acquisition with higher angular density of the diffusion weighting gradients. In the optimized tetrahedral diffusion encoding scheme used in the project, SNR of the diffusion weighted image was improved by acquiring more averages with the diffusion weighting gradient in one direction. It has been suggested if more measurements than the minimum of seven are to be made, then the bias introduced by measuring signal attenuation along a limited number of gradient directions is reduced by using more gradient vector directions. The ratio of the total number of measurements with high diffusion weighting to the number at the low diffusion weighting should be maintained at approximately 11.3 to 1 but with only one measurement for each diffusion encoding gradient vector direction.(Jones, 1998)
New methods for diffusion measurements will be developed to fully characterise the nature of the anisotropic diffusion in tissues, such as q-space imaging.(Cory & Garroway, 1990; Callaghan *et al.*, 1991)

Longitudinal studies on neurological diseases, such as stroke and tumour, will be performed using the high resolution sequence. The diffusion anisotropy at different stages of the diseases will be compared. There will be further development into liver imaging. Because of the genetic variance, hepatoma is much more common in Chinese people. Diffusion tensor imaging is expected to provide a new contrast mechanism which might help early distinguishment of benign or malignant tumours.

One of the major applications is white matter fiber tracking. The information from DT-EPI will be combined with fMRI studies. The Half-FOV EPI sequence provides a new way to acquire high resolution diffusion tensor data. Paradigms which activate the Wernicke region and Broca's region in the brain will be designed. Several existing fiber tracking algorithms will be examined. The result will be validated on human volunteers.

Bibliography

AHN, C.B., LEE, S.Y., NALCIOGLU, O., & CHO, Z.H. 1986. An improved nuclear magnetic resonance diffusion coefficient imaging method using an optimised pulse sequence. *Medical physics*, **13**, 789–793.

AHRENS, E.T., LAIDLAW, D.H., REDHEAD, C., BROSNAN, C.F., FRASER, S.E., & JACOBS, R.E. 1998. Mr microscopy of transgenic mice that spontaneously acquire experimental allergic encephalomyelitis. *Magnetic resonance in medicine*, **40**, 119–132.

ARMITAGE, P.A., & BASTIN, M.E. 2001. Utilizing the diffusion-to-noise ratio to optimize magnetic resonance diffuion tensor acquisition strategies for improving measurements of diffusion anisotropy. *Magnetic resonance imaging*, **45**, 1056–1065.

BASSER, P.J., & PIERPAOLI, C. 1996. Microstructural and physiological features of tissue elucidated by quantitative-diffusion-tensor mri. *Journal of magnetic resonance series b*, **111**, 209–219.

BASSER, P.J., & PIERPAOLI, C. 1998. A simplified method to measure the diffusion tensor from seven mr images. *Magnetic resonance in medicine*, **39**, 928–934.

BASSER, P.J., MATTIELO, J., & LEBIHAN, D. 1994a. Estimation of the effective self-diffusion tensor from the nmr spin echo. *Journal of magnetic resonance series b*, **103**, 247–254.

BASSER, P.J., MATTIELLO, J., & LEBIHAN, D. 1994b. Mr diffusion tensor spectroscopy and imaging. *Biophysical journal*, **66**(259-267).

BASSER, P.J., MATTIELLO, J., & LEBIHAN, D. 1995. *Diffusion and perfusion magnetic resonance imaging.* New York: Raven Press. Chap. Anisotropic diffusion: MR diffusion tensor imaging, pages 134–140.

BELLIVEAU, J.W., KENNEDY, D.N., & ET AL, R.C MCKINSTRY. 1991. Functional mapping of the human visual cortex by magnetic resonance imaging. *Science*, **254**, 716–719.

BENVENISTE, H., & JOHNSON, G.A. 1992. Mechanism of ischaemia induced changes in the brain water diffusion coefficient studied by mri and brain microdialysis. *Stroke*, **23**, 746–754.

BOWTELL, R., & SCHMITT, F. 1998. *Echo-planar imaging: theory, technique and application.* 1st edn. Berlin Heidelberg: Spinger-Verlag. Chap. Echo-Planar Imaging Hardware, pages 31–64.

BRUDER, H., FISCHER, H., REINFELDER, H-E., & SCHMITT, F. 1992. Image reconstruction for echo-planar imaging with non-equidistant k-space sampling. *Magnetic resonance in medicine*, **23**, 311–323.

BUONANNO, F.S., PYKETT, I.L., & ET AL, T.J. BRADY. 1982. Proton nmr imaging in experimental ischaemic infarction. *Stroke*, **14**, 178–184.

CALLAGHAN, P.T., COY, A., & MACGOWAN, D. 1991. Diffraction-like effect in nmr diffusion studies of fluid in porous solid. *Nature*, **351**, 467–469.

CARR, H.Y., & PURCELL, E.M. 1954. Effects of diffusion on free precession in nuclear magnetic resonance experiments. *Journal of chemical physics*, **34**, 2057–2061.

CHAPMAN, B., TURNER, R., ORDIDGE, R.J., DOYLE, M., CAWLEY, M., COXON, R., GLOVER, P., & MANSFIELD, P. 1987. Real-time movie from a single cardiac cycle by nmr. *Magnetic resonance in medicine*, **5**, 246–254.

CONTURO, T.E., LORI, N.F., CULL, T.S., AKBUDAK, E., SNYDER, A.Z., SHIMONY, J., MCKINSTRY, R.C., H.BURTON, & RAICHLE, M.E. 1999. Tracking neuronal fiber pathways in the living human brain. Proceedings of the National Academy of Sciences of the United States of America.

CORY, D.G., & GARROWAY, A.N. 1990. Measurement of translational displacement probabilities by nmr - an indicator of compartmentation. *Magnetic resonance in medicine*, **14**, 435–444.

DIETRICH, O., HEILAND, S., BENNER, T., & SARTOR, K. 2000. Reducing motion artefacts in diffusion-weighted mri of the brain: efficacy of navigator echo correction and pulse triggering. *Neuroradiology*, **42**, 85–91.

DOUEK, P., TURNER, R., PEKAR, J., PATRONAS, N., & LEBIHAN, D. 1991. Mr color mapping of myelin fiber orientation. *Journal of computer assisted tomography*, **15**, 923–929.

D.STARK, & BRADLEY, W.G. 1992. *Magnetic resonance imaging.* Mosby Year Book. Chap. Signal, Contrast and Noise, pages 331–380.

EDELSTEIN, W.A., HUTCHINSON, J.M.S., JOHNSON, G., & REDPATH, T. 1980. Spin warp nmr imaging and applications to human whole body imaging. *Physics in medicine and biology*, **25**, 751–756.

EINSTEIN, A. 1926. *Investigations on the theory of the brownian movement.* Dover, New York.

FEINBERG, D., & JAKAB, P.D. 1990. Tissue perfusion in humans studied by fourier velocity distribution, line scan and echo-planar imaging. *Magnetic resonance in medicine*, **16**, 180–193.

FEINBERG, D., & OSHIO, K. 1991. Gradient-echo time shifting in fast imaging. *Page 1239 of: Book of abstracts, 10th annual meeting, society of magnetic resonance in medicine.*

GAY, C.T., BRANNAN, S.K., & FOX, P.T. 1995. *Diffusion and perfusion magnetic resonance imaging.* New York: Raven Press. Chap. Human functional brain mapping: functional areas, variables, and information processing theory, pages 217–226.

HAACKE, E.M., BROWN, R.W., THOMPSON, M.R., & VENKATESAN, R. 1999. *Magnetic resonance imaging: Physical principles and sequence design.* John Wiley and Sons. Chap. Signal, Contrast and Noise, pages 331–380.

HAHN, E. 1950. Spin echoes. *Physics review*, **80**, 580–594.

HARRIS, K.R., & WOOLF, L.A. 1980. Pressure and temperature dependence of the self diffusion coefficient of water and oxygen-18 water. *Journal of the chemical soceity faraday transaction i*, **76**, 377–385.

HASSELGROVE, J.C., & MOORE, J.R. 1996. Correction for distortion of echo planar images used to calculate the apparent diffusion coefficient. *Magnetic resonance in medicine*, **36**, 960–964.

HEID, O. 1997. Robust epi phase correction. *Page 2014 of: Proceedings of 6th annual meeting of the international society and magnetic resonance in medicine.*

HEID, O. 2000. Eddy current nulled diffusion weighting. *Page 799 of: Proceedings of 8th international society of magnetic resonance in medicine.* ISMRM, Denver.

HENNEL, F., & NEDELEC, J.F. 1995. Interleaved asymmetric echo-planar imaging. *Magnetic resonance in medicine*, **34**, 520–524.

HORNAK, J.P. 1996. *The basics of mri.* http://www.cis.rit.edu:80/htbooks/mri/.

HORSFIELD, M.A., LARSSON, H.B.W., JONES, D.K., & GASS, A. 1998. Diffusion magnetic resonance imaging in multiple sclerosis. *Journal of neurology, neurosurgery and psychiatry*, **64(suppl)**, 80–84.

JESMANOWICZ, A., BANDETTINI, P.A., & HYDE, J.S. 1997. Single-shot half nex 256 * 256 resolution epi at 3 tesla. *Page 1632 of: Proceedings of 5th annual meeting of the international society and meagnetic resonance in medicine.* ISMRM, Vancouver.

JEZZARD, P., BARNETT, A.S., & PIERPAOLI, C. 1998. Characterization of and correction for eddy current artefacts in echo planar diffusion imaging. *Magnetic resonance in medicine*, **39**, 801–812.

JOHNSON, G., & HUTCHINSON, J.M.S. 1985. The limitations of nmr recalled echo imaging techniques. *Journal of magnetic resonance*, **63**, 14–30.

JONES, D., WILLIAMS, S., & HORSFIELD, M. 1997. Full representation of white-matter fibre direction on one map via diffusion tensor analysis. *Page 1743 of: Proceedings of the 5th annual meeting of international society of magnetic resonance in medicine.*

JONES, DEREK. 1998 (December). *Diffusion tensor magnetic resonance imaging in the central nervous system.* Ph.D. thesis, Faculty of Science, Department of Medical Physics, University of Leicester.

KÄRGER, J., PFEIFER, H., & HEINK, W. 1988. *Principles and applications of self-diffusion measurements by nuclear magnetic resonance.* Vol. 1. Academic Press.

KELLEY, D., & ORDIDGE, R.J. 1993 (August). Techniques for phase correction of raw data for epi with unshielded gradient coils. *Page 384 of: Proceeding of the society of magnetic resonance in medicine, 12th annual meeting.* ISMRM, New York.

KIM, S.G., HU, X., ADRIANY, G., & UGŭRBIL, K. 1996. Fast interleaved echo-planar imaging with navigator: high resolution anatomic and functional images at 4 tesla. *Magnetic resonance in medicine*, **35**, 895–902.

KNIGHT, R.A., ORDIDGE, R.J., & ET AL, J.A. HELPERN. 1991. Temporal evolution of ischaemic damage in rat brain measured by proton nuclear magnetic resonance imaging. *Stroke*, **22**, 802–808.

KNIGHT, R.A., DERESKI, M.O., HELPERN, J.A., ORDIDGE, R.J., & CHOPP, M. 1994. Magnetic resonance imaging assessment of evolving focal cerebral ischemia. comparison with histopathology in rats. *Stroke*, **25**, 1252–1262.

KOCH, M.A., NORRIS, D.G., & HUND-GEORGIADIS, M. 2002. An investigation of functional and anatomical connectivity using magnetic resonance imaging. *Neuroimage*, **in press**.

KWONG, K.K., BELLIVEAU, J.W., CHESLER, D.A., GOLDBERG, I.E., WEISSKOFF, R.M., PONCELET, B.P., KENNEDY, D.N., HOPPEL, B.E., COHEN, M.S., & ET AL, R. TURNER. 1992. Dynamic magnetic resonance imaging of human brain activity during primary sensory stimulation. *Pages 5675–5679 of: Proceeding of national academy of science in united states of america*, vol. 89.

LARSSON, H.B.W., THOMSEN, C., & FREDERIKSEN, J. 1992. In vivo magnetic resonance diffusion measurement in the brain of patients with multiple sclerosis. *Magnetic resonance in medicine*, **10**, 7–12.

LEBIHAN, D., & BRETON, E. 1985. Imagerie de diffusion in-vivo par resonance magnetique. *Cr acad sci [ii]*, **15**, 1109–1112.

LEBIHAN, D., BRETON, E., LALLEMAND, D., GRENIER, P., CABANIS, E., & LAVAL-JEANTET, M. 1986. Mr imaging of intravoxel incoherent motions: application to diffusion and perfusion in neurologic disorders. *Radiology*, **161**, 401–407.

LeBihan, D., Turner, R., & Patronas, N. 1995. *Diffusion and perfusion magnetic resonance imaging.* New York: Raven Press. Chap. Diffusion MR imaging in normal brain and in brain tumours, pages 134–140.

Lutsep, H.L., Albers, G.W., & et al, A. DeCrespigny. 1997. Clinical utility of diffusion-weighted magnetic resonance imaging in the assessment of ischaemic stroke. *Annual neurology*, **41**, 574–580.

Mansfield, P. 1977. Multi-planar image formation using nmr spin echoes. *Journal of physics c*, **10**, L55–L58.

Mansfield, P., & Chapman, B. 1986. Active magnetic screening of gradient coils in nmr imaging. *Journal of physics e*, **15**, 235–239.

Mansfield, P., & Pykett, I.L. 1978. Biological and medical imaging by nmr. *Journal of magnetic resonance*, **29**, 355–372.

McKinnon, G.C. 1993. Ultrafast interleaved gradient echo planar imaging on a standard scanner. *Magnetic resonance in medicine*, **30**, 609–616.

Mehta, M.L. 1991. *Random matrices.* San Diego: Academic Press.

Mintorovitch, J., Moseley, M.E., Cileuitt, L., Shimizu, H., Cohen, Y., & Weinstein, P.R. 1991. Comparison of diffusion- and t_2- weighted mri for the early detection of cerebral ischaemia and reperfusion in rats. *Magnetic resonance in medicine*, **18**, 39–50.

Mori, S., Crain, B.J., Chacko, V.P., & van Zijl, P.C.M. 1999a. Three-dimensional tracking of axonal projections in the brain by magnetic resonance imaging. *Annual neurology*, **45**, 265–269.

Mori, S., Crain, B.J., Chacko, V. P., & van Zijl, P.C.M. 1999b. Three-dimensional tracking of axonal projections in the brain by magnetic resonance imaging. *Annals of neurology*, **45**(2), 265–269.

MOSELEY, M.E., KUCHARCZYK, J., & MINTOROVITCH, J. 1990a. Diffusion-weighted mr imaging of acute stroke: correlation with t_2- weighted and magnetic susceptibility-enhanced mr imaging in cats. *American journal of neuroradiology*, **11**, 423–432.

MOSELEY, M.E., COHEN, Y., MINTOROVITCH, J., CILEUITT, L., SHIMIZU, H., KUCHARCZYK, J., WENDLAND, M.F., & WEINSTEIN, P.R. 1990b. Early detection of regional brain ischaemia in cats: comparison of diffusion- and t_2-weighted mri and spectroscopy. *Magnetic resonance in medicine*, **14**, 330–346.

ORDIDGE, R.J., MANSFIELD, P., DOYLE, M., & COUPLAND, R.E. 1981. Real-time movie images of nmr. *British journal of radiology*, **55**, 729–733.

ORDIDGE, R.J., HELPERN, J.A., QING, Z.X., KNIGHT, R.A., & NAGESH, V. 1994. Correction of motional artefacts in diffusion-weighted mr imaging using navigator echoes. *Magnetic resonance imaging*, **12**, 455–460.

PAJEVIC, S., & PIERPAOLI, C. 1999. Color schemes to represent the orientation of anisotropic tissues from diffusion tensor data: application to white matter fiber tract mapping in the human brain. *Magnetic resonance in medicine*, **42**(3), 526–540.

PAPADAKIS, N.G., XING, D., HUANG, C.L.-H., HALL, L.D., & CARPENTER, T. A. 1999. A comparative study of acquisition schemes for diffusion tensor imaging using mri. *Journal of magnetic resonance*, **137**(1), 67–82.

PARKER, G.J.M. 2000. Tracing fiber tracts using fast marching. *Page 85 of: Proceedings to international society of magnetic resonance in medicine.*

PIERPAOLI, C., & BASSER, P.J. 1996. Towards a quantitative assessment of diffusion anisotropy. *Magnetic resonance in medicine*, **36**, 893–906.

POUPON, C., MANGIN, J-F, FROUIN, V., REGIS, J., POUPON, F., PACHOT-CLOUARD, M., LEBIHAN, D., & BLOCH, I. 1998. Regularization of mr diffusion tensor maps for tracking brain white matter bundles. *Pages 489–498 of:* GOOS, G., HARTMANIS, J., & VAN LEEUWEN, J. (eds), *Lecture note in computer science 1496.* MIT Boston: Springer-Verlag.

POUPON, C., CLARK, C.A., FROUIN, V., LEBIHAN, D., BLOCH, I., & MANGIN, J-F. 1999. Inferring the brain connectivity from mr diffusion tensor data. *Pages 489–498 of:* GOOS, G., HARTMANIS, J., & VAN LEEUWEN, J. (eds), *Lecture note in computer science 1679.* Cambridge: Springer-Verlag.

PRASAD, P.V., & NALCIOGLU, O. 1991. A modified pulse sequence for in vivo diffusion imaging with reduced motion artefatcs. *Magnetic resonance in medicine*, **28**, 116–131.

RÖMER, P., EDELSTEIN, W.A., & HICKEY, J. 1986. Self shielded gradient coils. proceedings of the 5th Annual Meeting of the SMRM, Montreal.

ROSEN, B., BELLIVEAU, J.W., & CHIEN, D. 1989. Perfusion imaging by nuclear magnetic resonance. *Magnetic resonance q*, **5**, 263–281.

RZEDZIAN, R.R. 1987 (August). High speed, high resolution, spin echo imaging by mosaic scan and mesh. *Page 51 of: Proceeding of the society of magnetic resonance in medicine, 6th annual meeting.*

RZEDZIAN, R.R. 1988 (30 August). *Methods of high speed imaging with improved spatial resolution using partial k-space acquisitions.* U.S. Patent 4767991 serial number 085568.

SHIMONY, J.S., MCKINSTRY, R.C., AKBUDAK, E., ARONOVITZ, J.A., SNYDER, A.Z., LORI, N. F., CULL, T.S., & CONTURO, T.E. 1999. Quantitative diffusion-tensor anisotropy brain mr imaging: normative human data and anatomic analysis. *Radiology*, **212**(3), 770–784.

SIESJO, B.K. 1978. *Brain energy metabolism.* New York: John Wiley.

SLAVIN, G.S., BUTTS, K., RYDBERG, J.N., JACK, C.R., & RIEDERER, S.J. 1995. Dual-echo interleaved echo-planar imaging of the brain. *Magnetic resonance in medicine*, **33**, 264–270.

SORENSEN, A., & BUONANNO, F. 1996. Hyperacute stroke: evaluation with combined multi-section diffusion-weighted and hemodynamically weighted echo-planar mr imaging. *Radiology*, **199**, 391–401.

STEJSKAL, E.O., & TANNER, J.E. 1965. Spin diffusion measurements: spin-echoes in the presence of a time-dependent field gradient. *Journal of chemical physics*, **43**, 3597–3603.

TANNER, J.E. 1978. Transient diffusion in a system partitioned by permeable barriers. application to nmr measurements with a pulsed field gradient. *Journal of chemical physics*, **69**(4), 1748–1754.

TAYLOR, D.G., & BUSHELL, M.C. 1985. The spatial mapping of translational diffusion coefficients by the nmr imaging techniques. *Physics in medicine and biology*, **30**, 345–349.

TOURNIER, J-D, CALAMANTE, F., KING, M.D., GADIAN, D.G., & CONNELLY, A. 2002. Limitations and requirements of diffusion tensor fiber tracking: Assessment using simulations. *Magnetic resonance in medicine*, **in press**.

TURNER, R. 1988. Perfusion studies and fast imaging. *Pages 245–258 of:* RESCIGNO, A., & BOICELLI, A. (eds), *Cerebral blood flow.* New York: Plenum.

TURNER, R. 1998. *Echo-planar imaging: theory technique and application.* Berlin Heidelberg: Springer-verlag. Chap. Diffusion imaging with echo-planar imaging, pages 311–324.

TURNER, R., & BOWLEY, R.M. 1986. Passive screening of switched magnetic field gradients. *Journal of physics e*, **19**, 876–879.

TURNER, R., LEBIHAN, D., MAIER, J., VAVREK, R., HEDGES, L.K., & PEKAR, J. 1990. Echo-planar imaging of intravoxel incoherent motion. *Radiology*, **177**, 407–414.

VLAARDINGERBROEK, M.T., & DEN BOER, J. 1996. *Magnetic resonance imaging.* Berlin Heidelberg: Springer-Verlag.

WERRING, D.J., A.T.TOOSY, CLARK, C. A., PARKER, G.J.M., BARKER, G.J., MILLER, D.H., & THOMPSON, A.J. 2000. Diffusion tensor imaging can detect and quantify corticospinal tract degeneration after stroke. *Journal of neurology, neurosurgery, psychiatry*, **69**(2), 269–272.

WONG, E.C. 1992 (14 - 20 August). Shim insensitive phase correction for epi using a two echo reference scan. *Page 4514 of: Proceeding of the society of magnetic resonance in medicine, 11th annual meeting, berlin.*

XING, D., PAPADAKIS, N.G., HUANG, C.L.H., LEE, V.M., CARPENTER, T.A., & HALL, L.D. 1997. Optimised diffusion-weighting for measurement of apparent diffusion coefficient (adc) in human brain. *Magnetic resonance imaging*, **15**, 771–784.